Models for Coupling of Salt and Water Transport

Proximal Tubular Reabsorption in Necturus Kidney

HENRY SACKIN and EMILE L. BOULPAEP

From the Department of Physiology, Yale University School of Medicine, New Haven, Connecticut 06510

ABSTRACT Models for coupling of salt and water transport are developed with two important assumptions appropriate for leaky epithelia. (*a*) The tight junction is permeable to both salt and water. (*b*) Active Na transport into the lateral spaces is assumed to occur uniformly along the length of the channel. The proposed models deal specifically with the intraepithelial mechanism of proximal tubular reabsorption in the *Necturus* kidney although they have implications for epithelial transport in the gallbladder and small intestine as well. The first model (continuous version) is similar to the standing gradient model devised by Diamond and Bossert but uses different boundary conditions. In contrast to Diamond and Bossert's model, the predicted concentration profiles are relatively flat with no sizable gradients along the interspace. The second model (compartment version) expands Curran's model of epithelial salt and water transport by including additional compartments and considering both electrical and chemical driving forces for individual Na and Cl ions as well as hydraulic and osmotic driving forces for water. In both models, ion and water fluxes are investigated as a function of the transport parameters. The behavior of the models is consistent with previously suggested mechanisms for the control of net transport, particularly during saline diuresis. Under all conditions the predicted ratio of net solute to solvent flux, or emergent concentration, deviates from exact isotonicity (except when the basement membrane has an appreciable salt reflection coefficient). However, the degree of hypertonicity may be small enough to be experimentally indistinguishable from isotonic transport.

INTRODUCTION

A theory of coupled water and solute transport was first proposed by Curran in 1960 (9). From experiments on rat ileum, he suggested a three-compartment series membrane model which could explain passive water movement against its chemical potential. Further experiments by Curran and coworkers using artificial models (10, 30) supported the three-compartment hypothesis for coupling of water and solute transport. Patlak et al. (33) have analyzed

the Curran model in detail and have presented the general characteristics of such a system.

In 1964, Diamond (12) and Whitlock and Wheeler (47) suggested that the lateral interspaces of gallbladder epithelium may function as the middle compartment described in Curran's model. Active solute transport into these intercellular channels would make them hypertonic enough to move water passively across the epithelium assuming the channels had the appropriate asymmetric apical and basal membrane transport coefficients.

In 1967, Diamond and Bossert further refined this theory for the coupling of solute and water transport by suggesting that a standing osmotic gradient existed within the intercellular spaces (13). Their model involved a number of important assumptions, two of which have not stood up to experimental verification in recent years: first, that the intercellular spaces are closed at the luminal end, and second, that active transport is confined to a small region at the start of the channel.

There is electrophysiological evidence that the proximal tubule (6), the small intestine (16), and the gallbladder (17) all have a high paracellular conductance, indicating a tight junction which is permeable to ions. Morphological evidence for an ionic paracellular pathway comes from the demonstration of lanthanum precipitates in the tight junction of the kidney proximal tubule (50), as well as the intestine and gallbladder (28). Furthermore, since La^{3+} has an ionic radius of 1.15 A, its presence in the tight junctions suggests that water molecules should also be able to permeate the apical end of the interspace. In addition, osmotic water permeabilities ranging from 4×10^{-5} to 4×10^{-3} ml cm^{-2} s^{-1} $osmol^{-1}$ for gallbladder, jejunum, and proximal tubule were tabulated by Frömter and Diamond (18). Hence, it is quite evident that a model of epithelial interspaces should include a nonzero ion and water permeability for the tight junction.

As for the second assumption, there is little evidence that would indicate a highly localized region of active transport. The predominance of mitochondria near the luminal end of the cell in rabbit gallbladder (39) is not a compelling reason to restrict active solute pumping to the apical end of the channel. In fact, in mammalian proximal tubule there is a predominance of mitochondria in the basolateral region of the cell (29). Furthermore, Stirling (38) has shown a uniform distribution of ATPase along the lateral and basal cell membranes in labeled ouabain autoradiographs of the rabbit intestine. Using lead sulfate precipitation to mark ATPase sites in frog skin membranes, Farquhar and Palade found uniform staining along the intercellular spaces throughout the epidermis (15). These pieces of evidence suggest that a selective localization of solute pumps at the luminal end of the interspace is highly unlikely.

This paper first reexamines Diamond and Bossert's model. Second, we

discuss how a model of this type can be modified to describe concentration profiles for the *Necturus* proximal tubular epithelium, interstitial region, and capillaries. Third, we propose an electrochemical compartment model for the proximal tubule and peritubular space. The effects of parameter variations are considered as well as possible mechanisms for the control of salt and water reabsorption during volume expansion.

GLOSSARY OF SYMBOLS

Superscripts and Subscripts

Many of the quantities used in both models are specified by a particular set of superscripts and subscripts. Superscripts indicate either the respective barriers or the compartments 1–5 (see Fig. 10):

α Effective tight junction barrier
β Lateral cell membrane
γ Luminal cell membrane
δ Effective barrier comprising the basal end of the channel and basement membrane
ϵ Capillary endothelium
te Denotes an experimentally observed quantity measured across the entire tubular epithelium
(1) Lumen
(2) Cell
(3) Interspace
(4) Peritubular space
(4δ) Region of peritubular space immediately adjacent to the δ barrier, see Fig. 10 B
(4ϵ) Region of peritubular space immediately adjacent to the ϵ barrier, see Fig. 10 B
(5) Capillary

Subscripts indicate chemical species or water:

s Solute considered as the neutral salt NaCl
Na Sodium ion
Cl Chloride ion
an Univalent anions other than Cl^-
cat Univalent cations other than Na^+
v Solvent flow, which is used interchangeably with water flow

Coefficients

A^k Area of the k'th effective barrier per square centimeter epithelium (dimensionless)
$L_p{}^k$ Filtration coefficient (hydraulic conductivity) of the k'th barrier
$\omega_j{}^k$ Diffusion coefficient for species j across barrier k
$\sigma_j{}^k$ Reflection coefficient for species j across barrier k
$t_j{}^k$ Transference number of ion j across barrier k
$P_j{}^k$ Permeability coefficient of species j across barrier k, $(=\omega_j{}^k \cdot RT)$
z_j Valence of the j'th ion

Fluxes

J_j^k Flow of species j across barrier k (mmol $cm^{-2}s^{-1}$ for solutes, ml $cm^{-2}s^{-1}$ for water)

Φ_j^k Flow of species j across barrier k, equal to $J_j^k \cdot A^k$ (mmol or ml s^{-1}/cm^2 epithelium)

${}_{act}J_j^k$ Active transport of ion j across barrier k (mmol $cm^{-2}s^{-1}$)

R_j^k Fraction of the observed transepithelial flux which crosses the k'th barrier, equal to (Φ_j^k/Φ_j^{te})

Concentrations, Pressures, and Potentials

C_j^k Concentration of species j in compartment k

$\bar{C}_j^k$ Average concentration of species j in barrier k, (taken as the arithmetic mean of the concentrations on the two sides of the membrane)

ΔC_j^k Concentration difference of species j across barrier k for positive flow from 1 to 2, $\Delta C_j^k = C_j^{(1)} - C_j^{(2)}$

π^k Protein osmotic pressure difference across barrier k for positive flow from 1 to 2, $\Delta\pi^k = \pi^{(1)} - \pi^{(2)}$

p^k Hydrostatic pressure in compartment k

Δp^k Hydrostatic pressure difference across barrier k for positive flow from 1 to 2, $\Delta p^k = p^{(1)} - p^{(2)}$

Ψ^k Electrical potential in compartment k

$\Delta\Psi^\gamma$ Luminal cell membrane potential $= \Psi^{(1)} - \Psi^{(2)}$

$\Delta\Psi^\beta$ Peritubular cell membrane potential $= \Psi^{(2)} - \Psi^{(3)}$ where $\Psi^{(3)} = \Psi^{(4)} = \Psi^{(5)}$

$\Delta\Psi^\alpha$ Transepithelial potential $= \Psi^{(1)} - \Psi^{(3)}$ where $\Psi^{(3)} = \Psi^{(4)} = \Psi^{(5)}$

Quantities Specific for the Continuous Model

x Direction along the length of the interspace. The x axis is orthogonal to the tubular axis

y Direction defined as orthogonal to the x axis and normal to the lateral cell membrane

z Direction defined as orthogonal to the x and y axes and parallel to the lateral cell membrane

$x = 0$ Apical end of the interspace immediately adjacent to the tight junction barrier

$x = L$ Basal end of the interspace

$x = M$ Location of the outside capillary wall

$x = N$ Location of the inside capillary wall

L Effective length of the interspace (along the x axis)

l Total linear length of cellular circumference per square centimeter cellular epithelium (along the z axis)

W_t Width of the tight junction (along the y axis)

W_i Width of the interspace (along the y axis)

$v(x)$ Solvent linear velocity at x

$A(x)$ Cross-sectional area at x, available for salt and water flux, per square centi-

meter epithelium. Area is in a plane normal to the x axis. ($A(x)$ is dimensionless.)

$D(x)$ Effective diffusion coefficient at x

$J_v(x)$ Volume flow at x, (ml $s^{-1}cm^{-2}$)

$J_s(x)$ Solute flow at x, (mmol $s^{-1}cm^{-2}$)

$\Phi_v(x)$ Volume flow at x, (ml s^{-1}/cm^2 epithelium) $= J_v(x) \cdot A(x)$

$\Phi_s(x)$ Salt flow at x, (mmol s^{-1}/cm^2 epithelium) $= J_s(x) \cdot A(x)$

C_o Luminal and plasma solute concentration

C_c Cell solute concentration

$C(x)$ Interspace or peritubular space solute concentration at x

$C(0) = C(x = 0)$ Solute concentration at the apical end of the interspace

$C(L) = C(x = L)$ Solute concentration at the basal end of the interspace

$C(M) = C(x = M)$ Solute concentration at the outside capillary wall

$C(N) = C(x = N)$ Solute concentration at the inside capillary wall, equal to the capillary salt concentration $= C_o$

Special Symbols

D Free solution salt diffusion coefficient for 100 mM solutions at 25°C

C_{emerg} Emergent concentration or predicted ratio of net solute to solvent flux

r_c Ratio of capillary surface area available for salt and water flux to histological capillary surface area

r_{Cl} Ratio of cellular chloride concentration to luminal chloride concentration

r_t Tight junction transference number ratio $= t^{\alpha}_{Cl}/t^{\alpha}_{Na}$

r_π Ratio of interstitial to capillary colloid osmotic pressure

$|\Delta x|$ Average path length through the capillary endothelium (centimeters)

F The Faraday constant = 96,500 C/mol

R Gas constant = 8.3 J $(°K)^{-1}$ mol^{-1}

REEVALUATION OF THE STANDING GRADIENT OSMOTIC MODEL

In Diamond and Bossert's original mode (13) the interspace is represented as a right cylindrical channel closed at the apical end with walls permeable to water but not solute (see Fig. 1 A). The length of the channel is L and the boundary condition at the open end is $C(x = L) = C_o$ where C_o is the standard luminal and bathing solution osmolarity. In order to have net reabsorption reasonably isosmotic, Diamond and Bossert confined the solute pumps to the first 10 μm of the channel (13).

A numerical analysis of Diamond and Bossert's model leads to two results which were not considered in their original paper (13). First, the standing gradient model predicts exact isotonicity of reabsorbate in only a few degenerate cases such as zero active transport and infinite channel wall water permeability. For example, a recalculation of the lower curve in Fig. 9 of reference 13 indicates that although the emergent concentration (closed circles) appears to approach 0.300 osM as solute input length decreases below 10 μm, it may actually extrapolate to a value of 0.2% hypertonic at

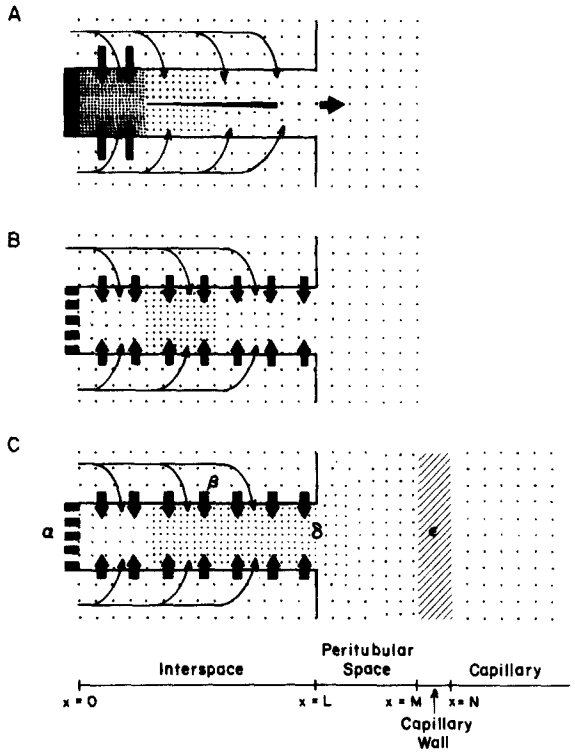

FIGURE 1. Diagram of the interspace models (continuous version). Vertical solid arrows represent solute pumps. Thin arrows represent water flow. Horizontal arrow represents interspace solute and water flow. The density of dots suggests the solute concentration. Luminal, cell, and capillary solute concentrations = C_o. (A) Diamond and Bossert's model (13). The tight junction region is impermeable. Solute pumps confined to the apical end of the channel produce a continuously decreasing solute concentration, leading to a slightly hypertonic reabsorption. (B) A permeable tight junction and solute pumps distributed uniformly along the lateral cell membrane results in a large hypertonicity and a significant violation of mass balance if $C(x = L) = C_o$. (C) A permeable tight junction and solute pumps distributed uniformly along the lateral cell membrane. $C(x = L) \neq C_o$ and solute mass balance is satisfied with $C(x = N) = C_o$. This is the "continuous model" discussed in the text.

zero input length. Exact isotonicity was never obtained with any physically meaningful set of parameters.

The second theoretical point is that Diamond and Bossert's model requires an unstirred layer at the end of the interspace. The reason for this follows from a description of the solute and volume flows at the basal end of the interspace:

$$\Phi_s(L) = A(L^-)\left[-D(L^-)\left.\frac{dC}{dx}\right|_{L^-} + C(L^-)\cdot v(L^-)\right], \quad (1)$$

$$\Phi_v(L) = A(L^-)\cdot v(L^-), \quad (2)$$

where L^- is the left-sided limit about the point L. The cross-sectional area, diffusion coefficient, linear velocity, and concentration are represented by A, D, v, and C, respectively.

The ratio of net solute to solvent flux, or emergent concentration, is given by:

$$C_{\text{emerg}} = \frac{\Phi_s(L)}{\Phi_v(L)} = C(L^-) - \frac{D(L^-)}{v(L^-)} \frac{dC}{dx}\bigg|_{L^-}. \tag{3}$$

Since the concentration must be continuous at the end of the interspace, $C(L^-) = C(L^+) = C(L) = C_o$ and reabsorption is isotonic only under conditions of osmotic equilibration where $(dC/dx)_{L^-} = 0$. Since Diamond and Bossert's profiles were all found to be at least slightly hypertonic (except for degenerate cases), $(dC/dx)_{L^-}$ is always <0.

Conservation of solute and volume at $x = L$ is represented by:

$$A(L^-)\left[v(L^-)\cdot C(L^-) - D(L^-)\frac{dC}{dx}\bigg|_{L^-}\right] = A(L^+)\left[v(L^+)\cdot C(L^+) - D(L^+)\frac{dC}{dx}\bigg|_{L^+}\right], \tag{4}$$

$$A(L^-)\cdot v(L^-) = A(L^+)\cdot v(L^+), \tag{5}$$

where L^+ is the right-sided limit about point L. Eqs. 4 and 5 imply:

$$\frac{dC}{dx}\bigg|_{L^+} = \frac{A(L^-)\cdot D(L^-)}{A(L^+)\cdot D(L^+)} \cdot \frac{dC}{dx}\bigg|_{L^-}. \tag{6}$$

Since $(dC/dx)_{L^-}$ is <0, $(dC/dx)_{L^+}$ must be <0 except in the limit of $A(L^+)$ or $D(L^+)$ approaching ∞. Consequently, the concentration cannot be uniform for $x > L$ and the region outside the mouth of the channel must be unstirred, with the degree of solute nonuniformity depending on the choice of parameters. This necessity for an unstirred layer was also recognized by Weinbaum and Goldgraben (43). If the region immediately outside the channel were well mixed, i.e. $(dC/dx)_{L^+} = 0$, it follows from Eq. 6 that the system violates mass balance.

Although it was not possible to develop a general proof that Diamond and Bossert's model (13) is always hypertonic, this could be done for the special case where solute input was uniform along the channel. The proof is important because a uniform distribution of active pumps is the case most consistent with available data.

It is assumed that C is continuous in the closed interval $[O, L]$ and dC/dx is continuous in the open interval (O, L). Either a permeable or impermeable tight junction region can be considered.

In order to osmotically transport water, the interspace must be hypertonic

to the lumen at some point, i.e., $C(x') > C_o$ for some x', $0 \leq x' < L$. (For an impermeable tight junction, $C(x = 0)$ is always $> C_o$ and x' can be 0.)

The concentration derivative at $x = 0$, $(dC/dx)_0$, is either equal to or greater than zero. Equality occurs for an impermeable tight junction as in Diamond and Bossert's model. A positive slope occurs for a permeable tight junction and always results in a local dilution at the start of the channel (see Appendix A).

Since $(dC/dx)_0 \geq 0$, $C(x') > C_o$, and $C(x = L) = C_o$, it follows that there must be some point, x_p, in the open interval (O, L) where the first and second derivatives of concentration are both less than zero. In Appendix B it is shown from the finite difference equations that the existence of such a point x_p requires: dC/dx and d^2C/dx^2 both <0 for all $x \geq x_p$. Hence the only possible class of concentration profiles are those which are monotonic decreasing and concave downward in the region $[x_p, L^-]$, where L^- is the left-sided limit about the point L. All these profiles have the end-point condition $(dC/dx)_{L^-} < 0$ (see Fig. 2).

There are several consequences of this end-point condition. First, $C(x = L)$

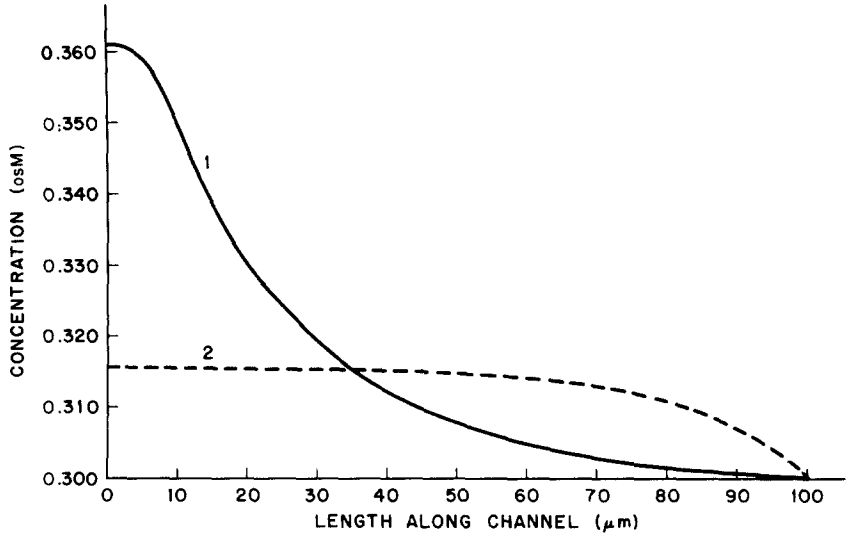

FIGURE 2. Examples of concentration profiles generated from Diamond and Bossert's model. The solute concentration is plotted against distance along the channel, x. In both profiles the active solute transport rate for the whole channel was held fixed at $2\pi r \cdot L \cdot 10^{-7}$ mosmol cm^{-2}. The water permeability, P_v^β was 2×10^{-5} cm s^{-1} osmol^{-1} l. (Curve 1) The active solute flux, ${}_{act}J_s^\beta$, was 10^{-6} mosmol cm^{-2} for $0 < x \leq 10$ μm and 0 for 10 μm $< x \leq 100$ μm. The predicted flux ratio (emergent concentration) was 0.307 osmol l^{-1}. (Curve 2) The active solute flux, ${}_{act}J_s^\beta$, was 10^{-7} mosmol cm^{-2} for $0 \leq x \leq 100$ μm. The flux ratio was 0.385 (0.300 is isotonic). In addition to predicting a hypertonic reabsorbate, both profiles violate mass balance at $x = L$. However, the degree of violation is much larger for curve 2.

$= C_o$ requires net reabsorption to be always hypertonic, i.e.,

$$C_{\text{emerg}} = \frac{\Phi_s(L)}{\Phi_v(L)} = C_o - \frac{D(L^-)}{v(L^-)} \frac{dC}{dx}\bigg|_{L^-} > C_o.$$

Second, it is also clear from Eq. 6 that the bathing solution at the mouth of the channel cannot be well stirred because $(dC/dx)_{L^+} < 0$. Third, none of these profiles are physiologically relevant because interstitial concentrations below C_o violate mass balance.[1]

In short, Diamond and Bossert's boundary condition, $C(x = L) = C_o$, leads to a class of concentration profiles which are not only hypertonically transporting but also physically unrealistic. Although the deviation from isotonicity and the degree of mass balance violation can be small if solute pumps are confined to the apical end of the channel, these deviations become quite significant for a uniform solute input along the channel (see Figs. 1 and 2). The only way to satisfy mass balance with models of this type is to replace the constraint that $C(x = L) = C_o$ with the boundary condition that solute concentration be C_o in the capillary. For isolated tubule preparations the bath concentration can be taken as C_o as long as there is some unstirred layer beyond the basal end of the interspace.

THE CONTINUOUS MODEL

Basic Outline for the Necturus Proximal Tubule

In view of the difficulties with Diamond and Bossert's model the analysis was rewritten with the following important differences: (*a*) The boundary condition that concentration at the end of the interspace equals C_o was replaced by the condition that the capillary concentration, $C(N)$, equals C_o. (*b*) Active transport of solute was uniformly distributed along the lateral cell

[1] The condition that $(dC/dx)_{L^+} < 0$ requires,

$$\Phi_s(L^+) = A(L^+)v(L^+)C(L^+) - A(L^+)D(L^+)\frac{dC}{dx}\bigg|_{L^+} > A(L^+)v(L^+)C(L^+),$$

as well as a decreasing concentration profile in the region beyond the interspace. Hence, the concentration at the outside of the capillary wall, $C(M^-)$, is $< C(L^+) = C_o$ where M^- is the left-sided limit about the point M. This, together with mass balance on volume flow: $A(L^+)v(L^+) = A(M^-)v(M^-) = A(M^+)v(M^+)$ requires, $A(L^+)v(L^+)C(L^+) > A(M^+)v(M^+)C(M^+)$ because $C(M^+) = C(M^-)$. Since $C(M^+)$ is $< C_o$ the concentration derivative at the capillary wall, $(dC/dx)_{M+}$, must be greater than zero. Hence,

$$A(M^+)v(M^+)C(M^+) > A(M^+)v(M^+)C(M^+) - A(M^+)D(M^+)\frac{dC}{dx}\bigg|_{M^+} = \Phi_s(M^+).$$

The above set of equations require $\Phi_s(L^+)$ to be always greater than $\Phi_s(M^+)$ thereby violating mass balance on solute.

membrane. (*c*) The tight junction region was considered permeable to solute and water with the hydraulic conductivity, L_p, the reflection coefficient σ, and the solute permeability, ω, estimated from overall transepithelial values for the *Necturus* proximal tubule. These determine the boundary conditions on v and dC/dx at the apical end of the interspace ($x = 0$). (*d*) The channel wall was permeable to NaCl where the salt permeability was estimated from ionic permeabilities. (*e*) The net volume flux leaving the interspace and crossing the capillary endothelium must equal the mean experimental *Necturus* reabsorptive flux. This condition is in sharp contrast with Diamond and Bossert's model (13) where no attempt was made to match the interspace volume flux with an experimentally observed flux characteristic of a particular epithelium. (*f*) The net solute flux leaving the mouth of the interspace must equal the solute flux calculated to be crossing the capillary wall. In order to investigate the degree of hypertonicity predicted by the models, the net solute flux was not constrained to equal the experimentally observed solute flux but was determined from Eq. 24 *c* of Appendix C.

The basic geometry for the continuous model is illustrated in Fig. 1 C. The intercellular channel is represented as a rectangular space of length L and width W_i. The use of rectangular rather than cylindrical geometry produces equations which are slightly different from those of Diamond and Bossert (13) although their form is similar. A complete description of the boundary conditions and differential equations is given in Appendix C. Justification of the parameter value used in this and the subsequent model is given in Appendix D.

Essentially, the tight junction region is treated as an effective membrane with specific permeability coefficients. Conservation of mass at $x = 0$ requires the initial values of v and dC/dx to be functions of $C(0)$ the initial concentration. The value of $C(0)$ together with the differential equations and lateral membrane coefficients determine concentration profiles for the interspace and peritubular space.

In this manner, a family of concentration profiles can be generated, each corresponding to a different initial concentration $C(0)$. However, profiles representing a solution to the boundary value problem must satisfy conditions (*e*) and (*f*). In order to satisfy these two conditions at least two quantities in the model had to be varied. Since no experimental data are available on $C(0)$ and ${}_{act}J_s^{\beta}$, these quantities were chosen as the two variables which characterize a concentration profile. Particular values of $C(0)$ and ${}_{act}J_s^{\beta}$ were found which would generate concentration profiles satisfying conditions *e* and *f* for a given set of independent parameters (Fig. 3 A and Table I).

The numerical calculations of the model, shown in Table II and Figs. 3, 5, 6, 7, 8, and 9, are based on a one-dimensional approach where the

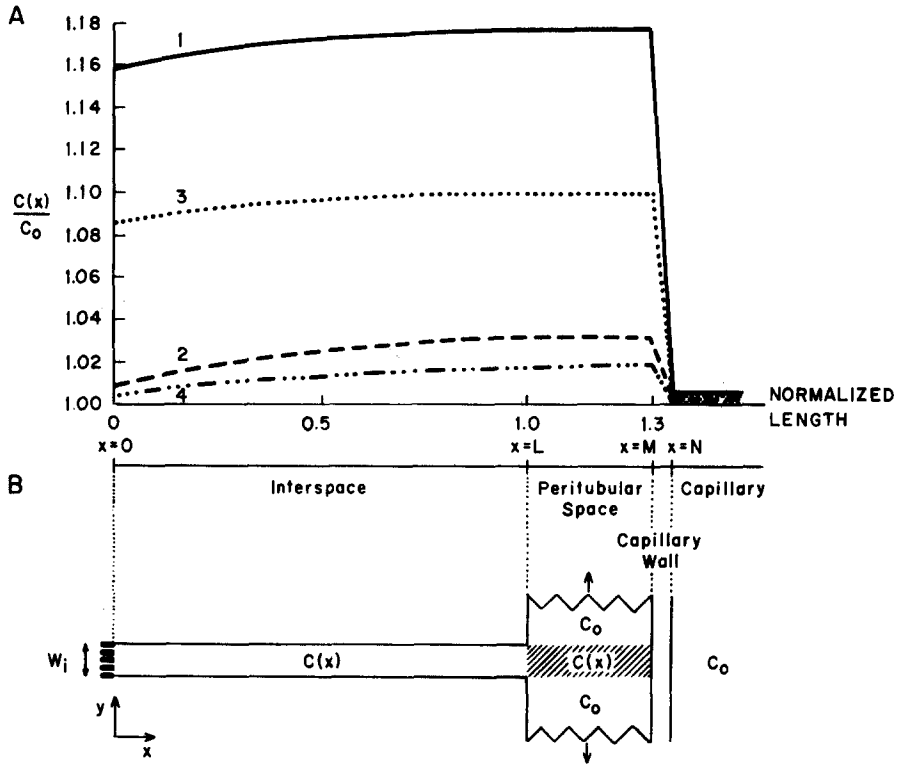

FIGURE 3. (A) Solute concentration profiles from a one-dimensional analysis (continuous model). Uniform distribution of solute pumps, a permeable tight junction and no solute dispersion (mixing) in the peritubular space were assumed. (Curve 1) Control *Necturus*, $L_p^{\alpha} = 6.10 \times 10^{-6}$ cm s^{-1} $(cmH_2O)^{-1}$. (Curve 2) Control *Necturus*, $L_p^{\alpha} = 2.60 \times 10^{-4}$ cm s^{-1} $(cmH_2O)^{-1}$. (Curve 3) Volume expanded *Necturus*, $L_p^{\alpha} = 6.10 \times 10^{-6}$ cm s^{-1} $(cmH_2O)^{-1}$. (Curve 4) Volume expanded *Necturus*, $L_p^{\alpha} = 2.60 \times 10^{-4}$ cm s^{-1} $(cmH_2O)^{-1}$. (B) The schematic geometry used for the calculation of the peritubular concentration profiles in the one-dimensional analysis (Fig. 3 A). There is assumed to be no interaction or mixing between the shaded band of fluid and the surrounding bulk of peritubular space, which is taken as isosmotic to capillary plasma.

differential equations consider only the x dependence of concentration (see Appendix C). A one-dimensional analysis of this kind cannot predict the precise mixing of solute which would occur as fluid from the interspace enters the peritubular space. Consequently, the concentration profiles of Fig. 3 A were calculated by having a band of fluid which originates from the interspace extend into the peritubular region. This is illustrated in Fig. 3 B. There is no interaction between the shaded band of fluid and the surrounding bulk of peritubular space which is assumed to be isosmotic to capillary plasma. These assumptions do not apply to the two-dimensional profile illustrated in Fig. 4.

TABLE I

CONTINUOUS MODEL: SUMMARY OF INDEPENDENT PARAMETERS

Constant quantities obtained from experimental data

$A^{\delta} = 4 \times 10^{-3}$ cm^2/cm^2 epithelium

$\omega_s^{\alpha} = \begin{cases} 1.52 \times 10^{-7} \text{ cm s}^{-1} \text{ mmol cm}^{-3} (\text{cmH}_2\text{O})^{-1} \text{ (control)} \\ 4.56 \times 10^{-7} \text{ cm s}^{-1} \text{ mmol cm}^{-3} (\text{cmH}_2\text{O})^{-1} \text{ (volume expansion)} \end{cases}$

$\omega_s^{\beta} = 3.0 \times 10^{-11}$ cm s^{-1} mmol cm^{-3} (cmH$_2$O)$^{-1}$

$\sigma_s^{\alpha} = 0.7$

$\sigma_s^{\beta} = 1.0$

$\Phi_v^{te} = \begin{cases} 1.64 \times 10^{-6} \text{ ml s}^{-1}/\text{cm}^2 \text{ epithelium (control)} \\ 0.91 \times 10^{-6} \text{ ml s}^{-1}/\text{cm}^2 \text{ epithelium (volume expansion)} \end{cases}$

$\Phi_s^{te} = \begin{cases} 1.64 \times 10^{-7} \text{ mmol s}^{-1}/\text{cm}^2 \text{ epithelium (control)} \\ 0.91 \times 10^{-7} \text{ mmol s}^{-1}/\text{cm}^2 \text{ epithelium (volume expansion)} \end{cases}$

$\Delta P^{\alpha} = 0.2$ cmH$_2$O

$(M\text{-}N)/L = 0.3$

$l = 800$ cm/cm^2 epithelium

$W_l = 25 \times 10^{-8}$ cm

$W_i = 5 \times 10^{-6}$ cm

$C_o = 100$ mM

$C_c = C_o$

$C(N) = C_o$

$D = 1.48 \times 10^{-5}$ cm^{2}s^{-1}

$|\Delta x| = 1 \times 10^{-4}$ cm

$RT = 2.53 \times 10^4$ cmH$_2$O cm^3 mmol^{-1}

Quantities varied over a range of experimentally observed values

L_p^{α} From 6.10×10^{-6} to 2.60×10^{-4} cm s^{-1} (cmH$_2$O)$^{-1}$, shown in Figs. 5, 7. Standard values: 6.10×10^{-6} cm s^{-1} (cmH$_2$O)$^{-1}$ and 2.60×10^{-4} cm s^{-1} (cmH$_2$O)$^{-1}$ (Table II and Fig. 3 A).

L_p^{β} From 2.8×10^{-10} to 28×10^{-10} cm s^{-1} (cmH$_2$O)$^{-1}$, shown in Figs. 6, 7. Standard value = 2.8×10^{-10} cm s^{-1} (cmH$_2$O)$^{-1}$.

L From $L = 25$ μm to $L = 60$ μm, shown in Fig. 8. Standard value = 25 μm.

r_c From 0.0002 to 0.002, shown in Fig. 9. Standard value = 0.001.

A complete definition of all symbols is given in the Glossary. Justification of all independent parameters is given in Appendix D.

Standard Concentration Profiles

As shown in Tables I and II, two classes of parameters are considered in the continuous model of the *Necturus* proximal tubule: independent and dependent. The set of independent parameters consists of: (*a*) constant quantities which are obtained from experimental data, (*b*) quantities which are varied over a range of experimentally observed values. The set of independent parameters is justified in Appendix D. The dependent parameters in Table II were determined from the constraint equations discussed in Appendix C.

Under control conditions with a low tight junction L_p, column 1 of Table II shows an interspace salt concentration increasing from 115.8 mM at the apical end to 117.5 mM at the basal end. The emergent concentration, defined as the solute to solvent flux ratio at the mouth of the channel, is 115.2 mM, where 100 mM is isosmotic with *Necturus* plasma. As shown in Fig. 3 A, the concentration profiles generated by this model are more uniform

TABLE II

CONTINUOUS MODEL: SUMMARY OF DEPENDENT PARAMETERS

	Control		Volume expansion	
	(1)	(2)	(3)	(4)
L_p^α, $cm\ s^{-1}\ (cm\ H_2O)^{-1}$	6.1×10^{-6}	2.6×10^{-4}	6.1×10^{-6}	2.6×10^{-4}
Predicted concentrations				
$C(x = 0)$, mM	115.8	100.8	108.6	100.5
$C(x = L)$, mM	117.5	103.0	109.9	101.7
C_{emerg}, mM	115.2	102.6	111.3	101.9
Predicted fluxes				
${}_{act}J_s^\beta$, $mmol\ cm^{-2}s^{-1}$	7.35×10^{-8}	3.44×10^{-8}	4.67×10^{-8}	1.93×10^{-8}
Φ_v^α, $ml\ s^{-1}/cm^2$ *epithelium*	6.83×10^{-7}	1.51×10^{-6}	3.71×10^{-7}	8.37×10^{-7}
Φ_v^β, $ml\ s^{-1}/cm^2$ *epithelium*	9.59×10^{-7}	1.30×10^{-7}	5.39×10^{-7}	7.17×10^{-8}
Φ_v^δ, $ml\ s^{-1}/cm^2$ *epithelium*	1.64×10^{-6}	1.64×10^{-6}	9.10×10^{-7}	9.10×10^{-7}
Φ_s^α, $mmol\ s^{-1}/cm^2$ *epithelium*	-2.19×10^{-9}	4.43×10^{-8}	-2.80×10^{-8}	2.31×10^{-8}
Φ_s^β, $mmol\ s^{-1}/cm^2$ *epithelium*	1.91×10^{-7}	1.24×10^{-7}	1.29×10^{-7}	6.96×10^{-8}
Φ_s^δ, $mmol\ s^{-1}/cm^2$ *epithelium*	1.89×10^{-7}	1.68×10^{-7}	1.01×10^{-7}	9.27×10^{-8}
Predicted flux ratios				
R_v^α	0.42	0.92	0.41	0.92
R_v^β	0.58	0.08	0.59	0.08
R_v^δ	1.00	1.00	1.00	1.00
R_s^α	−0.01	0.27	−0.31	0.25
R_s^β	1.16	0.76	1.42	0.77
R_s^δ	1.15	1.03	1.11	1.02

The dependent parameters are determined from the constraint equations in Appendix C.

along the x axis than those of Diamond and Bossert which show a large hump at the beginning of the channel followed by a rapid decline along the interspace (13). The uniformity of concentration parallels the uniform distribution of solute pumps. In addition, a permeable tight junction produces a dip in the concentration profile at the start of the channel due to a back diffusion of solute as well as solute dilution by the incoming water flux. Under control conditions an active transport rate of 7.35×10^{-8} mmol cm^{-2} s^{-1} all along the lateral cell membrane was required to account for the experimentally observed tubular water reabsorption of the in vivo *Necturus* kidney. For the low L_p^α case, the fluxes in column 1, Table II indicate that 42% (R_v^α) of the observed transepithelial water flux enters the interspace across the tight junction and 1% (R_s^α) of the observed salt flux leaks back into the lumen across the tight junction.

The assumption of a high L_p for the tight junction leads to a lower interspace salt concentration as shown in column 2, Table II ranging from 100.8 mM at $x = 0$ to 103.0 mM at $x = L$ with an emergent concentration of 102.6 mM. The dip in the interspace concentration profile is more pronounced than in the low L_p case (Fig. 3 A). As shown in column 2, Table II the high

L_p predicts that 92% of the observed transepithelial water flux and 27% of the net salt flux enter the interspace across the tight junction. There is no back leak of salt for this case. Since the high L_p condition predicts a net influx of salt across the tight junction, a lower value of active solute transport across the lateral cell membrane is required (3.44×10^{-8} mmol cm^{-2} s^{-1}).

In a one-dimensional analysis with no solute dispersion, the peritubular space profiles (Fig. 3 A between $x = L$ and $x = M$) apply only to a small band of fluid with width W_i and length $[L, M]$, (Fig. 3 B). Such a narrow zone of hypertonic solution would not occur in a real system if the interval $[L, M]$ is long enough. Even if it did occur, it would be impossible to detect and the peritubular space would appear practically isosmotic with plasma.

Under some conditions the concentration profile in this narrow band of fluid actually has a positive slope in $[L, M]$ indicating that it is slightly more hypertonic than the interspace. This depends on the relative magnitude of the convective and diffusional flows across the capillary wall.[2]

All the profiles in Fig. 3 A exhibit a prominent concentration drop across a small area of capillary endothelium. (In the remaining surface area the peritubular fluid adjacent to the capillary wall is isosmotic with plasma.) The reason for this drop is apparent from Eqs. 19 *c* and 22 *c* of Appendix C. Since $\Phi_s(M^+) = \Phi_s(M^-)$ and $C(M^+)\cdot v(M^+)\cdot A(M^+) = C(M^-)\cdot v(M^-)\cdot A(M^-)$, the right- and left-sided derivatives at $x = M$ are related by the expression:

$$-\left.\frac{dC}{dx}\right|_{M^+} = \frac{A(M^-)\cdot D(M^-)}{A(M^+)\cdot D(M^+)} \cdot \left[-\left.\frac{dC}{dx}\right|_{M^-}\right], \tag{7}$$

[2] In the continuous model, the sign of the concentration derivative $(dC/dx)_{M^-}$ at the outer surface of the capillary wall can be determined from the equations of Appendix C. Applying Eqs. 23 *c* and 25 *c* to Eq. 19 *c*:

$$\Phi_s(M^-) = -D\cdot A(L)\left.\frac{dC}{dx}\right|_{M^-} + C(M)\cdot r_c\cdot v(M^+)\cdot A(L).$$

Combining this with Eq. 24 *c* and solving for the concentration derivative ($\sigma_s{}^e = 0$):

$$\left.\frac{dC}{dx}\right|_{M^-} = [(v(M^+)/2D) - |\Delta x|^{-1}]\cdot[C(M) - C(N)]\cdot r_c.$$

As long as there is an inward directed concentration gradient across the capillary endothelium, $C(M)$ is $> C(N)$. Since r_c is > 0, the sign of $(dC/dx)_{M^-}$ depends on the relative magnitudes of $v(M^+)/2D$ and $|\Delta x|^{-1}$. Using the standard data discussed in Appendix D,

$$v(M^+) = \Phi_v^{t,e}/(r_c\cdot A^\delta) = 0.41 \text{ cm s}^{-1} \quad \text{and} \quad 0.23 \text{ cm s}^{-1},$$

for control and volume expansion, respectively, whereas $2D/|\Delta x| = 0.30$ cm s^{-1}. Hence, $(dC/dx)_{M^-}$ will be positive under control conditions but negative during volume expansion.

where M^- is the location just outside the capillary wall, and M^+ is the location just within the capillary wall. From studies by Landis and Pappenheimer (27) only a small fraction of the capillary surface area is available for diffusion, $A(M^+) \ll A(M^-)$. In a pore model of solute entry, the NaCl diffusion coefficient within a capillary pore is probably close to that in free solution, i.e., $D(M^+) \simeq D(M^-) = D$. Hence, Eq. 7 implies that there will be a discontinuity in the concentration derivative where $-dC/dx \mid_{M^+} \gg -dC/dx \mid_{M^-}$ which leads to a sharp drop in concentration across the capillary wall.[3]

It seems intuitive that solute mixing will dissipate the narrow band of hypertonic peritubular fluid indicated by the shaded region in Fig. 3 B. Goldgraben and Weinbaum (20) have evaluated the mixing pattern for a low Reynolds number jet entering a quiescent bathing solution. However, they do not consider the effects of an adjacent capillary bed which would greatly perturb the concentration profiles.

Although we have not yet evaluated the exact two-dimensional concentration profile in the peritubular space, an approximate solution is illustrated in Fig. 4 where solute concentration is plotted as a function of location in the x-y plane. Fig. 4 is based on the line source approximation for the convection of heat in a stream of fluid (26, 53). The *interspace* concentration is uniform in the y direction and hypertonic to the cell. There is a drop in concentration as hypertonic fluid from the interspace diffuses into the relatively isotonic peritubular space. Some concentration drop probably occurs at the capillary wall although it is undoubtedly smaller than the concentration drop shown in Fig. 3 A.

A concentration gradient across the capillary wall will not lead to reverse water flux out of the capillary because the salt reflection coefficient of the capillary endothelium is taken as 0 so that the effective osmotic force $2\sigma RT\Delta C_s$, is zero. Mass balance at the inner surface of the capillary wall can be satisfied only if it is assumed that the diffusive flux arising from the concentration drop across the capillary wall is removed by rapid capillary flow in the y direction.

[3] At the boundary between interspace and peritubular space ($x = L$) an abrupt widening in the y direction can be considered with the understanding that concentration at any point beyond $x = L$ is still independent of position along the y axis (this is the basic assumption of a one-dimensional analysis.) From continuity of solute concentration at $x = L$, it follows that at the point of abrupt increase in area the peritubular space concentration facing the cell will equal the end interspace concentration. Since a one-dimensional analysis does not predict much of a concentration drop in the region $[L, M]$, there will still be a relatively steep concentration gradient across the capillary surface area. A large value of $A(L^+)$, which equals $A(M^-)$, produces a large diffusion flux across the capillary wall and hence a large net solute to solvent flux ratio. This dependence of the flux ratio on $A(L^+)$ is an artifact which arises from treating the two-dimensional problem of peritubular space solute dispersion by a one-dimensional analysis. Since it is unrealistic to require peritubular space solute concentration to be homogeneous in the y direction over a distance larger than the width of the interspace, we assumed no cross sectional area expansion at $x = L$.

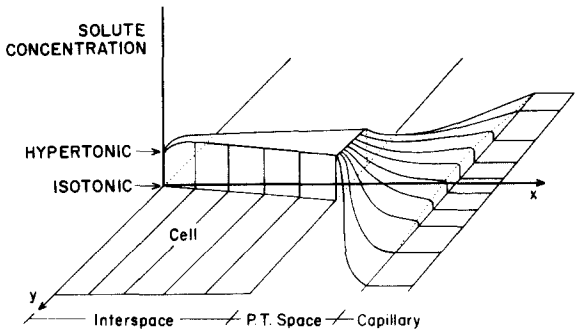

FIGURE 4. Solute concentration profiles from a two-dimensional analysis. Height above a particular point in the x-y plane denotes the solute concentration at that point. The profile is modified from the line source approximation (26, 53). Solute dispersion in the peritubular space leads to a lower average concentration drop across more of the capillary surface than in the one-dimensional analysis.

A drop in concentration across the tubular basement membrane could also occur although it is not considered in this model because the permeability properties of the *Necturus* basement membrane have not been studied. However, it is unlikely that the basement membrane offers an appreciable resistance to the flow of small solutes (44).

An important point about Figs. 3 and 4 is that the tonicity of reabsorbate, or ratio of solute to solvent flux at the capillary wall, is the same for both the one- and two-dimensional analyses used here. Since information about the two-dimensional concentration at the capillary wall is insufficient to uniquely determine the solute dispersion, the general technique was to calculate the solute to solvent flux ratio from the one-dimensional analysis and then select a two-dimensional profile with the same solute to solvent flux ratio that also satisfied the interspace boundary conditions at $x = L$.

Effects of Parameter Variations

The effects of volume expansion are shown in columns 3 and 4 of Table II and curves 3 and 4 of Fig. 3 A. Volume expansion was simulated by a decrease in observed transepithelial volume flux and a threefold increase in tight junction salt permeability based on experiments in our laboratory (7). The predicted *fractional* volume flux through the tight junction during saline diuresis was approximately the same as control values. For the low $L_p{}^{\alpha}$ assumption, volume expansion led to a decrease in interspace concentration (curve 3, Fig. 3 A), an increased back leak of salt from -1 to -31% (see $R_s{}^{\alpha}$, Table II) and a net transport which was slightly less hypertonic than control (111.3 mM vs. 115.2 mM). The model also predicted a 35% reduction in active transport rate associated with the volume expansion.

For the high $L_p{}^{\alpha}$ case, volume expansion also decreased the concentration

profile (curve 4, Fig. 3 A), but there was only a slight drop in the fraction of salt flux crossing the tight junction. A back leak of salt never occurred for the high L_p case because more salt was carried into the interspace by solvent drag than could leak back by diffusion. It will be shown subsequently in the compartment model that Na back leak is more pronounced if electrical driving forces are considered. For the high L_p^{α} case the predicted emergent concentration dropped from 102.6 to 101.9 mM during volume expansion. There was also a 44% decrease in active transport.

Curve 1 of Fig. 5 indicates the strong dependence of emergent concentration on the L_p of the tight junction. For $L_p^{\alpha} = 6.1 \times 10^{-6}$ cm s^{-1} $(cmH_2O)^{-1}$, the solute to solvent flux ratio is 115.2 mM which then drops off rapidly with a linear increase in L_p^{α}. For $L_p^{\alpha} > 7.0 \times 10^{-5}$ cm s^{-1} $(cmH_2O)^{-1}$ upwards of 85% of the volume flow crosses the tight junction, so that further increases in L_p^{α} can produce little change in the flow across the tight junction or in the emergent concentration.

Variations in the lateral cell membrane L_p are shown in curves 1 and 2 of Fig. 6. Increasing the L_p of the lateral cell membrane allows more water to enter the interspace thereby requiring a smaller degree of emergent hypertonicity to transport the same amount of water. The effect of the lateral cell membrane water permeability, L_p^{β}, is less pronounced when a higher tight junction L_p is assumed since a larger fraction of the net water flux enters the interspace across the tight junction (curve 2, Fig. 6).

From the shape of curve 1, Fig. 5 and curve 1, Fig. 6, it appears that L_p^{α} and L_p^{β} may have a similar effect on the solute to solvent flux ratio. The

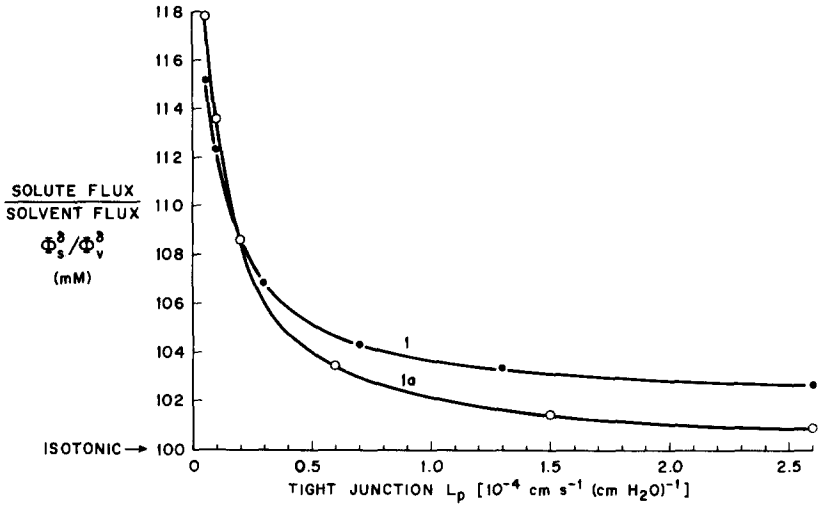

FIGURE 5. The effect of tight junction filtration coefficient, L_p^{α}, on the solute to solvent flux ratio (emergent concentration) for control *Necturus* data. (Curve 1 (●)) Continuous model. (Curve 1 *a* (○)) Compartment model.

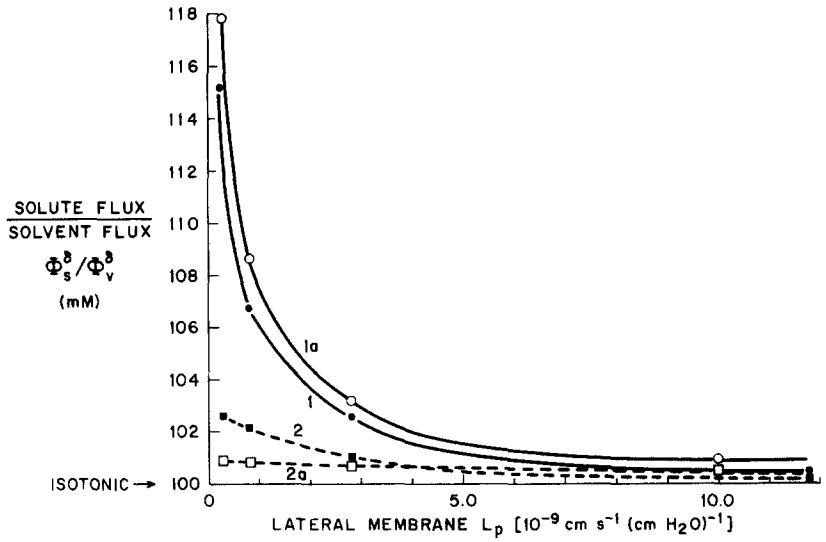

FIGURE 6. The effect of the lateral cell membrane coefficient, L_p^β, on the solute to solvent flux ratio (emergent concentration) for control *Necturus* data. (Curve 1 (●)) Continuous model, $L_p^\alpha = 6.10 \times 10^{-6}$ cm s^{-1} $(cmH_2O)^{-1}$. (Curve 2 (■)) Continuous model, $L_p^\alpha = 2.60 \times 10^{-4}$ cm s^{-1} $(cmH_2O)^{-1}$. (Curve 1 *a* (○)) Compartment model, $L_p^\alpha = 6.10 \times 10^{-6}$ cm s^{-1} $(cmH_2O)^{-1}$. (Curve 2 *a* (□)) Compartment model, $L_p^\alpha = 2.60 \times 10^{-4}$ cm s^{-1} $(cmH_2O)^{-1}$.

data are replotted in Fig. 7 as emergent concentration vs. the increase in L_p. The reference starting point for both L_p's (denoted by an asterisk) is given by the standard data of Table I and column 1 of Table II (emergent concentration = 115.2 mM). As shown in Fig. 7, variations in either L_p have a remarkably similar effect although a relative increase in the L_p of the lateral cell membrane (L_p^β) is slightly more effective in reducing the emergent concentration. Figs. 5 and 6 indicate that L_p^β is also more efficient in terms of the absolute change in L_p required to reduce the emergent concentration to a particular value.

The effect of postulating a longer interspace was also investigated. This is shown in Fig. 8 where $L = 25 \times 10^{-4}$ cm was taken as the standard value for the *Necturus* proximal tubule. For the low L_p^α case the solute to solvent flux ratio decreases with increasing interspace length (curve 1). As seen in curve 1, Fig. 3 A, the low L_p^α concentration profile shows only a slight percentage increase along the interspace. In this case, where most of the water flux crosses the lateral cell membrane, postulating a longer interspace lowers the predicted profile without appreciably affecting its shape because water enters uniformly across the increased length of lateral cell membrane. A lower concentration profile having the same shape as curve 1, Fig. 3 A produces a lower solute to solvent flux ratio. The gradual decline illustrated

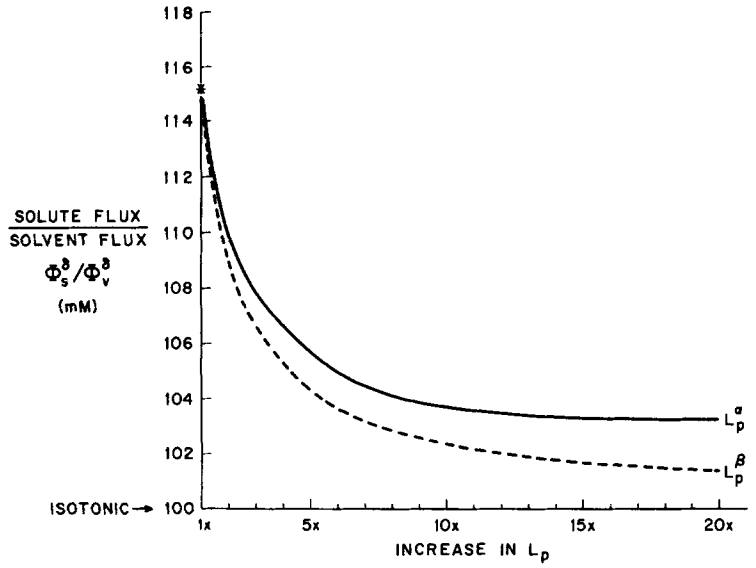

FIGURE 7. Comparison of the relative effects of L_p^α and L_p^β on the solute to solvent flux ratio (emergent concentration) for the continuous model. The reference point (*) is specified by the standard data in Table I and column 1 of Table II. (Solid line) Variations in L_p^α. (Dashed line) Variations in L_p^β.

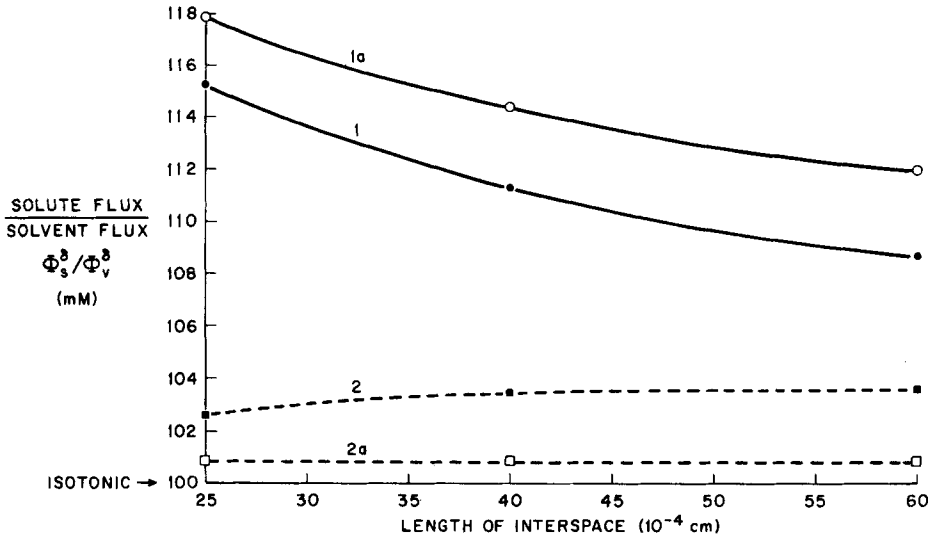

FIGURE 8. The effect of interspace length, L, on the solute to solvent flux ratio (emergent concentration) for control *Necturus* data. (Curve 1 (●)) Continuous model, L_p^α = 6.10 × 10^{-6} cm s^{-1} $(cmH_2O)^{-1}$. (Curve 2 (■)) Continuous model, L_p^α = 2.60 × 10^{-4} cm s^{-1} $(cmH_2O)^{-1}$. (Curve 1 *a* (○)) Compartment model, L_p^α = 6.10 × 10^{-6} cm s^{-1} $(cmH_2O)^{-1}$. (Curve 2 *a* (□)) Compartment model, L_p^α = 2.60 × 10^{-4} cm s^{-1} $(cmH_2O)^{-1}$.

in curve 1 of Fig. 8 indicates that large increases in interspace length would not have a dramatic effect on the emergent concentration.

For the case of a high L_p^{α} (curve 2, Fig. 8), there is actually a slight increase in emergent concentration with increasing interspace length. The reason for this can be seen from curve 2 of Fig. 3 A. Curve 2 shows about the same absolute increase with length as curve 1; however, the percentage increase is much larger because of its lower amplitude. It was found that increasing the interspace length accentuated the slope of this concentration profile because most of the water enters across the tight junction. Consequently, larger values of L generated lower values of $C(x = 0)$ but higher values of $C(x = L)$ than curve 2 (Fig. 3 A). Since the solute to solvent flux ratio or emergent concentration depends on the end interspace solute concentration (see Eq. 11 *c*, Appendix C), slight increases in $C(x = L)$ associated with increases in length L, lead to slightly larger emergent concentrations (curve 2, Fig. 8).

Variations in the parameters describing the capillary endothelium were also investigated (curve 1, Fig. 9). These capillary parameters affect the net solute flux across the capillary wall and, by mass balance, the net flux leaving the interspace as well as the concentration profile. (Solvent flux is always constrained to equal its experimentally observed value regardless of variations

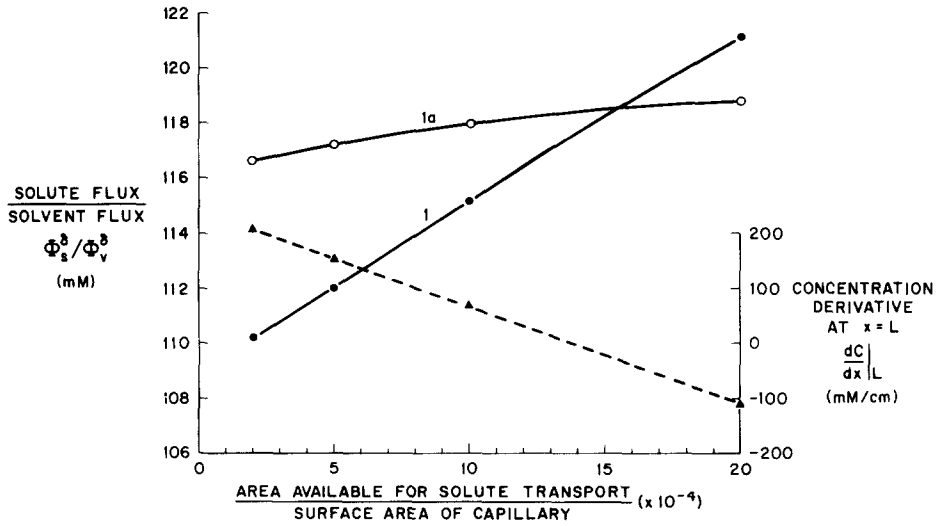

FIGURE 9. (Left ordinate) The effect of variations in the ratio of capillary area available for solute transport to histological capillary surface area, r_c, on the solute to solvent flux ratio (emergent concentration) for control *Necturus* data: (Curve 1 (●)) Continuous model, $L_p^{\alpha} = 6.10 \times 10^{-6}$ cm s^{-1} $(cmH_2O)^{-1}$. (Curve 1 *a* (○)) Compartment model, $L_p^{\alpha} = 6.10 \times 10^{-6}$ cm s^{-1} $(cmH_2O)^{-1}$. (Right ordinate) The effect of variations in r_c on the solute concentration derivative at the end of the interspace in the continuous model (dashed line, ▲).

in the model parameters.) All of the profiles predict an excess of solute over solvent leaving the interspace, but the larger the capillary resistance to solute flow, the closer the system will be to exact isotonicity. Or conversely, the greater the capillary area available for solute diffusion, the greater the hypertoncity of net transport.

Within a reasonable range, changes in the capillary wall diffusion coefficient and the capillary wall area available for salt and water transport have almost no effect on the actual shape of the interspace concentration profile. The changes in emergent hypertonicity shown in Fig. 9 (curve 1) are primarily associated with variations in the concentration derivative at $x = L$ which controls the diffusion flux at the end of the interspace. As shown by the dashed line in Fig. 9, the concentration derivative at $x = L$ is a linear function of r_c. Values of $r_c < 1.38 \times 10^{-3}$ lead to positive derivatives and the solute concentration in the shaded band of peritubular fluid shown in Fig. 3 B slightly exceeds the interspace solute concentration. For $r_c > 1.38 \times 10^{-3}$, the concentration derivative is negative and the solute concentration in the shaded band of Fig. 3 *b* is less than the interspace concentration.

THE COMPARTMENT MODEL

Basic Outline for the Necturus Proximal Tubule

Diamond and Bossert's model and our modified version of the interspace have neglected both hydrostatic pressures and the electrical potential difference as driving forces for salt and water. Appendix A and the Discussion examine some reasons for neglecting hydrostatic pressures in the *Necturus*. On the other hand, electrical driving forces in the *Necturus* proximal tubule may be as large or larger than RT times the concentration difference across the tight junction or lateral cell membrane. However, it is difficult to include electrical potentials in the continuous model.

Since interspace concentrations were found to be approximately uniform in the x direction (Fig. 3 A), we have developed a model which consists of separate homogeneous compartments for lumen (1), cell (2), interspace (3), peritubular space (4), and capillary (5), (see Fig. 10). This compartment model includes the basic driving forces of the continuous version with the following additions: (*a*) inclusion of electrical driving forces, (*b*) consideration of individual ionic fluxes rather than neutral salt fluxes, (*c*) inclusion of interactions between cell and interspace, where the flows and forces across both the luminal and lateral cell membranes are considered.

In Fig. 10 A the direction of the arrows defines positive flows although negative flows may also occur. The transcellular fluxes not entering the interspace were neglected because they introduce a number of unknown parameters which do not appreciably enhance the predictive power of the

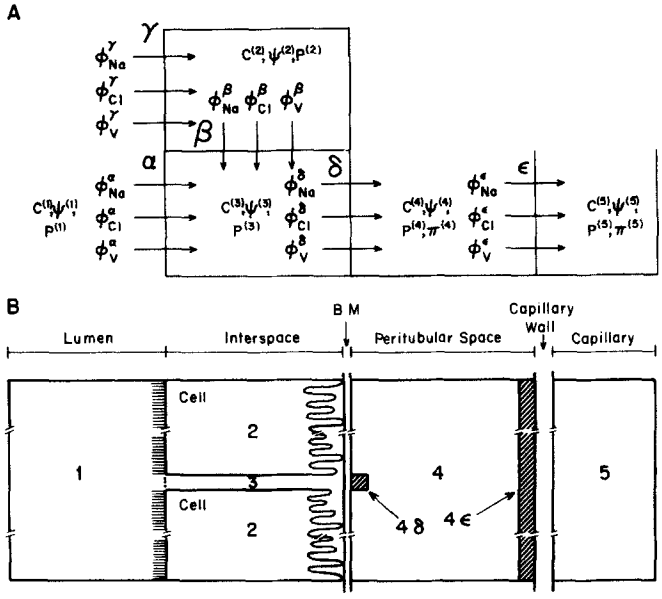

FIGURE 10. (A) The five-compartment model for Na^+, Cl^-, and water. α denotes the tight junction region, β the lateral cell membrane, γ the luminal membrane, δ the open end of the interspace and basement membrane, ϵ the capillary endothelium. C_j denotes concentration of ion j; p denotes hydrostatic pressure; Ψ denotes electrical potential; π denotes colloid osmotic pressure. The direction of the arrows indicates the convention chosen for positive fluxes Φ_j. (B) This figure illustrates the location and relative size of the subcompartments: 4δ and 4ϵ (shaded regions).

model. Furthermore, from the two-dimensional profile in Fig. 4 it appears that the effective peritubular space solute concentration adjacent to the basal cell membrane is probably very similar to the cell solute concentration except in the region near the mouth of the interspace. This would lead to very little osmotic driving force for water across the basal side of the cell. Spring (37) has also proposed a compartmental model which represents the *Necturus* epithelium as two parallel pathways for solute and water flow. His model was primarily designed to explain volume and solute flows induced by applied electric currents whereas the present treatment is concerned with the dependence of normal isotonic reabsorption on the transport parameters of the epithelium.

The compartment model was evaluated for a given set of parameters by simultaneously solving the mass balance equations for salt and volume flow as well as electroneutrality conditions. These are summarized in Table III. A detailed version of the equations as well as an outline of the complete solution is given in Appendix E. Each net flux, Φ_j^k, equals $J_j^k \cdot A^k$ where J_j^k is the flux of component j across membrane k per square centimeter of membrane and A^k is the area of membrane k per square centimeter epithelium.

TABLE III
COMPARTMENT MODEL: BASIC EQUATIONS

Mass balance on volume flow
(1) $\Phi_v^{\gamma} = \Phi_v^{\beta}$
(2) $\Phi_v^{\alpha} + \Phi_v^{\beta} = \Phi_v^{\delta}$
(3) $\Phi_v^{\delta} = \Phi_v^{\epsilon} = \Phi_v^{to}$

Mass balance on ion fluxes
(4) $\Phi_{Na}^{\gamma} = \Phi_{Na}^{\beta}$
(5) $\Phi_{Cl}^{\gamma} = \Phi_{Cl}^{\beta}$
(6) $\Phi_{Na}^{\alpha} + \Phi_{Na}^{\beta} = \Phi_{Na}^{\delta}$
(7) $\Phi_{Cl}^{\alpha} + \Phi_{Cl}^{\beta} = \Phi_{Cl}^{\delta}$
(8) $\Phi_{Na}^{\delta} = \Phi_{Na}^{\epsilon}$
(9) $\Phi_{Cl}^{\delta} = \Phi_{Cl}^{\epsilon}$

Electroneutrality
(10) $\Phi_{Na}^{\gamma} - \Phi_{Cl}^{\gamma} = \Phi_{Na}^{\beta} - \Phi_{Cl}^{\beta}$ (redundant)
(11) $\Phi_{Na}^{\gamma} - \Phi_{Cl}^{\gamma} = \Phi_{Cl}^{\alpha} - \Phi_{Na}^{\alpha}$ (redundant)
(12) $\Phi_{Na}^{\delta} = \Phi_{Cl}^{\delta}$

Φ_j^k is the net flux of species j across membrane k, $= J_j^k \cdot A^k$.
Units are ml s^{-1} for water and mmol s^{-1} for ions.

The standard Kedem-Katchalsky equations are used to describe volume and ionic flow (25). The volume flow across the kth barrier is:

$$J_v^k = L_p^k[\Delta P^k - \sum_j \sigma_j^k \cdot RT\Delta C_j^k - \Delta\pi^k]. \tag{8}$$

The first term is the hydrostatic pressure gradient, the second is the osmotic driving force, and the third is the colloid osmotic pressure which is assumed to apply only across the tubule basement membrane and capillary endothelium. The electroosmotic term is assumed to be negligible compared to the other driving forces.

Assuming no coupling between ions, the flux of the jth ion in the linear range is, according to Sauer (36): $J_j = (1 - \sigma_j)\,\overline{C}_j J_v + L_{jj}\Delta\tilde{\mu}_j + {}_{act}J_j$ where L_{jj} is the phenomenological straight coefficient relating J_j to its conjugate driving force, the electrochemical potential, $\Delta\tilde{\mu}_j$, which in turn can be expressed as:

$$\Delta\tilde{\mu}_j = (RT\Delta C_j/\overline{C}_j) + z_j F\Delta\Psi.$$

Hence,

$$J_j = (1 - \sigma_j)\overline{C}_j J_v + L_{jj}(RT\Delta C_j/\overline{C}_j) + L_{jj}z_j F\Delta\Psi + {}_{act}J_j\,.$$

The ionic permeability or diffusion coefficient is defined according to Kedem

and Leaf (25) as,

$$\omega_j = [J_j/RT\Delta C_j]_{\substack{J_v=0 \\ \Delta\Psi=0 \\ {}_{act}J_j=0}} = (L_{jj}/\bar{C}_j) = P_j/RT.$$

Therefore, the flux of ion j across barrier k is given by:

$$J_j^k = (1 - \sigma_j^k)\overline{C}_j^k \cdot J_v^k + RT\omega_j^k \cdot \Delta C_j^k + \omega_j^k \cdot \overline{C}_j^k \cdot z_j F \Delta\Psi^k + {}_{act}J_j^k. \quad (9)$$

Since the complete set of unknowns for the five barriers and five compartments is somewhat unwieldy, it was assumed for simplicity that the hydrostatic pressure driving forces are small compared to osmotic forces. As shown in Appendix A, osmotic forces dominate the flux equations unless the hydrostatic pressure gradients across the individual membranes exceed 180 mmH_2O which is two orders of magnitude larger than the entire transepithelial pressure gradient in the *Necturus* proximal tubule under control conditions. Although large interspace hydrostatic pressures cannot be ruled out a priori, it seems justified to neglect hydrostatic pressures in a preliminary treatment. Pressure terms can be included in the equations although this greatly complicates the process of finding a solution.

The compartment model was evaluated by finding a complete set of parameter values which is both reasonable and self-consistent. By assigning a range of values to parameters which are not precisely known, a range of values can be generated for the remaining parameters. Four examples of "solution sets" to the system of equations are shown in Tables IV and V.

Since the compartment model is a one-dimensional form of analysis, it cannot precisely describe the two-dimensional flow of solute in the peritubular space. Consequently, an approximation was developed similar to that used in the continuous model. The compartment model equations were first evaluated for the case of no solute dispersion (Table V); i.e. the peritubular space was represented as two discrete homogeneous sections: (*a*) a narrow band of fluid originating from the interspace and having a constant width, W_i, (in the continuous model this band is homogeneous in the y direction only. In the compartment model it is homogeneous in both x and y directions.) And (*b*) a surrounding bulk of fluid taken as isosmotic to capillary plasma. (This region is homogeneous in all directions.) These regions are shown in Fig. 3 B. There is assumed to be no interaction or flow between these two regions of fluid. The values of $C_{Na}^{(4)}$ and $C_{Cl}^{(4)}$ given in Table V represent the Na and Cl concentrations in the narrow band of fluid.

Solution Sets for Standard Data

As with the continuous model, the parameters can be divided into two classes: independent (Table IV) and dependent (Table V). The independent parameters consist of: (*a*) constant quantities which were obtained from

TABLE IV

COMPARTMENT MODEL: SUMMARY OF INDEPENDENT PARAMETERS

Constant quantities obtained from experimental data

$A^{\alpha} = 2 \times 10^{-4}$ cm^2/cm^2 epithelium

$A^{\gamma} = 20$ cm^2/cm^2 epithelium

$A^{\delta} = 4 \times 10^{-3}$ cm^2/cm^2 epithelium

$A^{\epsilon} = \begin{cases} A^{\delta} \text{ for Table V} \\ 1 \text{ cm}^2/\text{cm}^2 \text{ epithelium for Table VI} \end{cases}$

$L_p^{\gamma} = 2.8 \times 10^{-10}$ cm s^{-1} (cmH$_2$O)$^{-1}$

$\omega_{Na}^{\beta} = 3.44 \times 10^{-11}$ cm s^{-1} meq cm^{-3} (cmH$_2$O)$^{-1}$

$\omega_{Cl}^{\gamma} = 2.33 \times 10^{-10}$ cm s^{-1} meq cm^{-3} (cmH$_2$O)$^{-1}$

$\omega_{Na}^{\delta} = 1.04 \times 10^{-8}$ cm s^{-1} meq cm^{-3} (cmH$_2$O)$^{-1}$ ($\omega_{Na}^{\delta} = \omega_{Cl}^{\delta}$)

$\omega_{Na}^{\epsilon} = 5.85 \times 10^{-9}$ cm s^{-1} meq cm^{-3} (cmH$_2$O)$^{-1}$ ($\omega_{Na}^{\epsilon} = \omega_{Cl}^{\epsilon}$) (for $r_c = 1 \times 10^{-3}$)

$\sigma_s^{\alpha} = 0.7 \quad \sigma_s^{\beta} = 1.0 \quad \sigma_s^{\gamma} = 1.0 \quad \sigma_s^{\delta} = 0 \quad \sigma_s^{\epsilon} = 0$

$\sigma_{Na}^{\alpha} = 0.7 \quad \sigma_{Na}^{\beta} = 1.0 \quad \sigma_{Na}^{\gamma} = 1.0 \quad \sigma_{Na}^{\delta} = 0 \quad \sigma_{Na}^{\epsilon} = 0$

$\sigma_{Cl}^{\alpha} = 0.7 \quad \sigma_{Cl}^{\beta} = 1.0 \quad \sigma_{Cl}^{\gamma} = 1.0 \quad \sigma_{Cl}^{\delta} = 0 \quad \sigma_{Cl}^{\epsilon} = 0$

$\Phi_s^{te} = \begin{cases} 1.64 \times 10^{-6} \text{ ml s}^{-1}/\text{cm}^2 \text{ epithelium (control)} \\ 0.91 \times 10^{-6} \text{ ml s}^{-1}/\text{cm}^2 \text{ epithelium (volume expansion)} \end{cases}$

$\Phi_v^{te} = \begin{cases} 1.64 \times 10^{-7} \text{ mmol s}^{-1}/\text{cm}^2 \text{ epithelium (control)} \\ 0.91 \times 10^{-7} \text{ mmol s}^{-1}/\text{cm}^2 \text{ epithelium (volume expansion)} \end{cases}$

$C_s^{(1)} = 100$ mM

$C_s^{(5)} = 100$ mM

$C_{cat}^{(2)} = 70$ meq/liter

$\pi^{(5)} = \begin{cases} 9.29 \text{ cmH}_2\text{O (control)} \\ 3.48 \text{ cmH}_2\text{O (volume expansion)} \end{cases}$

$p^{(5)} = \begin{cases} 2.23 \text{ cmH}_2\text{O (control)} \\ 3.37 \text{ cmH}_2\text{O (volume expansion)} \end{cases}$

$\Psi^{(2)} = -70$ mV

$\Delta\Psi^{\alpha} = \Psi^{(1)} - \Psi^{(3)} = \begin{cases} -15.4 \text{ mV (control)} \\ -9.75 \text{ mV (volume expansion)} \end{cases}$

$\Delta\Psi^{\beta} = \Psi^{(2)} - \Psi^{(3)} = -70$ mV

$D = 1.48 \times 10^{-5}$ cm^{2}s^{-1}

$r_{Cl} = 0.3$

$r_t = 1.6$

$|\Delta x| = 1 \times 10^{-4}$ cm

$RT = 2.53 \times 10^4$ cmH$_2$O cm^3 (mmol)$^{-1}$

Quantities varied over a range of experimentally observed values

L_p^{α} From 6.10×10^{-6} to 2.60×10^{-4} cm s^{-1} (cmH$_2$O)$^{-1}$, shown in Tables V, VI, and Figs. 5, 7.

L_p^{β} From 2.8×10^{-10} to 2.8×10^{-9} cm s^{-1} (cmH$_2$O)$^{-1}$, shown in Table VII and Figs. 6, 7. Standard value = 2.8×10^{-10} cm s^{-1} (cmH$_2$O)$^{-1}$.

A^{β} From 4.0 cm^2/cm^2 epithelium ($L = 25$ μm) to 9.6 cm^2/cm^2 epithelium ($L = 60$ μm), shown in Table VIII and Fig. 8. Standard value = 4.0 cm^2/cm^2 epithelium ($L = 25$ μm).

$\sigma_{Na}^{\delta} = \sigma_{Cl}^{\delta}$ From 0 to 0.19, shown in Table IX. Standard value: $\sigma_{Na}^{\delta} = \sigma_{Cl}^{\delta} = 0$.

r_c From 2.0×10^{-4} to 2.0×10^{-3}, shown in Table X and Fig. 9. Standard value = 1.0×10^{-3}.

r_{π} From 0.26 to 0.77, shown in Table XI. Standard value = 0.43

A complete definition of all symbols is given in the Glossary. The values of the independent parameters are justified and explained in Appendix D.

TABLE V

COMPARTMENT MODEL: SUMMARY OF DEPENDENT PARAMETERS

	Control		Volume Expansion	
	(1)	(2)	(3)	(4)
L_p^{α}, $cm\ s^{-1}\ (cm\ H_2O)^{-1}$	6.10×10^{-6}	2.60×10^{-4}	6.10×10^{-6}	2.60×10^{-4}
Predicted concentrations				
$C_{Na}^{(2)}$ *meq/liter*	33.0	30.1	31.7	30.1
$C_{Cl}^{(2)}$ *meq/liter*	30.0	30.0	30.0	30.0
$C_{an}^{(2)}$ *meq/liter*	73.0	70.1	71.7	70.1
$C_{Na}^{(3)}$ *meq/liter*	118.1	100.9	110.1	100.5
$C_{Cl}^{(3)}$ *meq/liter*	118.1	100.9	110.1	100.5
$C_{Na}^{(4)}$ *meq/liter*	120.6	101.0	109.2	100.4
$C_{Cl}^{(4)}$ *meq/liter*	120.6	101.0	109.2	100.4
C_{emerg} *mM*	117.8	100.9	110.6	100.5
Predicted pressures*				
$\pi^{(4)}$ cmH_2O	4.0	4.0	1.5	1.5
$p^{(4)}$ cmH_2O	2.23	2.23	4.3	4.3
$p^{(3)}$ cmH_2O	2.23	2.23	5.0	5.0
Predicted coefficients				
L_p^{δ}, $cm\ s^{-1}\ (cmH_2O)^{-1}$	1.03×10^{-4}	1.03×10^{-4}	1.03×10^{-4}	1.03×10^{-4}
L_p^{ϵ}, $cm\ s^{-1}\ (cmH_2O)^{-1}$	7.73×10^{-5}	7.73×10^{-5}	7.73×10^{-5}	7.73×10^{-5}
ω_{Na}^{α} $cm\ s^{-1}\ meq\ cm^{-3}\ (cmH_2O)^{-1}$	9.57×10^{-8}	6.47×10^{-8}	2.92×10^{-7}	2.06×10^{-7}
ω_{Cl}^{α} $cm\ s^{-1}\ meq\ cm^{-3}\ (cmH_2O)^{-1}$	1.53×10^{-7}	1.04×10^{-7}	4.67×10^{-7}	3.30×10^{-7}
ω_s^{α} $cm\ s^{-1}\ meq\ cm^{-3}\ (cmH_2O)^{-1}$	5.89×10^{-8}	3.98×10^{-8}	1.80×10^{-7}	1.27×10^{-7}
ω_{Cl}^{β} $cm\ s^{-1}\ meq\ cm^{-3}\ (cmH_2O)^{-1}$	1.15×10^{-11}	8.00×10^{-12}	1.68×10^{-12}	3.35×10^{-13}
ω_{Na}^{γ} $cm\ s^{-1}\ meq\ cm^{-3}\ (cmH_2O)^{-1}$	1.96×10^{-12}	1.29×10^{-12}	1.41×10^{-12}	9.22×10^{-13}
Predicted ionic fluxes				
${}_{act}J_{Na}^{\beta}$ $meq\ cm^{-2}\ s^{-1}$	3.05×10^{-7}	2.51×10^{-7}	2.76×10^{-7}	2.42×10^{-7}
${}_{act}J_{Cl}^{\gamma}$ $meq\ cm^{-2}\ s^{-1}$	4.13×10^{-7}	4.11×10^{-7}	4.90×10^{-7}	4.89×10^{-7}
Φ_{Na}^{α} $meq\ s^{-1}/cm^2$ *epithelium*	-1.40×10^{-8}	2.86×10^{-8}	-5.86×10^{-8}	-1.25×10^{-8}
Φ_{Na}^{β} $meq\ s^{-1}/cm^2$ *epithelium*	2.07×10^{-7}	1.37×10^{-7}	1.60×10^{-7}	1.04×10^{-7}
Φ_{Na}^{δ} $meq\ s^{-1}/cm^2$ *epithelium*	1.93×10^{-7}	1.65×10^{-7}	1.01×10^{-7}	9.15×10^{-8}
Φ_{Cl}^{α} $meq\ s^{-1}/cm^2$ *epithelium*	6.10×10^{-8}	7.85×10^{-8}	8.18×10^{-8}	8.78×10^{-8}
Φ_{Cl}^{β} $meq\ s^{-1}/cm^2$ *epithelium*	1.32×10^{-7}	8.69×10^{-8}	1.88×10^{-8}	3.63×10^{-9}
Φ_{Cl}^{δ} $meq\ s^{-1}/cm^2$ *epithelium*	1.93×10^{-7}	1.65×10^{-7}	1.01×10^{-7}	9.15×10^{-8}
Predicted flux ratios				
R_v^{α}	0.48	0.98	0.48	0.98
R_v^{β}	0.52	0.02	0.52	0.02
R_v^{δ}	1.00	1.00	1.00	1.00
R_{Na}^{α}	−0.09	0.17	−0.64	−0.14
R_{Na}^{β}	1.27	0.84	1.75	1.15
R_{Na}^{δ}	1.18	1.01	1.11	1.01
R_{Cl}^{α}	0.37	0.48	0.90	0.96
R_{Cl}^{β}	0.81	0.53	0.21	0.05
R_{Cl}^{δ}	1.18	1.01	1.11	1.01

The dependent parameters are determined from the constraint equations in Appendix E.

* The following assumptions are required only for the calculation of $\pi^{(4)}$, $p^{(4)}$, and $p^{(3)}$: $r_{\pi} = 0.43 = [\pi^{(4)}/\pi^{(5)}]_{control} = [\pi^{(4)}/\pi^{(5)}]_{VE}$; $p^{(3)}$ (control) = $p^{(4)}$ (control) = $p^{(5)}$ (control).

experimental data; (*b*) quantities which were varied over a range of experimentally observed values. The independent parameters are justified in Appendix D. The equations used to determine the dependent parameters are explained in Appendix E. The predicted values of the dependent parameters are discussed below in order of their appearance in Table V.

SALT CONCENTRATIONS Both the luminal and capillary salt concentrations were chosen as 100 mM NaCl. Under these assumptions the constraint equations predict cell Na and Cl concentrations of about 30 meq/liter with Na slightly higher than chloride. The total cation or anion cell concentration varies between 100.1 and 103 meq/liter.

Since the model considers only the flow of Na and Cl ions, their interspace concentrations are identical. Assuming a low L_p for the tight junction (column 1, Table V), the interspace Na^+ concentration must be 118.1 meq/liter in order to account for the observed volume flux under control conditions. The solute to solvent flux ratio is 117.8 mM which is slightly larger than that predicted by the continuous model for the same $L_p{}^{\alpha}$.

The assumption of a high tight junction L_p (column 2, Table V) has a dramatic effect on the predicted interspace salt concentration. Under these conditions, the entire fluid reabsorption by the *Necturus* proximal tubule in control conditions could be explained by interspace Na^+ and Cl^- concentrations of only 100.9 meq/liter and a solute to solvent flux ratio of 100.9 mM. This small degree of hypertonicity in the flux ratio would be experimentally difficult to distinguish from isotonic reabsorption (100 mM). The peritubular space salt concentrations will be discussed later.

HYDROSTATIC AND COLLOID OSMOTIC PRESSURE Since the hydrostatic pressure difference between *Necturus* proximal tubular lumen and peritubular capillaries is only 0.26 cmH_2O under control conditions (21), it was arbitrarily assumed that the control interspace and peritubular space hydrostatic pressures were approximately equal to the capillary pressure, $p^{(5)}$. Hydrostatic pressure gradients could be included in the compartment model as indicated by Eqs. 1 *e* through 5 *e* of Appendix E. However, since there are no measurements of interspace hydrostatic pressures in any epithelium, its value could be between 0 and 10 cmH_2O (22). Estimates of cell hydrostatic pressure, $p^{(2)}$, and interspace hydrostatic pressure, $p^{(3)}$, could be used as independent input parameters in Eqs. 1 *e* through 4 *e* of Appendix E.

For Table V it was also assumed that the ratio of peritubular colloid osmotic pressure to capillary colloid osmotic pressure was 0.43 under control conditions (see Appendix D). Hence, the values of $p^{(3)}$, $p^{(4)}$, and $\pi^{(4)}$ in columns 1 and 2 of Table V are based solely on the experimentally observed values of $p^{(5)}$ and $\pi^{(5)}$.

COMPUTED COEFFICIENTS Since it was assumed that $p^{(3)} = p^{(4)} = p^{(5)}$ under control conditions and $\sigma_s{}^{\delta} = \sigma_s{}^{\epsilon} = 0$, the colloid osmotic pressure gradients across barriers δ and ϵ are the only driving forces for volume reabsorption in the compartment model. Hence, the values of $L_p{}^{\delta}$ and $L_p{}^{\epsilon}$ in Table V were calculated from the experimental control volume flux and the estimated colloid osmotic pressure gradient. Although this is an oversimplification, the effect of a small hydrostatic pressure gradient could be included without greatly affecting the magnitude of $L_p{}^{\delta}$ and $L_p{}^{\epsilon}$.

The calculated values of $L_p{}^{\delta}$ and $L_p{}^{\epsilon}$ shown in Table V compare reasonably well with the measured L_p's of the basement membrane and peritubular capillaries. From applied hydrostatic pressure experiments, Welling and Grantham found a basement membrane L_p of 8.8×10^{-5} cm s^{-1} $(cmH_2O)^{-1}$ in the rabbit proximal convoluted tubule (44). This is slightly lower than the value of $L_p{}^{\delta}$ given in Table V (1.03×10^{-4} cm s^{-1} $(cmH_2O)^{-1}$). Anagnostopoulos and Windhager measured 5×10^{-5} cm s^{-1} $(cmH_2O)^{-1}$ for the L_p of the rat peritubular capillaries (1). Again this is slightly lower, than the capillary endothelium $L_p{}^{\epsilon}$ predicted by the compartment model Table V (7.73×10^{-5} cm s^{-1} $(cmH_2O)^{-1}$). It should be noted that $L_p{}^{\delta}$ and $L_p{}^{\epsilon}$ were calculated from Eqs. 44 *e* and 45 *e* (Appendix E) which are essentially independent from the main set of coupled equations for the compartment model. Hence, the agreement of $L_p{}^{\delta}$ and $L_p{}^{\epsilon}$ with experimental measurements should not be construed as a verification of the entire model.

The tight junction salt permeability, $\omega_s{}^{\alpha}$, predicted by the compartment model under control conditions is from 2.5 to 4 times lower than the $\omega_s{}^{\alpha}$ used in the continuous model. This discrepancy arises mainly because the continuous model does not consider either electrical driving forces or individual ionic fluxes. Since the two models cannot be expected to have exactly the same $\omega_s{}^{\alpha}$, the only important point is that all control values of $\omega_s{}^{\alpha}$ lie below the upper limit of 3.0×10^{-7} cm s^{-1} mmol cm^{-3} $(cmH_2O)^{-1}$ calculated in Appendix D.

The values of ω_{Cl}^{β} and ω_{Na}^{α} predicted by the compartment model (Table V) are both more than one order of magnitude lower than the corresponding permeabilities calculated from Whittembury et al. (52) (see Appendix D). Since the experiments of Whittembury et al. cannot distinguish luminal cell membrane from lateral cell membranes, ω_{Cl}^{β} (Table V) should be $\simeq\omega_{Cl}^{\gamma}$ (Table IV) and ω_{Na}^{β} (Table IV) should be $\simeq\omega_{Na}^{\gamma}$ (Table V).

There are a number of ways the model could be modified so that it might predict Na^+ and Cl^- cell membrane permeabilities more consistent with the available data. The first possibility would be the inclusion of ion and water fluxes across the basal side of the cell. Since there are large electrochemical driving forces for Na across the luminal membrane (γ) which are proportional to ω_{Na}^{γ} and large electrochemical driving forces for Cl across the lateral

cell membrane (β) which are proportional to ω^{β}_{Cl}, values of ω^{γ}_{Na} and ω^{β}_{Cl} close to the data of Whittembury et al. (52) would increase the transepithelial Na and Cl fluxes by a factor of 10, whereas the volume flux would still equal the experimentally observed value. This would lead to an unreasonably large solute to solvent flux ratio independent of whether or not fluxes occurred across the basal side of the cell.

The second possibility is to assume a very low cellular Cl^- concentration which would reduce the electrochemical driving force for Cl^- out of the cell. However, this could at best increase the chemical gradient by a factor of 2 which would not offset the effect of a 10-fold increase in ω_{Cl}.

A third alternative is to postulate active ion pumps opposing the passive ion fluxes across the luminal (γ) and lateral (β) cell membranes. However, there is no evidence in the proximal tubule for active pumps with these orientations.

It is interesting that if the compartment model is recalculated with values of $\omega^{\gamma}_{Cl} = \omega^{\beta}_{Cl} = (1/20)\omega^{cell}_{Cl}$ (where $RT\omega^{cell}_{Cl}$ is the cell membrane Cl^- permeability obtained from [52]), the predicted ion permeabilities, ω^{γ}_{Na} and ω^{β}_{Na}, drop proportionately so that the ratio of ω_{Cl}/ω_{Na} for both luminal and lateral cell membranes is about 6.8 ($=\omega^{cell}_{Cl}/\omega^{cell}_{Na}$ from [52]). This indicates that if P^{cell}_{Na} and P^{cell}_{Cl} were both 20 times smaller than those measured in (52), they would be completely consistent with the compartment model.

ION AND WATER FLUXES Active Na^+ transport rates ($_{act}J^{\beta}_{Na}$) of 3.05 and 2.51 $\times$ 10^{-7} mmol cm^{-2} s^{-1} were required to account for the observed water reabsorption under the assumptions of low and high L_p^{α}, respectively. This is between four and seven times larger than the $_{act}J_s^{\beta}$ predicted by the continuous model although both models transport the same amount of water. The apparent inefficiency of the compartment model arises from a Na^+ backflux that is one order of magnitude larger in the compartment model than in the continuous model. This is mainly due to the inclusion of an electrical potential difference which leads to a large driving force for Na^+ from interspace to lumen in the compartment model. The absolute active transport rates of both models remain below the rough upper limit suggested by Diamond and Bossert of 5 $\times$ 10^{-7} mmol NaCl cm^{-2} s^{-1} (13).

The high negativity of the cell prevents Cl^- from diffusing passively across the luminal membrane except for very low cellular chloride concentrations. Hence, an active component of chloride flux was postulated to occur across the luminal membrane.

Fig. 11 and column 1, Table V indicate the ion and water fluxes across each barrier for the low L_p^{α} condition. In Fig. 11 the solid arrows represent a cellular pathway from lumen to interspace. The open arrows represent a paracellular path across the tight junction. Since the model assumes that all transport occurs via the interspace, the arrows across the luminal cell mem-

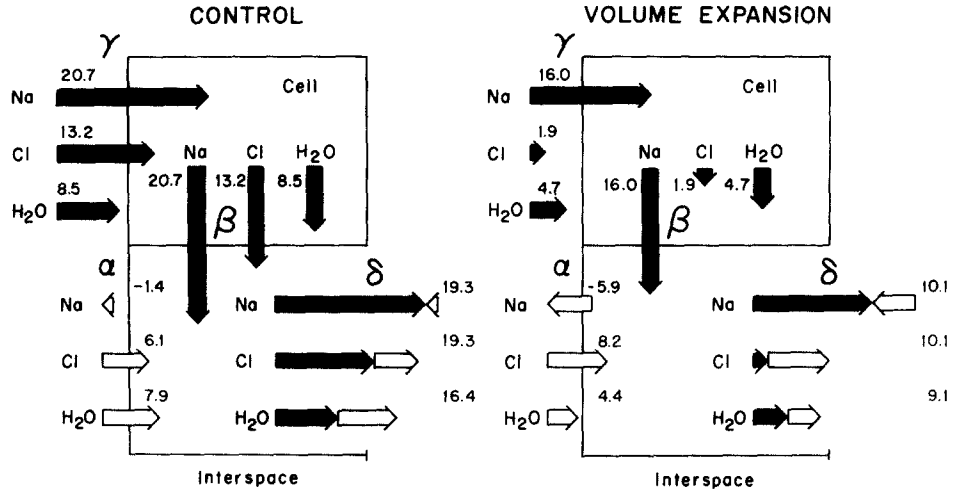

FIGURE 11. Ion and water fluxes for $L_p^{\alpha} = 6.1 \times 10^{-6}$ cm s^{-1} $(cmH_2O)^{-1}$. The left side illustrates the control condition; the right side illustrates volume expansion. Fluxes crossing the cell from lumen to interspace are indicated by solid arrows. Fluxes bypassing the cell are indicated by open arrows. The numbers indicate the magnitude of the net flux across each of the four barriers shown. Na^+ and Cl^- fluxes are in 10^{-8} mmol s^{-1}/cm^2 epithelium. Water fluxes are in 10^{-7} ml s^{-1}/cm^2 epithelium.

brane (γ) are identical to those across the lateral cell membrane (β). As shown in column 1 Table V, 52% of the observed water flux traverses the cellular path and 48% crosses the tight junction. This is similar to the continuous model which predicted values of 58 and 42%, respectively. All the interspace sodium enters from the cell. 7% of this "input flux" (Φ_{Na}^{β}) leaks back into the lumen across the tight junction. The remaining 93% leaves the interspace and is reabsorbed by the capillaries. The omission of electrical potential differences in the continuous model leads to a salt back leak of only 1% for the low L_p^{α} condition.

For the assumption of a high L_p^{α} (column 2, Table V) 98% of the observed water flux crosses the tight junction in the compartment model. Again, this is similar to the 92% predicted by the continuous model (R_v^{α}, column 2, Table II). There is no back leak of Na for the high L_p^{α} case because sodium is swept along with the large volume flow across the tight junction. $\Phi_{Na}^{\alpha} = 21\%$ Φ_{Na}^{β} for the compartment model as compared with $\Phi_s^{\alpha} = 36\%$ Φ_s^{β} for the continuous model. The difference in the two models is again due to the inclusion of an electrical potential difference across the tight junction. For both L_p^{α} conditions the compartment model predicts a net lumen to interspace Cl^- flux across the tight junction because the electrical potential difference and solvent drag terms are larger than the chemical driving force.

PERITUBULAR SPACE ION CONCENTRATIONS The values of peritubular

space ion concentrations, $C_{Na}^{(4)} = C_{Cl}^{(4)}$, apply only to the compartment indicated by the shaded region in Fig. 3 B which represents a narrow band of fluid with constant width W_i and length $[L, M]$. Mixing between this hypertonic band of fluid and the surrounding bulk of fluid at concentration C_o would produce a peritubular space which is inhomogeneous in both x and y directions (see Fig. 4). It is possible to estimate the degree of inhomogeneity in the x direction by using the compartment model to calculate: $C_{Na}^{(4\delta)}$, the peritubular space Na concentration immediately adjacent to barrier δ; and $C_{Na}^{(4\epsilon)}$, the peritubular space Na concentration immediately adjacent to barrier ϵ, where ϵ represents the entire effective capillary surface (A^ϵ = 1 cm²/cm² epithelium). The subcompartments 4δ and 4ϵ are illustrated in Fig. 10 B and the details of the calculation are given in Appendix E.

The effect of solute dispersion in the peritubular space is indicated by the values of $C_{Na}^{(4\delta)}$ and $C_{Na}^{(4\epsilon)}$ together with the interspace and capillary concentrations listed in Table VI. The ratio of solute to solvent flux is identical to that of Table V. Under control conditions the ion concentration just outside the interspace, $C_{Na}^{(4\delta)}$, is slightly above the interspace concentration $C_{Na}^{(3)}$. This is similar to the continuous model where the concentration derivative at $x = L$ is sometimes greater than zero. In both models the salt concentration just outside the interspace seems to depend on the transport properties of the capillary (Table X, Fig. 9) and the tubule basement membrane (Table IX).

The low value of $C_{Na}^{(4\epsilon)}$ indicates that a large concentration drop must have occurred between the end of the interspace and the outside of the capillary wall. This is consistent with the two dimensional concentration profile shown in Fig. 4. The capillary endothelial filtration coefficient, L_p^ϵ,

TABLE VI

COMPARTMENT MODEL: EFFECT OF PERITUBULAR SPACE SOLUTE DISPERSION ON SELECTED DEPENDENT PARAMETERS

L_p^α, $cm\ s^{-1}\ (cm\ H_2O)^{-1}$	6.10×10^{-6}	2.60×10^{-4}
C_{emerg} mM	117.8	100.9
$C_{Na}^{(3)} = C_{Cl}^{(3)}$ $meq/liter$	118.1	100.9
$C_{Na}^{(4\delta)} = C_{Cl}^{(4\delta)}$ $meq/liter$	120.6	101.0
$C_{Na}^{(4\epsilon)} = C_{Cl}^{(4\epsilon)}$ $meq/liter$	100.2	100.0*
$C_{Na}^{(5)} = C_{Cl}^{(5)}$ $meq/liter$	100.0	100.0
L_p^ϵ $cm\ s^{-1}\ (cmH_2O)^{-1}$	3.09×10^{-7}	3.09×10^{-7}

The independent parameters are given in Table IV (control conditions). Note that A^ϵ = 1 cm²/cm² epithelium for Table VI.

The only dependent parameters which are affected by peritubular space solute dispersion are: $C_j^{(4\delta)}$, $C_j^{(4\epsilon)}$, L_p^ϵ. Since ω_j^ϵ depends on r_c, it is unaffected by changes in A^ϵ (see Appendix D). Note that Eqs. 50 *e*, 51 *e* of Appendix E require $C_{Na}^{(4\delta)}$ of Table VI to equal $C_{Na}^{(4)}$ of Table V.

* Indicates a concentration slightly greater than 100.0 meq/liter.

is included in Table VI because, as pointed out in Appendix E, its predicted value depends on whether water reabsorption occurs across the entire capillary surface (A^{ϵ} = 1 cm²/cm² epithelium, Table VI) or just across a small region of capillary surface area ($A^{\epsilon} = A^{\delta}$, Table V).

Effect of Parameter Variations

For the compartment model, volume expansion was simulated by a decrease in transepithelial volume flux associated with both a decrease in $\pi^{(5)}$ and an increase in $p^{(5)}$. In addition, the transepithelial potential difference was altered from −15.4 to −9.75 mV and the tight junction salt permeability, $\omega_s{}^{\alpha}$, was increased by a factor of 3 based on experiments in our laboratory (7) (see Table IV).

The predicted *fractional* volume flux across the tight junction was unchanged during saline diuresis in both $L_p{}^{\alpha}$ conditions. For the low $L_p{}^{\alpha}$ assumption the interspace and peritubular space ion concentrations decreased during volume expansion and the ratio of solute to solvent flux dropped to 110.6 mM. This is similar to the ratio of 111.3 mM predicted by the continuous model (column 3, Table II). Under the assumptions discussed in Appendix E, the compartment model predicts a drop in peritubular space colloid osmotic pressure and a rise in both interspace and peritubular space hydrostatic pressure during volume expansion (column 3, Table V). There is an increased back leak of Na with R_{Na}^{α} shifting from −0.09 to −0.64 in addition to a 10% drop in active Na transport (see Fig. 11). This can be compared with the predictions of the continuous model where $R_s{}^{\alpha}$ shifted from −0.1 to −0.31 during volume expansion.

For the high $L_p{}^{\alpha}$ condition the interspace and peritubular space concentrations also decreased during volume expansion. The emergent concentration dropped to 100.5 mM which is close to that predicted by the continuous model under similar conditions. The predicted Na flux across the tight junction switched directions during volume expansion with R_{Na}^{α} going from +0.17 to −0.14. This differs from the continuous model where no back leak of salt was observed for the high $L_p{}^{\alpha}$ assumption. Indeed, Φ_{Na}^{α} (Table V) changes more during volume expansion than does $\Phi_s{}^{\alpha}$ because of the inclusion of an electrical potential difference across the tight junction in the compartment model.

The Cl^- flux in the compartment model always moves across the tight junction from lumen to interspace. During volume expansion the observed threefold increase in transepithelial conductance (7) predicts a tight junction Cl^- flux equal to 90% of the transepithelial Cl^- flux.

For the compartment model the dependence of emergent concentration on $L_p{}^{\alpha}$ is indicated by curve 1 *a* of Fig. 5. The shape of the curve is similar to curve 1, obtained with the continuous model. However, the compartment

model predicts a lower emergent concentration at high values of L_p^{α} because the concentration at the end of the interspace is lower in the compartment model due to the assumption of uniform concentrations.

The dependence of emergent concentration on L_p^{β} for the compartment model is indicated by curves 1 *a* and 2 *a* in Fig. 6. The curves are essentially similar to those obtained with the continuous model. As shown in Table VII, variations in L_p^{β} with a low value of L_p^{α} have a large effect on the fraction of transepithelial reabsorbate which crosses the tight junction.

If the dependence of emergent concentration on L_p^{α} and L_p^{β} is replotted as a function of the increase in L_p, the resulting curves would resemble Fig. 7 but lie closer together. (The emergent concentrations are 103.3 and 103.1 for a 10-fold increase in L_p^{α} and L_p^{β}, respectively.)

Fig. 8 illustrates the dependence of the predicted emergent concentration on the assumed interspace length (L). For the low L_p^{α} condition (curves 1 and 1 *a*) both models predict the same decline in the solute to solvent flux ratio for longer interspaces. It is interesting that for a low L_p^{α} even extremely long interspaces would not produce an isosmotic reabsorbate provided the solute pumps are distributed uniformly along the lateral cell membranes. For the high L_p^{α} condition (curve 2 *a*) the compartment model predicts a low emergent concentration that is essentially independent of the assumed interspace length. Table VIII indicates that the assumed interspace length has a moderate effect on the fraction of total volume flow crossing the lateral cell membrane.

Table IX illustrates the effects of a nonzero basement membrane salt reflection coefficient. If both σ_{Na}^{δ} and σ_{Cl}^{δ} are >0, sieving of solute takes place at the basement membrane. As a result, the Na and Cl concentrations in the

TABLE VII

COMPARTMENT MODEL: EFFECT OF VARIATIONS IN L_p^{β} ON SELECTED DEPENDENT PARAMETERS

L_p^{α}, *cm* s^{-1} (*cm* H_2O)$^{-1}$	6.10×10^{-6}			2.60×10^{-4}		
L_p^{β}, 10^{-10} *cm* s^{-1} (*cm* H_2O)$^{-1}$	2.8	8.4	28	2.8	8.4	28
Interspace concentration $C_{Na}^{(3)} = C_{Cl}^{(3)}$ *meq/liter*	118.1	108.9	103.2	100.9	100.8	100.7
Solute flux/solvent flux C_{emerg} *mM*	117.8	108.7	103.1	100.9	100.8	100.7
Volume flux ratios						
R_v^{α}	0.48	0.23	0.08	0.98	0.93	0.80
R_v^{β}	0.52	0.77	0.92	0.02	0.07	0.20
R_v^{δ}	1.00	1.00	1.00	1.00	1.00	1.00

The independent parameters are given in Table IV (control conditions). Results apply to the standard or control case for different values of L_p^{β}.

TABLE VIII

COMPARTMENT MODEL: EFFECT OF VARIATIONS IN INTERSPACE LENGTH

L_p^α, cm s^{-1} (cm H_2O)$^{-1}$	6.10×10^{-6}			2.60×10^{-4}		
L, μm	25	40	60	25	40	60
A^β, cm^2/cm^2 epithelium	4.0 (Std)	6.4	9.6	4.0 (Std)	6.4	9.6
Interspace concentration						
$C_{Na}^{(3)} = C_{Cl}^{(3)}$ meq/liter	118.1	114.7	112.1	100.9	100.9	100.8
Solute flux/solvent flux						
C_{emerg} mM	117.8	114.4	111.9	100.9	100.8	100.8
Volume flux ratios						
R_v^α	0.48	0.39	0.32	0.98	0.96	0.95
R_v^β	0.52	0.61	0.68	0.02	0.04	0.05
R_v^δ	1.00	1.00	1.00	1.00	1.00	1.00

The independent parameters are given in Table IV (control conditions). The value of A^β used in the compartment model corresponds to an interspace of length L.

TABLE IX

COMPARTMENT MODEL: DEPENDENCE OF THE NET SOLUTE FLUX RATIO ON THE BASEMENT MEMBRANE IONIC REFLECTION COEFFICIENT

Basement membrane ionic reflection coefficient, $\sigma_{Na}^\delta = \sigma_{Cl}^\delta$	0.0	0.05	0.10	0.15	0.17	0.19
Emergent concentration						
C_{emerg} mM	117.8	112.7	107.9	103.4	101.6	99.9
Peritubular space concentrations*						
$C_{Na}^{(4\delta)} = C_{Cl}^{(4\delta)}$ meq/liter	120.6	114.7	109.1	103.9	101.8	99.8
$C_{Na}^{(4\epsilon)} = C_{Cl}^{(4\epsilon)}$ meq/liter	100.2	100.2	100.2	100.1	100.0	100.0

For $\sigma_{Na}^\delta = \sigma_{Cl}^\delta$, $\sigma_s{}^\delta = \sigma_{Na}^\delta \cdot \omega_s{}^\delta \cdot [(\omega_{Na}^\delta)^{-1} + (\omega_{Cl}^\delta)^{-1}]$.

The independent parameters are given in Table IV. Interspace concentration required to account for control transepithelial volume flux: $C_{Na}^{(3)} = C_{Cl}^{(3)} = 118.1$ meq/liter with $L_p^\alpha = 6.10 \times 10^{-6}$ cm s^{-1} (cmH_2O)$^{-1}$. C_{emerg} was calculated from Eqs. 12 *e* and 14 *e* of Appendix E with $\sigma_{Na}^\epsilon = 0$ and $A^\epsilon = A^\delta$.

* Calculated from Eqs. 51 *e* and 53 *e*, where $A^\epsilon = 1$ cm^2/cm^2 epithelium.

4δ region (see Fig. 10 B) drop below their interspace concentrations, and the ratio of net solute to solvent flux decreases with increasing values of the reflection coefficient. A basement membrane ionic reflection coefficient of only 0.19 can produce isotonic transport even though the concentration of the interspace is 118 mM NaCl. Welling et al. (45) have suggested that the tubular basement membrane may affect the relative contribution of diffusive and convective flows, thereby influencing the ratio of solute to solvent flux. However, modification of the basement membrane ionic permeabilities was not very effective in reducing the ratio of net solute to solvent flux, and isosmotic transport could not be achieved only by changing ω_{Na}^δ and ω_{Cl}^δ.

Fig. 9 illustrates the effect of variations in the area assumed to be available for transport across the capillary endothelium. Curve 1 *a* indicates that for the compartment model, increased values of r_c lead to a moderately increased solute to solvent flux ratio. The effect is not nearly as large as that predicted by the continuous model (curve 1). The sensitivity to r_c depends on the choice of ω^{δ}_{Na}, the diffusion coefficient at the mouth of the interspace. In the compartment model this parameter was estimated as the Na permeability of the basement membrane whereas for the continuous model no characteristics of the tubular basement membrane were considered.

As shown in Table X small values of r_c lead to an accumulation of salt in the peritubular space adjacent to the basal end of the interspace, indicated by $C^{(4\delta)}_{Na}$. This is analogous to the prediction of the continuous model that the peritubular space concentration exceeds the interspace concentration because of a positive slope, $(dC/dx)_L$, (Fig. 9, dashed line). Although the value of $C^{(4\delta)}_{Na}$ is larger than the interspace concentration, $C^{(3)}_{Na}$, the emergent concentration is less than $C^{(3)}_{Na}$ because of diffusion of solute back into the interspace. However, in all cases the low values of $C^{(4\epsilon)}_{Na}$ indicate that the ion concentration of the reabsorbate drops off sharply as fluid advances into the large peritubular space which is in close communication with the capillaries. The last column in Table X indicates that for high values of r_c the peritubular space ion concentrations are below the interspace concentration. Table X illustrates only the low $L_p{}^{\alpha}$ condition. Raising the value of $L_p{}^{\alpha}$ or $L_p{}^{\beta}$ would obviously lower all concentrations in Table X.

Since the colloid osmotic pressure in the peritubular space, $\pi^{(4)}$ was difficult to estimate, a number of possible values of r_π were examined. This is

TABLE X

COMPARTMENT MODEL: EFFECT OF VARIATIONS IN r_c: THE RATIO OF CAPILLARY AREA AVAILABLE FOR SALT AND WATER FLOW TO THE HISTOLOGICAL CAPILLARY SURFACE AREA

	r_c			
	2.0×10^{-4}	5.0×10^{-4}	1.0×10^{-3} (Std)	2.0×10^{-3}
Emergent concentration				
C_{emerg} *mM*	116.6	117.1	117.8	118.6
Peritubular space concentrations*				
$C^{(4\delta)}_{Na} = C^{(4\delta)}_{Cl}$ *meq/liter*	129.0	125.2	120.6	115.2
$C^{(4\epsilon)}_{Na} = C^{(4\epsilon)}_{Cl}$ *meq/liter*	100.9	100.4	100.2	100.0

The independent parameters are given in Table IV. Interspace concentration required to account for control transepithelial volume flux: $C^{(3)}_{Na} = C^{(3)}_{Cl} = 118.1$ meq/liter with $L_p{}^{\alpha} = 6.10 \times 10^{-6}$ cm s^{-1} $(cmH_2O)^{-1}$.

For Table X, ω^{ϵ}_{Na} and ω^{ϵ}_{Cl} are dependent parameters $= (D \cdot r_c)/(|\Delta x| \cdot RT)$.

* Calculated under conditions of peritubular space solute dispersion ($A^{\epsilon} = 1$ cm^2/cm^2 epithelium).

illustrated in Table XI where $\pi^{(5)}$ is known during both control and saline diuresis (see Appendix D). Under the assumptions of Appendix E the model gives some information about the hydrostatic pressures, $p^{(3)}$ and $p^{(4)}$ during volume expansion (Table XI). The hydraulic conductances $L_p{}^{\delta}$ and $L_p{}^{\epsilon}$ are also functions of r_π . The dependent parameters not shown in Table XI are unaffected by assumptions about r_π .

TABLE XI

COMPARTMENT MODEL: EFFECT OF VARIATIONS IN $r_\pi = \pi^{(4)}/\pi^{(5)}$ ON THE DEPENDENT PARAMETERS

r_π	0.26		0.43 (Std)		0.60		0.77	
	Control	VE	Control	VE	Control	VE	Control	VE
$\pi^{(4)}$ cmH_2O	2.4	0.9	4.0	1.5	5.6	2.1	7.2	2.7
$p^{(4)}$ cmH_2O	2.2	4.6	2.2	4.3	2.2	4.0	2.2	3.8
$p^{(3)}$ cmH_2O	2.2	5.0	2.2	5.0	2.2	5.0	2.2	5.0
$L_p{}^{\delta}$, 10^{-5} $cm\ s^{-1}$ $(cmH_2O)^{-1}$	17.0	17.0	10.0	10.0	7.3	7.3	5.7	5.7
$L_p{}^{\epsilon}$, 10^{-5} $cm\ s^{-1}$ $(cmH_2O)^{-1}$ (No PT space solute dispersion)	6.0	6.0	7.7	7.7	11.0	11.0	19.1	19.1
$L_p{}^{\epsilon}$, 10^{-7} $cm\ s^{-1}$ $(cmH_2O)^{-1}$ (PT space solute dispersion)	2.4	2.4	3.1	3.1	4.4	4.4	7.7	7.7

Table XI lists only those dependent parameters which are affected by variations in r_π.
The independent parameters are the same as in Table IV.
The results in this table are the same for both high and low values of $L_p{}^{\alpha}$.
The following assumptions were used: r_π (control) = r_π (VE) and $p^{(3)}$ (control) = $p^{(4)}$ (control) = $p^{(5)}$ (control) where VE denotes volume expansion.

DISCUSSION

A minimum of four criteria should be fulfilled by any model describing salt and water transport across the proximal tubular epithelium. *First*, the model should explain the net passive transfer of water between two bulk solutions of equal osmolality (luminal fluid and peritubular capillaries). *Second*, it should apply to a particular epithelium. Namely, the model should be compatible with the known cellular and interspace geometry, the known transport coefficients of the intraepithelial barriers, and all information regarding the magnitude and distribution of solute pumps as well as hydrostatic and electrochemical driving forces. *Third*, the model should predict (or be designed to predict) a volume flow equal to what is experimentally observed for that epithelium. *Fourth*, the ratio of solute to volume flow predicted by the model should be approximately isosmotic to capillary plasma.

The three-compartment model, first proposed by Curran (9, 10, 30), involves membranes of different permeabilities together with a hypertonic

middle compartment which, in the case of the proximal tubule, would correspond to the intercellular space. Although this model system predicts a net passive transport of water between two solutions of equal osmolarity, it is not designed to predict either the magnitude of volume transfer or the transport coefficients for a particular epithelium. In addition, the model does not offer a detailed explanation of how salt and water could be transported in an isotonic ratio. A subsequent treatment by Patlak et al. (33) derives an expression for the ratio of net solute to solvent flux in a series membrane system. However, this differs from the present analysis which considers both parallel and series pathways for solute and water flux into the interspace.

Diamond and Bossert's model (13) also proposes that the intercellular spaces function as the hypertonic middle compartment necessary for passive transport of water across the epithelium. However, their model is a general treatment which neither relies heavily on transport parameters from one epithelium nor matches reabsorptive rates to a particular epithelium.

In order to better fulfill the previous four criteria, two alternative models were developed for the *Necturus* proximal tubule preparation. The first model (continuous model) describes the interspace salt concentration as a function of distance. It is similar to Diamond and Bossert's model except that the solute pumps are evenly distributed along the lateral cell membrane and the tight junction is permeable to salt and water. The concentration profiles predicted by the continuous model are fairly uniform along the interspace with the basal end salt concentration always larger than C_o. Hence, the term "standing gradient" is inappropriate because no appreciable concentration gradients exist along the interspace if the pumps are uniformly distributed. The second model (compartment model) is an expansion of the Curran model to five uniform compartments in a series-parallel arrangement.

Certain important features are common to the two proposed models. They both explain the movement of water across a composite epithelial membrane separating solutions of equal osmolarity. They also both rely on values of parameters obtained from the *Necturus* proximal tubule. Parameter values which were not reliably known were varied over a range of experimentally reasonable values. Each model deals with the effects of parameter variations and particularly the effect on emergent concentration. Furthermore, the models are designed to produce the observed fluid reabsorption for this preparation. Saline diuresis is simulated by modifications in the input parameters.

With regard to the fourth criterion neither the continuous model nor the compartment model predict a completely isosmotic reabsorbate. Furthermore, the L_p values of the tight junction (α) and lateral cell membrane (β) seem to be the main determinants of the net solute to solvent flux ratio (as well as the interspace concentration). Values of L_p^{α} and L_p^{β} at the extreme

upper end of the observed range lead to emergent concentrations (solute to solvent flux ratios) which are practically isosmotic to capillary plasma. However, values closer to the lower end of the observed range predict solute to solvent ratios which could be experimentally distinguished from isotonic transport (see Figs. 5, 6). Hence direct measurements of both L_p^{α} and L_p^{β} are crucial for models of epithelial transport.

The only remaining parameters that substantially affect the ratio of solute to solvent flux are the solute permeability and reflection coefficient of the basement membrane. The equations of the compartment model (Appendix E) predict that a decrease in ionic permeability ω_{Na}^{δ} (or ω_{Cl}^{δ}) and a reflection coefficient, σ_{Na}^{δ} (or σ_{Cl}^{δ}), greater than zero might both act to reduce the predicted hypertonicity of the reabsorbate. However, the salt reflection coefficient of the basement membrane is the only parameter variation (in the physiological range) which can produce isotonic (or even hypotonic) net reabsorption in these types of models (Table IX).

Since neither the continuous nor the compartment model consider transport across the basal side of the cell it is possible that ion and water fluxes across this barrier might affect the net solute to solvent flux ratio. Water could be drawn out of the cell by a hypertonic salt concentration in the basal labyrinth. However, if the tubular basement membrane reflection coefficient for NaCl is close to 0, salt and water originating from a hypertonic labyrinth would always cross the basement membrane in a hypertonic ratio. Alternatively, peritubular colloid present in the basal labyrinth could draw water across the basal side of the cell. This possibility is suggested by the nonzero permeability of the tubular basement membrane to albumin (44). In any case, the basal labyrinth salt concentration would still be either isosmolar or hyperosmolar to the cell. If it were hypoosmolar to any extent, the effective osmotic driving force for water to move back into the cell would probably exceed any colloid osmotic force for water to move out of the cell (σ_s of the cell membrane is close to 1.0). Hence any colloid-induced water flux across the basal side of the cell would cross the basement membrane with a salt concentration that is at best only slightly hypoosmotic to the cell. This colloid-induced water flux arising from the basal cell membrane would add to the volume flow arising from the hypertonic interspace. As a result, a model which includes both basal membrane volume flux as well as interspace fluxes might lower the hypertonicity of the reabsorbate but would not predict it to be always exactly isotonic.

If net transport results from a combination of basal cell fluxes and interspace fluxes, variations in one pathway should affect the tonicity of reabsorbate. For example, a colloid-free peritubular fluid or bath should increase the hypertonicity of net transport whereas an inhibited interspace flux should decrease it.

With respect to the second criterion, most of the predicted parameters are in good agreement with the experimental values for *Necturus* proximal tubule in particular, or for epithelia in general. However, some predicted transport coefficients appear inconsistent with experimental data. In addition, no attempt was made to match predicted hydrostatic pressures with experimental values.

The two ionic permeabilities: ω^{β}_{Cl} and ω^{γ}_{Na} (see Table V) are an order of magnitude larger than values measured by Whittembury et al. (52). Since the experiments of Whittembury et al. could not distinguish between the luminal (γ) and lateral (β) cell membranes it is most likely that: $\omega^{\gamma}_{Na} \simeq \omega^{\beta}_{Na} \simeq P^{cell}_{Na}/RT$ and $\omega^{\gamma}_{Cl} \simeq \omega^{\beta}_{Cl} \simeq P^{cell}_{Cl}/RT$ where P^{cell}_{Na} and P^{cell}_{Cl} are from (52). Using these values and the data in Appendix D it is possible to calculate the minimum ionic fluxes across the luminal and lateral cell membranes:[4]

$$\Phi^{\beta}_{Na} = \Phi^{\gamma}_{Na} \geq 3.26 \times 10^{-6} \text{ mmol s}^{-1}/\text{cm}^2 \text{ epithelium},$$

$$\Phi^{\gamma}_{Cl} = \Phi^{\beta}_{Cl} \geq 1.97 \times 10^{-6} \text{ mmol s}^{-1}/\text{cm}^2 \text{ epithelium}.$$

These should be compared with the transepithelial volume flux under control conditions, $\Phi^{te}_{v} = 1.64 \times 10^{-6}$ cm^{3}s^{-1}/cm^2 epithelium. Hence, unless 95% of this Na and Cl flux leaked back into the lumen across the tight junction, the predicted reabsorbate would be unreasonably hypertonic; i.e., $\Phi_{Na}/\Phi^{te}_{v} \geq$ 1,987 mM and $\Phi_{Cl}/\Phi^{te}_{v} \geq$ 1,200 mM. We can only explain the data of Whittembury et al. (52) by postulating significantly different ion permeabilities for the luminal and lateral cell membranes ($\omega^{\gamma} \neq \omega^{\beta}$). In addition, it is possible that the uptake experiments of Whittembury et al. (52) overestimated the cell membrane permeabilities because of the presence of inward directed ion pumps. These pumps might possibly be located at the luminal membrane.

Neither model includes intraepithelial hydrostatic pressure as a driving force under control conditions. In the continuous model, forces driving water from interspace to peritubular space were not specified. The model requires only that the reabsorbate equals the total net volume flow entering the interspace. Hence, it is possible that hydrostatic pressures are partly responsible for this balance. One can estimate the maximum hydrostatic pressure gradient from interspace to peritubular space by adding the approximate pressure drops (*a*) between apical and basal ends of the interspace and (*b*) across the tubular basement membrane.

[4] This calculation of ionic fluxes is based on Eqs. 10 *e* and 9 *e* of Appendix E, where $\Phi_j{}^k = J_j{}^k \cdot A^k$ and the solvent drag terms are negligible because σ^{γ} and σ^{β} are both $\simeq$1.0. The following estimates were used for the concentration terms $C^{(1)}_{Na} - C^{(2)}_{Na} \geq 60$ mM; $C^{(1)}_{Na} + C^{(2)}_{Na} \geq 120$ mM; $C^{(2)}_{Cl}$, $- C^{(3)}_{Cl} \geq -80$ mM; $C^{(2)}_{Cl} + C^{(3)}_{Cl} \geq 120$ mM. Note that $F\Delta\Psi^{\gamma} = 5.39 \times 10^4$ cm^3 mmol^{-1} cm H_2O, and $F\Delta\Psi^{\beta} = -6.91 \times 10^4$ cm^3 mmol^{-1} cm H_2O.

Assuming the interspace to be a rectangular slit, the maximal pressure drop between the two ends of the interspace can be estimated to be <5 cm H_2O.[5] The pressure drop across the basement membrane can be estimated from the hydraulic conductivity of rabbit tubule basement membranes. Assuming a zero colloid osmotic pressure across the basement membrane (*bm*),

$$\Delta P = \Phi_v^{te}/(A^{\delta} \cdot L_p^{bm}) = 4.7 \text{ cm } H_2O,$$

where $L_p^{bm} = 8.8 \times 10^{-5}$ cm s^{-1} (cm $H_2O)^{-1}$ is the value obtained from the hydrostatic pressure measurements in (44). Hence, the overall pressure gradient from interspace to peritubular space is at most 9.7 cm H_2O.

Based on compliance measurements of tubular cell membranes, Grantham has suggested that the observed deformations of the lateral membrane indicate an interspace pressure of 10 cm H_2O (22). However, this calculation assumes that the lateral cell membranes are pinned at both the apical and basal ends. If the basal end of the interspace is free to widen by only 0.5 μm, the calculated interspace pressures would be much lower than 10 cm H_2O. Although interspace pressures could be as high as 10 cm H_2O, hydrostatic gradients would only be important across barriers where osmotic gradients are small. As shown in Appendix A, osmotic pressures are the dominant driving forces across the tight junction and lateral cell membranes. In any event, a different driving force for convective flow across the basement membrane would not affect the main conclusions of this analysis because net volume flux is always constrained to equal the experimentally observed value. Only the estimates of L_p^{δ} and L_p^{ϵ} would be affected.

The continuous and compartment models as well as all previously published models of salt and water transport through cellular interspaces are based on one-dimensional transport equations, with the exception of work by Weinbaum and Goldgraben (43, 20). Consequently, it is not possible to precisely describe the concentration profiles in the peritubular region beyond the end of the interspace. However, several approximations were used to estimate peritubular space concentrations. For the continuous model, the peritubular profiles were estimated by considering the analogous problem of heat conduction in a stream of fluid (26, 53). As illustrated in Fig. 4, hypertonic fluid emerging from the interspace becomes progressively more dilute as it mixes with the bulk of peritubular fluid which is in close communication with the capillary network. This reduction in concentration does not mean that transport becomes more isotonic as fluid moves into the peritubular space. The ratio of solute to solvent flux is set when fluid leaves the interspace

[5] $\Delta P_{max} = (12\eta \cdot L \cdot \Phi_v^{te})/(A^{\delta} \cdot W_i^2) = 5$ cm H_2O which was modified from Eq. 5 (4). The parameter values used in the calculation are given in Appendix D and the viscosity, η was taken as 0.01 poise.

and is invariant after this point. Hence the tonicity of reabsorbate does not depend on whether a one- or two-dimensional analysis is used for the peritubular space. Consequently, the solute to solvent flux ratios for the continuous model were calculated by representing the two-dimensional peritubular space profiles by an equivalent one-dimensional band of hypertonic fluid extending from the mouth of the interspace to the capillary.

In the compartment model, information about the peritubular space concentration profiles was obtained by evaluating, first, the high peritubular space ion concentrations immediately adjacent to the basement membrane, $C_i^{(4\delta)}$, and second, the lower peritubular space ion concentrations adjacent to the capillary endothelium $C_i^{(4\epsilon)}$ where i refers to either Na^+ or Cl^- (see Fig. 10 B). It should be noted that the two-dimensional solute dispersion in the peritubular space does not lead to a drop in the solute to solvent flux ratio.

Although both the continuous and compartment models were developed to explain tubular reabsorption in the intact animal, they can apply to the isolated tubule preparation as well. Fluid would still be hypertonic along the entire length of the interspace and even just outside the interspace up to the basement membrane. However, the main concentration drop would probably occur in an unstirred layer just outside the basement membrane. For the continuous model the peritubular space concentration profiles of Fig. 4 would be greatly compressed in the x direction. The compartment model would still predict the existence of a small region (4δ) of hypertonic fluid located just outside the basement membrane with a Na^+ concentration, $C_{Na}^{(4\delta)}$ (see Fig. 10 B). As with the intact animal, the ratio of net solute to solvent flux is determined by the composition of the fluid reaching the basement membrane.

CONCLUSIONS

The two models developed in this paper, and applied to the *Necturus* proximal tubule, expand on the theories originally proposed by Curran et al., Diamond and Bossert (9, 10, 30, 13). The main original assumptions underlying both the continuous model and the compartment model are, first, the permeability of the tight junction to ions and water, and second, the uniform distribution of solute pumps along the lateral cell membrane. Two general predictions follow from these assumptions: (*a*) The salt concentration profiles are practically uniform with no standing gradients as in Diamond and Bossert's model (13). This allows the lateral interspace to be approximated as a single compartment with a uniform salt concentration. (*b*) Osmotic equilibration is not achieved by the time fluid reaches the end of the interspace. Consequently, the predicted ratios of net solute to solvent flux are always hypertonic to some degree. The extent of this hypertonicity depends on the exact values of the transport parameters. In addition, both the continuous and compartment models are

useful in predicting values of certain transport parameters as well as suggesting an intraepithelial mechanism for volume expansion.

A definitive verification of either our proposed models or the model of Diamond and Bossert (13) requires direct experimental information about the interspace concentration profiles. Micropuncture samples obtained from insect rectal pads (41) indicate hyperosmotic spaces between the cells. However, standing gradients have never been detected in a cellular interspace. Until the existence of these gradients is actually demonstrated we feel it is more appropriate to refer to these models as simply "*hypertonic interspace models.*" Final resolution of this issue must await the development of techniques to determine solute concentrations at two points within the interspace.

A more testable prediction of both the continuous and compartment models is that net reabsorption is not exactly isotonic. Since the hypertonicity is very slight, a large number of measurements would have to be performed in order to detect a significant deviation from isotonicity. Supporting this point is a reanalysis by Whittembury of some earlier data which suggests that fluid reabsorption in the kidney may be slightly hyperosomotic (48). Powell and Malawer (34) have also obtained evidence that net transport in the rat ileum is hypertonic, and experiments by Wheeler (46) suggest a slightly hypertonic net transport in the rabbit gallbladder.

A number of indirect methods exist for testing both the continuous and compartment models. If the hydraulic conductivities of the tight junction and lateral cell membrane are as low as some experiments would indicate (51, 48), the ratio of net solute to solvent flux should be measurably different from isotonic reabsorption (column 1, Tables II and V). However, as indicated in Fig. 6, a cell membrane hydraulic conductivity ($L_p{}^{\beta}$) one order of magnitude larger than that obtained by Whittembury et al. (51, 48) would produce a ratio of solute to solvent flux close to isotonic.

In addition, a tight junction hydraulic conductivity ($L_p{}^{\alpha}$) close to 2.6×10^{-4} cm s^{-1} (cm $H_2O)^{-1}$ would lead to a net reabsorbate that could easily be mistaken for isotonic. High values of $L_p{}^{\alpha}$ are associated with sizable volume fluxes across the tight junction. Solutes like sucrose that cross the *Necturus* proximal tubule via the paracellular pathway (5) would be swept away from the apical end of the interspace if the volume flux through the tight junction were large enough. Such solute entrainment was postulated in order to explain the observed sucrose flows during net volume flux (5).

Direct measurement of ionic transport coefficients also provides a way of testing the models. As mentioned earlier, both the ionic permeabilities and the ionic reflection coefficients of the basement membrane are important determinants of the net solute to solvent flux ratio. In particular a small but nonzero value of the reflection coefficient would considerably reduce the hypertonicity of the net solute to solvent flux (Table IX). As indicated by the

compartment model, both luminal and lateral cell membrane passive ion permeabilities should also be reexamined since the cell potential difference in the proximal tubule leads to unreasonably large Na^+ and Cl^- fluxes if the ionic permeability measurements of Whittembury et al. (52) are used.

In summary, we have developed two associated models for salt and water transport across the proximal tubular epithelium of the *Necturus* which might also be applicable to other leaky epithelia such as the gallbladder or small intestine. Although the proposed models have features in common with previous theories (9, 10, 30, 33, 13), they represent a significant departure from both Curran's compartmental and Diamond and Bossert's standing gradient model. By rejecting the assumption of a localized solute input, the proposed models predict a slightly hypertonic net transport, except if the salt reflection coefficient at the basement membrane or subsequent barriers is greater than zero. The expected deviation from exact isotonicity depends on the precise transport coefficients of the epithelium.

APPENDIX A

Effect of a Leaky Tight Junction on the Concentration Profile at $x = 0$

It can be shown that a permeable tight junction produces a negative slope, dC/dx, at $x = 0$ only if there is a net backflux of water across the tight junction from interspace to lumen. In Appendix C an expression is derived for the slope of the concentration profile at the apical end of the interspace (Eq. 6 *c*):

$$\left.\frac{dC}{dx}\right|_0 = \left[v(0)\cdot C(0) - \frac{W_t}{W_i}\cdot J_s(0)\right] \Big/ D, \qquad (1\ a)$$

where the solute flux across the tight junction is

$$J_s(0) = (1/2)[C_o + C(0)](1 - \sigma_s^{\alpha})J_v(0) + 2\omega_s^{\alpha}\cdot RT[C_o - C(0)], \qquad (2\ a)$$

and

$$v(0) = \frac{W_t}{W_i}\cdot J_v(0). \qquad (3\ a)$$

Combining Eqs. 1 *a*, 2 *a*, and 3 *a*:

$$\left.\frac{dC}{dx}\right|_0 = \frac{1}{2D}\cdot\frac{W_t}{W_i}\cdot J_v(0)[[C(0) - C_o] + \sigma_s^{\alpha}\cdot[C(0) + C_o]] + \frac{1}{D}\cdot\frac{W_t}{W_i}\cdot 2\omega_s^{\alpha}\cdot RT[C(0) - C_o].$$

For $C(0) > C_o$, $(dC/dx)_{x=0}$ is <0 only if $J_v(0) < 0$.

Assuming an interspace hypertonicity (ΔC) of only 1 mM NaCl, a backflux of

water would only occur if the hydrostatic pressure gradient from interspace to lumen exceeded $\sigma_s{}^{\alpha}RT\Delta C$. For $\sigma_s{}^{\alpha} = 0.7$ and $\Delta C = 1$ mM NaCl, $\sigma_s{}^{\alpha}RT\Delta C = 18.3$ and 17.5 cm H_2O for mammalian and amphibian tubules, respectively. This is more than 3 times the highest observed transtubular pressure gradients in the rat (14) and one to two orders of magnitude larger than the control transtubular pressure gradient in the *Necturus* (21). Hence, the osmotic gradient exceeds the hydrostatic pressure gradient across the tight junction and $J_v(0) > 0$ which implies that $(dC/dx)_{x=0} > 0$.

APPENDIX B

General Shape of Interspace Concentration Profiles Assuming a Uniform Solute Input

This appendix reexamines the three first-order differential equations of Diamond and Bossert's model (13):

$$\frac{dv}{dx} = \frac{2P}{r}[C(x) - C_o], \tag{1 b}$$

r and P are, respectively, the radius and water permeability of Diamond and Bossert's channel.

$$\frac{dC}{dx} = B, \tag{2 b}$$

$$\frac{dB}{dx} = \left[C \cdot \frac{dv}{dx} + v \cdot B - \frac{2N(x)}{r}\right] \Big/ D. \tag{3 b}$$

$N(x)$ is the rate of active solute transport across the walls of the channel. If the active solute pumps are distributed uniformly along the length of the interspace, $N(x) = N$, a constant.

Writing each of the three derivatives as forward differences:

$$\frac{dv}{dx} = \frac{v(x_{i+1}) - v(x_i)}{\Delta x}, \tag{4 b}$$

$$\frac{dC}{dx} = \frac{C(x_{i+1}) - C(x_i)}{\Delta x}, \tag{5 b}$$

$$\frac{dB}{dx} = \frac{B(x_{i+1}) - B(x_i)}{\Delta x}, \tag{6 b}$$

where Δx is the constant difference: $x_{i+1} - x_i$.
Rewriting Eqs. 1 *b*, 2 *b*, and 3 *b* as finite difference equations:

$$v(x_{i+1}) = v(x_i) + \frac{2P}{r}[C(x_i) - C_o] \cdot \Delta x, \tag{7 b}$$

$$C(x_{i+1}) = C(x_i) + B(x_i) \cdot \Delta x, \tag{8 b}$$

$$B(x_{i+1}) = B(x_i) + \left.\frac{dB}{dx}\right|_{x_i} \cdot \Delta x, \tag{9 b}$$

and

$$\left.\frac{dB}{dx}\right|_{x_i} = \frac{2P}{rD} C(x_i)[C(x_i) - C_o] + \frac{v(x_i)\cdot B(x_i)}{D} - \frac{2N}{rD}, \qquad (10\ b)$$

where Eq. 1 *b* was used to evaluate dv/dx.

Let x_p be the first point in the open interval $(0, L)$ where dC/dx and d^2C/dx^2 are both <0. Therefore, $B(x_p) < 0$ and $(dB/dx)_{x_p} < 0$.
Let $x_i = x_p$, then Eqs. 7 *b*, 8 *b*, and 9 *b* imply, respectively:

$$v(x_{p+1}) = v(x_p) + \frac{2P}{r}[C(x_p) - C_o]\cdot\Delta x > v(x_p) > 0, \qquad (11\ b)$$

since $C(x_p) > C_o$.

$$C(x_{p+1}) = C(x_p) + B(x_p)\cdot\Delta x < C(x_p), \qquad (12\ b)$$

$$B(x_{p+1}) = B(x_p) + \left.\frac{dB}{dx}\right|_{x_p} \cdot \Delta x < B(x_p) < 0. \qquad (13\ b)$$

From 13 *b* and $v(x_{p+1}) > 0$ it follows that:

$$v(x_{p+1})B(x_{p+1}) < v(x_{p+1})B(x_p). \qquad (14\ b)$$

From Eq. 11 *b* and $B(x_p) < 0$ it follows that:

$$v(x_{p+1})B(x_p) < v(x_p)B(x_p). \qquad (15\ b)$$

Combining Eqs. 14 *b* and 15 *b*:

$$v(x_{p+1})B(x_{p+1}) < v(x_p)B(x_p). \qquad (16\ b)$$

From Eq. 12 *b* it follows that:

$$C(x_{p+1})[C(x_{p+1}) - C_o] < C(x_p)[C(x_p) - C_o]. \qquad (17\ b)$$

Eq. 10 *b* and the inequalities in Eqs. 16 *b* and 17 *b* require that:

$$\begin{aligned}\left.\frac{dB}{dx}\right|_{x_{p+1}} &= \frac{2P}{rD} C(x_{p+1})[C(x_{p+1}) - C_o] + \frac{v(x_{p+1})B(x_{p+1})}{D} - \frac{2N}{rD} \\ &< \frac{2P}{rD} C(x_p)[C(x_p) - C_o] + \frac{v(x_p)B(x_p)}{D} - \frac{2N}{rD} = \left.\frac{dB}{dx}\right|_{x_p} < 0.\end{aligned} \qquad (18\ b)$$

Hence, if $B(x_p)$ and $(dB/dx)_{x_p}$ are both <0, then $B(x_{p+1})$ and $(dB/dx)_{x_{p+1}}$ must both be <0. Continuing this process, $B(x_{p+2})$ and $(dB/dx)_{x_{p+2}}$ will also be <0, etc. Therefore, by induction it follows that dC/dx and d^2C/dx^2 are both <0 for all x in the region $[x_p, L^-]$.

APPENDIX C

Equations for the Continuous Interspace Model

The basic geometry of the continuous model is illustrated in Fig. 1 C. The intercellular channel is represented as a rectangular space of length L. The use of rectangular

rather than cylindrical geometry does not alter Diamond and Bossert's (13) basic one-dimensional equations except that the cylindrical cross section πr^2 is replaced by $W_i \cdot l$ and the cylindrical surface area $2\pi r \cdot \Delta x$ by $2 \cdot l \cdot \Delta x$. All symbols used are defined in the glossary. The superscripts "+" and "−" denote, respectively, the right- and left-sided limits about a point.

The tight junction is represented as an effective barrier immediately adjacent to the start of the interspace at $x = 0$. Eqs. 1 *c* and 2 *c* give the volume and salt flow across the tight junction effective barrier under conditions of no net current (23).

$$J_v(0) = L_p{}^{\alpha}[\Delta p^{\alpha} - 2\sigma_s{}^{\alpha} \cdot RT \cdot (C_o - C(0))], \tag{1 c}$$

$$J_s(0) = (\tfrac{1}{2})[C_o + C(0)](1 - \sigma_s{}^{\alpha})J_v(0) + 2\omega_s{}^{\alpha} \cdot RT \cdot [C_o - C(0)], \tag{2 c}$$

C_o is the luminal salt concentration and $C(0)$ is the salt concentration at the most apical end of the interspace, $x = 0$. The interspace volume and salt flow at $x = 0$ must equal the volume and salt flow crossing the effective tight junction barrier, i.e.,

$$W_i \cdot v(0) = W_t \cdot J_v(0), \tag{3 c}$$

and,

$$W_i \cdot \left[v(0) \cdot C(0) - D \cdot \frac{dC}{dx}\bigg|_0 \right] = W_t \cdot J_s(0). \tag{4 c}$$

Rearranging Eqs. 3 *c* and 4 *c*, the boundary conditions at $x = 0$ are:

$$v(0) = \frac{W_t}{W_i} \cdot J_v(0), \tag{5 c}$$

$$\frac{dC}{dx}\bigg|_0 = \left[v(0) \cdot C(0) - \frac{W_t}{W_i} \cdot J_s(0) \right] \Big/ D, \tag{6 c}$$

where $J_v(0)$ and $J_s(0)$ are given by Eqs. 1 *c* and 2 *c*.

The differential equations for solvent and solute flow along the interspace are similar to those of Diamond and Bossert (13).

$$\frac{dv}{dx} - \frac{4}{W_i} \cdot \sigma_s{}^{\beta} \cdot L_p{}^{\beta} \cdot RT \cdot [C(x) - C_c] = 0, \tag{7 c}$$

$$v \cdot \frac{dC}{dx} + C \cdot \frac{dv}{dx} - D \cdot \frac{d^2C}{dx^2} - \frac{2}{W_i} \cdot J_s{}^{\beta} = 0, \tag{8 c}$$

where

$$J_s{}^{\beta} = L_p{}^{\beta} \cdot \sigma_s{}^{\beta} \cdot (1 - \sigma_s{}^{\beta})[C^2(x) - C_c{}^2]RT + 2\omega_s{}^{\beta} \cdot RT \cdot [C_c - C(x)] + {}_{act}J_s{}^{\beta},$$

which is modified from the Kedem-Katchalsky relations (23) for zero net current and a cell salt concentration $= C_c$.

For a one-dimensional analysis no attempt was made to calculate the lateral dispersion of solute which would undoubtably occur when hypertonic fluid from the

interspace enters a peritubular region which is relatively isotonic (compare Figs. 3 and 4). Hence the peritubular space salt concentrations for the one-dimensional analysis were calculated for a narrow rectangular band of peritubular fluid with width W_i and length $[L, M]$ (shaded region in Fig. 3 B) which does not interact with the rest of the peritubular space. The flux of solvent and solute leaving the interspace at $x = L$ is:

$$\Phi_v(L) = v(L^-) \cdot A(L), \tag{9 c}$$

$$\Phi_s(L) = \left[-D \cdot \frac{dC}{dx}\bigg|_{L^-} + C(L^-) \cdot v(L^-) \right] \cdot A(L), \tag{10 c}$$

so that the ratio of solute to solvent flux or "emergent concentration" is given by,

$$C_{\text{emerg}} = \frac{\Phi_s(L)}{\Phi_v(L)} = C(L^-) - \frac{D}{v(L^-)} \frac{dC}{dx}\bigg|_{L^-}. \tag{11 c}$$

Since in a one-dimensional analysis there is no change in cross-sectional area at the transition between interspace and peritubular space [$A(x) = A(L)$ for $L \leq x \leq M^-$], the boundary conditions at $x = L^+$ are:

$$C(L^+) = C(L^-) \text{ continuity of concentration,} \tag{12 c}$$

$$v(L^+) = v(L^-) \text{ continuity of linear velocity,} \tag{13 c}$$

$$-D \cdot \frac{dC}{dx}\bigg|_{L^+} + C(L^+) \cdot v(L^+) = -D \cdot \frac{dC}{dx}\bigg|_{L^-} + C(L^-) \cdot v(L^-) \text{ mass balance on solute.} \tag{14 c}$$

Beyond $x = L$ steady-state solute and volume flow is assumed to occur only in the x direction. The solute differential equation in the region $[L, M]$ becomes:

$$v \cdot \frac{dC}{dx} - D \cdot \frac{d^2C}{dx^2} = \frac{d}{dx}\left[-D \cdot \frac{dC}{dx} + C \cdot v \right] = 0, \tag{15 c}$$

and the linear velocity in $[L, M]$ becomes:

$$v(x) = v(L^+) = v(L^-). \tag{16 c}$$

Consequently,

$$-D \cdot \frac{dC}{dx} + C \cdot v = \text{const} = -D \cdot \frac{dC}{dx}\bigg|_{L^-} + C(L^-) \cdot v(L^-), \tag{17 c}$$

where Eq. 17 c has a well-defined exponential solution in $[L, M]$.

Since the cross-sectional area of the shaded region in Fig. 3 B is unchanged through out the peritubular space, $A(M^-) = A(L)$. Hence, the volume and solute fluxes just outside the capillary wall at $x = M^-$ are:

$$\Phi_v(M^-) = v(M^-) \cdot A(L), \tag{18 c}$$

$$\Phi_s(M^-) = \left[-D \cdot \frac{dC}{dx}\bigg|_{M^-} + C(M^-) \cdot v(M^-) \right] \cdot A(L). \tag{19 c}$$

Eq. 16 *c* at $x = M^-$ requires $v(M^-) = v(L^-)$ or $\Phi_v(M^-) = \Phi_v(L)$. Similarly, Eq. 17 *c* at $x = M^-$ together with Eq. 10 *c* requires,

$$\Phi_s(M^-) = \Phi_s(L). \tag{20 c}$$

In the simplest treatment of the peritubular capillaries, the volume and solute fluxes within the capillary wall are given by:

$$\Phi_v(M^+) = v(M^+) \cdot A(M^+), \tag{21 c}$$

$$\Phi_s(M^+) = \left[-D \cdot \frac{dC}{dx}\bigg|_{M^+} + C(M^+) \cdot v(M^+) \right] \cdot A(M^+). \tag{22 c}$$

Since there is a reduction in cross-sectional area at the capillary wall, $A(M^+) = r_c \cdot A(M^-) = r_c \cdot A(L)$, where r_c is the ratio of capillary area available for salt and water flux to the histological capillary surface area.

The capillary endothelium is approximated as an effective membrane since its thickness, $|\Delta x|$, is much less than the dimensions of the peritubular space. As a result, Eq. 22 *c* can be replaced by an equation for the solute flux across a membrane separating two solutions with concentrations: $C(M)$ and $C(N)$. The solute concentrations are assumed to be continuous at the membrane boundaries, e.g. at $x = M$:

$$C(M^-) = C(M^+) = C(M). \tag{23 c}$$

Therefore,

$$\Phi_s(M^+) = (\tfrac{1}{2})[C(M) + C(N)](1 - \sigma_s^{\epsilon}) \cdot v(M^+) \cdot r_c \cdot A(L) + \frac{D \cdot r_c}{|\Delta x|} [C(M) - C(N)] \cdot A(L). \tag{24 c}$$

The term $(D \cdot r_c)/|\Delta x|$ equals $2RT\omega_s^{\epsilon}$ where ω_s^{ϵ} is the capillary wall solute diffusion coefficient. The capillary solute reflection coefficient, σ_s^{ϵ}, is assumed to be zero. It is unnecessary to rewrite Eq. 21 *c* because $\Phi_v(M^+)$ is always constrained to equal the experimentally observed net volume flux, Φ_v^{te}

The linear flow velocity across the capillary wall, $v(M^+)$ is determined by the mass balance condition on volume flow at $x = M$ and Eqs. 9 *c* and 21 *c*:

$$\Phi_v(M^+) = v(M^+) \cdot r_c \cdot A(L) = \Phi_v(M^-) = v(M^-) \cdot A(M^-) = \Phi_v(L) = v(L^-) \cdot A(L),$$

or

$$r_c \cdot v(M^+) = v(M^-) = v(L^-). \tag{25 c}$$

A self-consistent solution for the concentration profiles was obtained as follows: Conservation of mass at $x = 0$ requires that the initial values of v and dC/dx be functions of $C(0)$, the initial concentration (see Eqs. 5 *c* and 6 *c*). Hence, for a par-

ticular value of $C(0)$ it is possible to generate concentration and velocity profiles along the interspace, $[0, L]$, by numerical integration of Eqs. 7 *c* and 8 *c*. The computed values of $C(L^-)$, $v(L^-)$, and $(dC/dx)_{L^-}$ together with Eqs. 16 *c* and 17 *c* determine the concentration and velocity profiles in the peritubular space, $[L, M]$. In this manner a family of concentration profiles can be generated in the region $[0, M]$, each corresponding to a different initial concentration, $C(0)$.

However, profiles representing a solution to the boundary value problem must satisfy two additional constraints: (*a*) The net volume flux leaving the interspace must equal the mean experimental *Necturus* reabsorptive flux; i.e., $\Phi_v(L) = \Phi_v^{te}$ (see Eq. 9 *c*). (*b*) The net solute flux leaving the mouth of the interspace must equal the solute flux calculated from Eq. 24 *c*; i.e., $\Phi_s(L) = \Phi_s(M^+)$. From Eq. 20 *c*, this condition is equivalent to a mass balance on solute at $x = M$; i.e., $\Phi_s(M^+) = \Phi_s(M^-)$. Note that $\Phi_s(M^+)$ calculated from Eq. 24 *c* is not constrained to equal the experimentally observed solute flux, Φ_s^{te}.

APPENDIX D

Justification of Independent Parameter Values for *Necturus* Proximal Tubule

The Continuous Model

CONSTANT QUANTITIES OBTAINED FROM EXPERIMENTAL DATA

$A^\delta = A(L)$ The cross-sectional area at the mouth of the interspace (basal end) is the product of W_i and l (discussed below). $A^\delta = W_i \cdot l = 5 \times 10^{-6}$ cm $\times$ 800 cm/cm^2 epithelium $= 4 \times 10^{-3}$ cm^2/cm^2 epithelium.

ω_s^α Only an upper bound can be placed on the salt diffusion coefficient for the tight junction, ω_s^α. If all the NaCl flux went through the tight junction, $2\omega_s^\alpha RT = P_s^\alpha = P_s^{te} \cdot (A^{te}/A^\alpha)$. Obviously, all the salt flux does not traverse the tight junction and $\omega_s^\alpha < (\frac{1}{2})(P_s^{te}/RT) \cdot (A^{te}/A^\alpha)$; $P_s^{te} = 3.04 \times 10^{-6}$ cm s^{-1} (7); $RT = 2.53 \times 10^4$ (cm H_2O) cm^3 mmol^{-1} (see below). The areas are defined as follows: $A^{te} = 1$ cm^2/cm^2 epithelium; $A^\alpha = W_t \cdot l = 2 \times 10^{-4}$ cm^2/cm^2 epithelium (W_t and l evaluated below). Hence, $\omega_s^\alpha < 3.0 \times 10^{-7}$ cm s^{-1} mmol cm^{-3} (cm H_2O)$^{-1}$. We arbitrarily chose a value of $\omega_s^\alpha = 1.52 \times 10^{-7}$ cm s^{-1} mmol cm^{-3} (cm H_2O)$^{-1}$ for ω_s^α. During saline diuresis ω_s^α was observed to increase by a factor of 3 (7).

ω_s^β Using cell membrane ion permeabilities obtained from Whittembury et al. (51) (i.e., $P_{Na} = 8.7 \times 10^{-7}$ cm s^{-1} and $P_{Cl} = 5.9 \times 10^{-6}$ cm s^{-1}),

$$\omega_s^\beta = \frac{\omega_{Na}^\beta \cdot \omega_{Cl}^\beta}{\omega_{Na}^\beta + \omega_{Cl}^\beta} = \frac{1}{RT} \frac{P_{Na} \cdot P_{Cl}}{P_{Na} + P_{Cl}} = 3 \times 10^{-11} \text{ cm s}^{-1}\text{mmole cm}^{-3}(\text{cm } H_2O)^{-1}.$$

σ_s^α For the *Necturus* proximal tubule, the reflection coefficient of the tight junction is approximately equal to the reflection coefficient of the epithelium, σ_s^{te}. Hence, $\sigma_s^\alpha = \sigma_s^{te} = 0.7$ from (3).

σ_s^β From the work of Whittembury et al. (52) the *Necturus* cell membrane reflection coefficient was measured as 0.97 on the basis of zero time rate of cell swelling, where the extracellular osmolarity of NaCl leading to no change in cell volume was

not significantly different from sucrose or mannitol where $\sigma = 1$. Hence σ_s^β was approximated as 1.0.

Φ_v^{te} The experimentally observed transepithelial volume fluxes in control conditions and saline diuresis were taken from Boulpaep (7). Φ_v^{te} (control) = 1.64×10^{-6} cm^3 s^{-1}/cm^2 epithelium, Φ_v^{te} (VE) = 0.91×10^{-6} cm^3 s^{-1}/cm^2 epithelium, where VE denotes volume expansion.

Φ_s^{te} The experimentally observed salt fluxes were also taken from (7): Φ_s^{te} (control) = 1.64×10^{-7} mmol s^{-1}/cm^2 epithelium, Φ_s^{te} (VE) = 0.91×10^{-7} mmol s^{-1}/cm^2 epithelium.

Δp^α Under control conditions, the average hydrostatic pressure difference between lumen and peritubular capillaries is 0.26 cm H_2O (21). It is doubtful that interspace hydrostatic pressure greatly exceeds luminal or peritubular hydrostatic pressure. Therefore, the pressure gradient across the tight junction, Δp^α, was chosen as 0.2 cm H_2O.

l Since there are 1.6×10^5 cells/cm^2 epithelium (8), the total linear length of cellular circumference is calculated to be $l = 800$ cm/cm^2 epithelium.

W_t The width of the tight junction, W_t, was taken as 25×10^{-8} cm which is the average of values from (4) and (5).

W_i The width of the interspace, W_i, was taken as 5×10^{-6} cm, which is an average of values from (8, 2).

C_o The NaCl concentration of *Necturus* luminal fluid is about 100 mM. For convenience, C_o is taken as exactly 100 mM.

C_c In the continuous model, the cellular NaCl concentration is assumed to be the same as the luminal salt concentration; i.e., $C_c = C_o = 100$ mM.

$C(N)$ Since the capillaries are assumed to be well mixed, the salt concentration at the inside face of the capillary wall, $C(N)$, is equivalent to the capillary salt concentration. The capillary plasma NaCl concentration is approximately identical to the luminal salt concentration. Consequently $C(N)$ was taken equal to C_o.

D The free solution salt diffusion coefficient, D, was taken as 1.48×10^{-5} cm^2 s^{-1} which is applicable for 100 mM solutions of NaCl at 25°C (35).

$|\Delta x|$ The average path length through a typical capillary wall was taken as 1×10^{-4} cm (32).

RT The value of RT used throughout the analysis was obtained from: T = 25°C = 298°K; $R = 8.31$ J mol^{-1} (°K)$^{-1}$ from (42); 1 J = 9.896×10^{-3} liter-atm; 1 atm = 760 mm Hg = 76 cm Hg; 1 cm Hg = 13.6 cm H_2O; $RT = 2.53 \times 10^4$ (cm H_2O) cm^3 mmol^{-1}.

QUANTITIES VARIED OVER A RANGE OF EXPERIMENTALLY OBSERVED VALUES

L_p^α The simplest approximation for estimating the L_p of the tight junction is to assume that salt and water flux from lumen to interspace occurs either through the cell via membranes γ and β or across the tight junction (barrier α). Let the cellular pathway across γ and β be represented by a single effective barrier with cross-sectional area A^{cell} and filtration coefficient L_p^{cell}. This is in parallel with barrier α of area A^α and filtration coefficient L_p^α.

From Kedem and Katchalsky's analysis of parallel membranes (24) it follows that:

$$L_p^{te} = \frac{A^\alpha}{A^\alpha + A^{cell}} \cdot L_p^\alpha + \frac{A^{cell}}{A^\alpha + A^{cell}} \cdot L_p^{cell}. \qquad (1\,d)$$

The circulation term, $\alpha_a\alpha_{bK}'(\beta_a - \beta_b)^2$, (24), has been omitted because electrical effects were neglected in this calculation.

Since the width of the tight junction is negligible compared with the dimensions of the cell, $A^\alpha + A^{cell} \simeq A^{cell}$. Hence, it follows from Eq. 1 *d* that:

$$L_p^\alpha \simeq \frac{A^{cell}}{A^\alpha}(L_p^{te} - L_p^{cell}). \qquad (2\,d)$$

The effective area, A^{cell}, is probably close to 1 cm^2/cm^2 epithelium. The area of the tight junction barrier, A^α, is given by $W_t \cdot l$. The L_p of the *Necturus* proximal tubule cell membrane was obtained directly from the experiments of Whittembury et al. (51, 48), i.e., $L_p^{cell} = 2.8 \times 10^{-10}$ cm s^{-1} (cm $H_2O)^{-1}$.

Two extreme estimates of L_p^{te} were chosen to represent a range of values. Using an L_p^{te} of 15×10^{-10} cm s^{-1} (cm $H_2O)^{-1}$ from (48), Eq. 2 *d* predicts $L_p^\alpha = 6.1 \times 10^{-6}$ cm s^{-1} (cm $H_2O)^{-1}$. For an L_p^{te} of 520×10^{-10} cm^{-1} (cm $H_2O)^{-1}$ ([21] luminal hydrostatic measurement), the predicted L_p^α is 2.6×10^{-4} cm s^{-1} (cm $H_2O)^{-1}$.

L_p^β The L_p of the *Necturus* proximal tubule cell membrane was obtained directly from the experiments of Whittembury et al. (48, 51) with $L_p^{cell} = 2.8 \times 10^{-10}$ cm s^{-1} (cm $H_2O)^{-1}$. Since this probably represents a minimum value, several L_p^β's spanning an order of magnitude were investigated. The standard L_p^β was taken as 2.8×10^{-10} cm s^{-1} (cm $H_2O)^{-1}$.

L Electron micrographs sectioned perpendicular to the tubule axis indicate that the interspaces of the *Necturus* proximal tubule extend radially outward from the tubular lumen with little convolution. This differs significantly from the interdigitating convoluted interspaces of mammalian tubules.

Furthermore, infoldings of the lateral cell membrane which are occasionally seen in the *Necturus* interspaces seem to be cylindrical "finger-like" projections which would not significantly increase the histological surface area of the lateral cell membranes.

For these reasons, the *Necturus* proximal tubular interspace length, L, was taken equal to the linear cell dimension of 25 μm (8, 2). For completeness, calculations were also done with interspace lengths of 40 and 60 μm.

r_c r_c is the ratio of capillary surface area available for salt and water transport to the histological capillary surface area. A range of values from 0.0002 to 0.002 was chosen around a standard value of 0.001 in accordance with an estimate by Pappenheimer for a ratio of pore area to histological capillary area less than or equal to 0.001 (27).

The Compartment Model

CONSTANT QUANTITIES OBTAINED FROM EXPERIMENTAL DATA

A^α The cross-sectional area of the tight junction barrier is $A^\alpha = W_t \cdot l = 2 \times 10^{-4}$ cm^2/cm^2 epithelium (W_t and l were evaluated above).

A^γ In the mammalian tubule, the infoldings of the brush border increase the

luminal plasma membrane surface area by a factor of 40 (29). From the lower density of infoldings in the *Necturus* brush border the luminal area expansion was estimated to be half that of the mammalian tubule. Hence A^{γ} was taken as 20 cm^2/cm^2 epithelium.

A^{δ} See above.

A^{ϵ} Under conditions where there is no solute dispersion in the peritubular space, $A^{\epsilon} = A^{\delta}$. When solute dispersion is allowed to occur in the peritubular space, $A^{\epsilon} = 1$ cm^2/cm^2 epithelium.

$L_p{}^{\gamma}$ Since measurements of cell membrane L_p's from kidney slices cannot distinguish between the luminal and lateral cell membrane, $L_p{}^{\gamma}$ was taken equal to $L_p{}^{\beta}$. ($L_p{}^{\beta}$ given below.)

ω^{β}_{Na} The sodium diffusion coefficient for the lateral cell membrane is equal to P^{β}_{Na}/RT where the P_{Na} of the *Necturus* kidney cell membrane is 8.7×10^{-7} cm s^{-1} from (52). $\omega^{\beta}_{Na} = 3.44 \times 10^{-11}$ cm s^{-1} meq cm^{-3} (cm H_2O)$^{-1}$.

ω^{γ}_{Cl} The chloride diffusion coefficient for the luminal cell membrane is P^{γ}_{Cl}/RT where P^{γ}_{Cl} was taken from the average P_{Cl} for the *Necturus* kidney cell membrane = 5.9×10^{-6} cm s^{-1} (52). $\omega^{\gamma}_{Cl} = 2.33 \times 10^{-10}$ cm s^{-1} meq cm^{-3} (cm H_2O)$^{-1}$.

$\omega^{\delta}_{Na} = \omega^{\delta}_{Cl}$ Since no information is available about the properties of the *Necturus* proximal tubule basement membrane, ω^{δ}_{Na} is difficult to estimate. Assuming equal permeabilities for Na^+ and Cl^-, an approximate value of ω^{δ}_{Na} can be obtained:

$$\omega^{\delta}_{Na} = 2\omega^{\delta}_{NaCl} = P^{\delta}_{NaCl}/RT = \frac{1}{RT}\frac{D_{NaCl}}{\Delta x}\frac{A_v{}^{\delta}}{A_h{}^{\delta}},$$

where Δx is the thickness of the barrier, $A_v{}^{\delta}$ is the area available for solvent transport across δ and $A_h{}^{\delta}$ is the histological surface area of the δ barrier. It is assumed that the transport area available for Na^+ and Cl^- is not significantly different from the area available for solvent transport. A similar expression applies for the permeability across the capillary endothelium:

$$\omega^{\epsilon}_{Na} = \frac{1}{RT}\frac{D_{NaCl}}{\Delta x}\frac{A_v{}^{\epsilon}}{A_h{}^{\epsilon}}.$$

If the δ barrier represents primarily the properties of the basement membrane, then equal histological areas of basement membrane (*bm*) and capillary endothelium (cap) should have permeability coefficients which are related as follows:

$$\frac{\omega^{\delta}_{Na}}{\omega^{\epsilon}_{Na}} = (A_v/\Delta x)_{bm}/(A_v/\Delta x)_{cap}.$$

The hydraulic conductivities of the basement membrane and capillary can be estimated from basic pore theory:

$$L_p^{bm} = (r^2_{bm}/8\eta)\cdot(A_v/\Delta x)_{bm},$$

$$L_p^{cap} = (r^2_{cap}/8\eta)\cdot(A_v/\Delta x)_{cap},$$

where η denotes viscosity and r_{bm}, r_{cap} denote the average pore radius of the basement

membrane and capillary, respectively. Combining these expressions:

$$\omega^{\delta}_{Na} = \omega^{\epsilon}_{Na} \cdot (L_p^{bm}/L_p^{cap}) \cdot (r_{cap}/r_{bm})^2.$$

Since there is no reliable estimate of r_{cap}/r_{bm}, we assumed that it is approximately 1. On the other hand, the ratio of L_p's can be evaluated from experimental data. The applied pressure measurements of Welling and Grantham yield an $L_p^{bm} = 5.3 \times 10^{-3}$ cm^3/(cm^2 min·cm H_2O) for the rabbit proximal convoluted tubule (44). Anagnostopoulos and Windhager obtained an $L_p^{cap} = 3 \times 10^{-3}$ cm^3/(cm^2 min·cm H_2O) for rat peritubular capillaries (1). From these values: $\omega^{\delta}_{Na} = 1.77\ \omega^{\epsilon}_{Na} = 1.04 \times 10^{-8}$ cm s^{-1} mmol cm^{-3} (cm H_2O)$^{-1}$. (ω^{ϵ}_{Na} is evaluated below.)

$\omega^{\epsilon}_{Na} = \omega^{\epsilon}_{Cl}$ If Na and Cl have approximately equal diffusion coefficients across the capillary endothelium, $\omega^{\epsilon}_{Na} \simeq \omega^{\epsilon}_{Cl}$, then $\omega^{\epsilon}_{NaCl} = (\omega^{\epsilon}_{Na} \cdot \omega^{\epsilon}_{Cl})/(\omega^{\epsilon}_{Na} + \omega^{\epsilon}_{Cl}) = (1/2)\ \omega^{\epsilon}_{Na}$; and, $\omega^{\epsilon}_{Na} = 2\omega^{\epsilon}_{NaCl} = P^{\epsilon}_{NaCl}/RT = (D_{NaCl} \cdot r_c)/(|\Delta x| \cdot RT)$, where $|\Delta x|$ and r_c were defined above. If Na and Cl enter the capillary via pores which are large compared to the dimensions of the ions, $D_{NaCl} \simeq D_{NaCl}$ (free solution) $= 1.48 \times 10^{-5}$ cm^2 s^{-1} (35). Hence, $\omega^{\epsilon}_{Na} = \omega^{\epsilon}_{Cl} = 5.85 \times 10^{-9}$ cm s^{-1} meq cm^{-3} (cm H_2O)$^{-1}$. If r_c is different from 1×10^{-3}, then ω^{ϵ}_{Na} and ω^{ϵ}_{Cl} are *dependent* parameters (see Appendix E).

σ_j^k The following simplifying assumptions were made regarding the reflection coefficients used in the compartment model: (1) $\sigma^{\alpha}_{Na} = \sigma^{\alpha}_{Cl}$; (2) $\sigma^{\beta}_{Na} = \sigma_s{}^{\beta} = 1.0$; (3) $\sigma^{\gamma}_{Na} = \sigma_s{}^{\gamma} = 1.0$; (4) $\sigma^{\epsilon}_{Na} = \sigma_s{}^{\epsilon} = 0$.

The salt reflection coefficients and permeabilities can be expressed as functions of ionic reflection coefficients and permeabilities (25). For the effective tight junction barrier, α:

$$\sigma_s{}^{\alpha} = \omega_s{}^{\alpha} \cdot [(\sigma^{\alpha}_{Na}/\omega^{\alpha}_{Na}) + (\sigma^{\alpha}_{Cl}/\omega^{\alpha}_{Cl})].$$

Since $\sigma^{\alpha}_{Na} = \sigma^{\alpha}_{Cl}$, and $\omega_s{}^{\alpha} = (\omega^{\alpha}_{Na} \cdot \omega^{\alpha}_{Cl})/(\omega^{\alpha}_{Na} + \omega^{\alpha}_{Cl})$

$$\sigma_s{}^{\alpha} = \omega_s{}^{\alpha} \cdot \sigma^{\alpha}_{Na} \cdot [(\omega^{\alpha}_{Na})^{-1} + (\omega^{\alpha}_{Cl})^{-1}] = \sigma^{\alpha}_{Na},$$

so that $\sigma^{\alpha}_{Na} = \sigma^{\alpha}_{Cl} = \sigma_s{}^{\alpha}$ where $\sigma_s{}^{\alpha}$ was taken as 0.7 (see above).

Using a similar analysis it can be shown that assumptions 2, 3, and 4 above lead to the following values for the reflection coefficients: $\sigma^{\beta}_{Na} = \sigma^{\beta}_{Cl} = \sigma_s{}^{\beta} = 1.0$; $\sigma^{\gamma}_{Na} = \sigma^{\gamma}_{Cl} = \sigma_s{}^{\gamma} = 1.0$; $\sigma^{\epsilon}_{Na} = \sigma^{\epsilon}_{Cl} = \sigma_s{}^{\epsilon} = 0$. These equalities suggested the additional assumptions that $\sigma^{\gamma}_{Na} = \sigma^{\gamma}_{cat} = \sigma^{\gamma}_{an}$ and $\sigma^{\beta}_{Na} = \sigma^{\beta}_{cat} = \sigma^{\beta}_{an}$.

Φ_v^{te} See above.

Φ_s^{te} See above.

$C_s{}^{(1)}$ The luminal salt concentration, $C_s{}^{(1)}$, is equal to C_o which was taken as exactly 100 mM (see above). Since only Na and Cl are considered $C_s^{(1)} = C^{(1)}_{Na} = C^{(1)}_{Cl} = C_o$.

$C_s{}^{(5)}$ The capillary salt concentration is also taken as exactly 100 mM (see above value of $C(N)$). $C_s{}^{(5)} = C^{(5)}_{Na} = C^{(5)}_{Cl} = C_o$.

$C^{(2)}_{cat}$ For simplicity, all cellular cations and anions were taken as univalent. Since cellular sodium and chloride concentrations are known to be approximately 30 meq/liter (52), the univalent assumption requires $C^{(2)}_{cat}$ and $C^{(2)}_{an}$ to be about 70 meq/liter. Since the model requires that one of these two quantities be specified precisely, $C^{(2)}_{cat}$

was chosen to be exactly 70 meq/liter. The presence of osmotically active polyvalent ions within the cell would alter the values of $C_{cat}^{(2)}$ and $C_{an}^{(2)}$ but would not greatly affect the basic predictions of the model. These assumptions differ from the assumption about C_c used in the continuous model. In the compartment model flows and forces across the luminal cell membrane were explicitly considered whereas in the continuous model luminal membrane volume flow was not calculated. Therefore, cell osmolarity is a dependent variable in the compartment model.

$\pi^{(5)}$ The in vivo capillary colloid osmotic pressure for the *Necturus* was found to be 9.29 cm H_2O in control and 3.48 cm H_2O during saline diuresis (21).

$p^{(5)}$ The hydrostatic pressure in the *Necturus* peritubular capillaries was found to be 2.23 cm H_2O in control and 3.37 cm H_2O during saline diuresis (21).

$\Psi^{(2)}$ The cell potential difference for the *Necturus* proximal tubule was taken as -70 mV which is an average of data from Giebisch (19) and Boulpaep.[6]

$\Psi^{(3)}$ Although there may be a drop in electrical potential along the cellular interspace, no methods are currently available for measuring this. Hence, the problem was simplified by assuming $\Psi^{(3)} = \Psi^{(4)}$.

$\Psi^{(4)}$ It was assumed that $\Psi^{(4)} = \Psi^{(5)} = 0$.

$\Delta\Psi^{\alpha}$ The transepithelial potential difference ($\Delta\Psi^{\alpha}$) was obtained from measurements in our laboratory of -15.4 mV under control conditions and -9.75 mV during volume expansion for the in vivo *Necturus* proximal tubule (7).

$\Delta\Psi^{\beta}$ Since $\Psi^{(3)} = \Psi^{(4)} = \Psi^{(5)} = 0$, $\Delta\Psi^{(\beta)} = \Psi^{(2)} - \Psi^{(3)} = \Psi^{(2)} = -70$ mV.

$\Delta\Psi^{\gamma}$ $\Delta\Psi^{\gamma} = \Psi^{(1)} - \Psi^{(2)} = \Delta\Psi^{\alpha} - \Delta\Psi^{\beta}$.

D See above.

r_{Cl} The ratio of cell Cl to luminal Cl was varied between 0.1 and 0.3. This ratio only affected the values of ${}_{act}J_{Cl}^{\gamma}$ and ω_{Cl}^{β}. The standard value of r_{Cl} was chosen as 0.3. An $r_{Cl} = 0.3$ corresponds to a cellular chloride concentration of 30 meq/liter.

r_t For a single salt, the ratio of ionic permeabilities is equivalent to the ratio of the ionic transference numbers. The ratio of Cl to Na transference numbers for the *Necturus* tight junction was measured in our laboratory as 1.6.[7]

$|\Delta x|$ See above.

RT See above.

F The Faraday; 96,500 C/mol from (42).

QUANTITIES VARIED OVER A RANGE OF EXPERIMENTALLY OBSERVED VALUES

$L_p{}^{\alpha}$ See above.

$L_p{}^{\beta}$ See above.

A^{β} The surface area of both lateral cell membranes bordering the interspace is $A^{\beta} = 2 \cdot L \cdot l$. For the standard interspace length of 25 μm, $A^{\beta} = 2 \times 25 \times 10^{-4}$ cm $\times$ 800 cm/cm^2 epithelium = 4 cm^2/cm^2 epithelium. For L = 40 and 60 μm, $A^{\beta} = 6.4$ and 9.6 cm^2/cm^2 epithelium, respectively.

$\sigma_{Na}^{\delta} = \sigma_{Cl}^{\delta}$ Although experiments by Welling and Grantham (44) suggest that

[6] Boulpaep, E. L. Electrophysiology of the proximal tubule of *Necturus* kidney. II. The luminal cell membrane and the paracellular pathway. Manuscript submitted for publication.

[7] Boulpaep, E. L. Electrophysiology of the proximal tubule of *Necturus* kidney. I. The peritubular cell membrane. Manuscript submitted for publication.

the basement membrane offers little resistance to small solutes, the reflection coefficient for Na and Cl may not be exactly zero. Hence, $\sigma^{\delta}_{Na} = \sigma^{\delta}_{Cl}$ was varied from 0 to 0.2 with zero taken as the standard value.

r_c See above.

r_π A range of values was investigated for $r_\pi = \pi^{(4)}/\pi^{(5)}$. For mammals the colloid osmotic pressure in the peritubular space, $\pi^{(4)}$, has been estimated to be in the range of 30–80 % of the plasma colloid osmotic pressure, $\pi^{(5)}$, (40, 11). In the standard *Necturus* (peritubular protein = 2.6 g/100 ml [21]) this corresponds to $\pi^{(4)}$ being between 26 and 77 % of $\pi^{(5)}$. The assumption is made that the ratio, $r_\pi = \pi^{(4)}/\pi^{(5)}$ is nearly constant during volume expansion so that r_π ranges between 0.26 and 0.77 for both control and volume expansion (see Table XI). Evidence for this invariance of r_π during saline diuresis comes from a comparison of colloid osmotic pressures during hydropenia and volume expansion in the dog (31).

APPENDIX E

Equations for the Compartment Model

General Equations

The basic mass balance equations for the compartment model are given in Table III. Each flux $\Phi_j{}^k$ is computed as the product of the flow per unit area, $J_j{}^k$, and the effective area of the barrier, A^k. The volume flows across each barrier are written according to Eq. 8 of the text.

$$J_v{}^{\alpha} = L_p{}^{\alpha}\cdot[p^{(1)} - p^{(3)} - \sigma^{\alpha}_{Na}\cdot RT\cdot[C^{(1)}_{Na} - C^{(3)}_{Na}] - \sigma^{\alpha}_{Cl}\cdot RT\cdot[C^{(1)}_{Cl} - C^{(3)}_{Cl}]]. \quad (1\,e)$$

$$J_v{}^{\beta} = L_p{}^{\beta}\cdot[p^{(2)} - p^{(3)} - \sigma^{\beta}_{Na}\cdot RT\cdot[C^{(2)}_{Na} - C^{(3)}_{Na}] - \sigma^{\beta}_{Cl}\cdot RT\cdot[C^{(2)}_{Cl} - C^{(3)}_{Cl}] - \sigma^{\beta}_{cat}\cdot RT\cdot C^{(2)}_{cat} - \sigma^{\beta}_{an}\cdot RT\cdot C^{(2)}_{an}]. \quad (2\,e)$$

$$J_v{}^{\gamma} = L_p{}^{\gamma}\cdot[p^{(1)} - p^{(2)} - \sigma^{\gamma}_{Na}\cdot RT\cdot[C^{(1)}_{Na} - C^{(2)}_{Na}] - \sigma^{\gamma}_{Cl}\cdot RT\cdot[C^{(1)}_{Cl} - C^{(2)}_{Cl}] + \sigma^{\gamma}_{cat}\cdot RT\cdot C^{(2)}_{cat} + \sigma^{\gamma}_{an}\cdot RT\cdot C^{(2)}_{an}]. \quad (3\,e)$$

$$J_v{}^{\delta} = L_p{}^{\delta}\cdot[p^{(3)} - p^{(4)} - \sigma^{\delta}_{Na}\cdot RT\cdot[C^{(3)}_{Na} - C^{(4)}_{Na}] - \sigma^{\delta}_{Cl}\cdot RT\cdot[C^{(3)}_{Cl} - C^{(4)}_{Cl}] + \pi^{(4)}]. \quad (4\,e)$$

$$J_v{}^{\epsilon} = L_p{}^{\epsilon}\cdot[p^{(4)} - p^{(5)} - \sigma^{\epsilon}_{Na}\cdot RT\cdot[C^{(4)}_{Na} - C^{(5)}_{Na}] - \sigma^{\epsilon}_{Cl}\cdot RT\cdot[C^{(4)}_{Cl} - C^{(5)}_{Cl}] + \pi^{(5)} - \pi^{(4)}]. \quad (5\,e)$$

Assuming no coupling between ions, Eq. 9 of the text expresses the flux of the jth ion across the kth barrier. For the range of concentrations considered, $\bar{C}_j{}^k$ can be approximated as the arithmetic mean of the concentrations in the two compartments on either side of barrier k. Active sodium transport is assumed to occur from cell to interspace across the lateral membrane. In order to satisfy mass balance a small active chloride flux was postulated across the luminal cell membrane.

In addition, the interspace peritubular space and capillary were assumed to be at the same electrical potential, i.e. $\Psi^{(3)} = \Psi^{(4)} = \Psi^{(5)}$. Under these assumptions there

are 10 equations describing the flux of Na^+ and Cl^- in the compartment model of Fig. 10.

$$J^{\alpha}_{Na} = (1/2)[C^{(1)}_{Na} + C^{(3)}_{Na}](1 - \sigma^{\alpha}_{Na})J_v{}^{\alpha} + RT\cdot\omega^{\alpha}_{Na}\cdot[C^{(1)}_{Na} - C^{(3)}_{Na}] + (1/2)[C^{(1)}_{Na} + C^{(3)}_{Na}]\cdot\omega^{\alpha}_{Na}\cdot F\cdot\Delta\Psi^{\alpha}. \quad (6\,e)$$

$$J^{\alpha}_{Cl} = (1/2)[C^{(1)}_{Cl} + C^{(3)}_{Cl}](1 - \sigma^{\alpha}_{Cl})J_v{}^{\alpha} + RT\cdot\omega^{\alpha}_{Cl}\cdot[C^{(1)}_{Cl} - C^{(3)}_{Cl}] - (1/2)[C^{(1)}_{Cl} + C^{(3)}_{Cl}]\cdot\omega^{\alpha}_{Cl}\cdot F\cdot\Delta\Psi^{\alpha}. \quad (7\,e)$$

$$J^{\beta}_{Na} = (1/2)[C^{(2)}_{Na} + C^{(3)}_{Na}](1 - \sigma^{\beta}_{Na})J_v{}^{\beta} + RT\cdot\omega^{\beta}_{Na}\cdot[C^{(2)}_{Na} - C^{(3)}_{Na}] + (1/2)[C^{(2)}_{Na} + C^{(3)}_{Na}]\cdot\omega^{\beta}_{Na}\cdot F\cdot\Delta\Psi^{\beta} + {}_{act}J^{\beta}_{Na}. \quad (8\,e)$$

$$J^{\beta}_{Cl} = (1/2)[C^{(2)}_{Cl} + C^{(3)}_{Cl}](1 - \sigma^{\beta}_{Cl})J_v{}^{\beta} + RT\cdot\omega^{\beta}_{Cl}\cdot[C^{(2)}_{Cl} - C^{(3)}_{Cl}] - (1/2)[C^{(2)}_{Cl} + C^{(3)}_{Cl}]\cdot\omega^{\beta}_{Cl}\cdot F\cdot\Delta\Psi^{\beta}. \quad (9\,e)$$

$$J^{\gamma}_{Na} = (1/2)[C^{(1)}_{Na} + C^{(2)}_{Na}](1 - \sigma^{\gamma}_{Na})J_v{}^{\gamma} + RT\cdot\omega^{\gamma}_{Na}\cdot[C^{(1)}_{Na} - C^{(2)}_{Na}] + (1/2)[C^{(1)}_{Na} + C^{(2)}_{Na}]\cdot\omega^{\gamma}_{Na}\cdot F\cdot\Delta\Psi^{\gamma}. \quad (10\,e)$$

$$J^{\gamma}_{Cl} = (1/2)[C^{(1)}_{Cl} + C^{(2)}_{Cl}](1 - \sigma^{\gamma}_{Cl})J_v{}^{\gamma} + RT\cdot\omega^{\gamma}_{Cl}\cdot[C^{(1)}_{Cl} - C^{(2)}_{Cl}] - (1/2)[C^{(1)}_{Cl} + C^{(2)}_{Cl}]\cdot\omega^{\gamma}_{Cl}\cdot F\cdot\Delta\Psi^{\gamma} + {}_{act}J^{\gamma}_{Cl}. \quad (11\,e)$$

$$J^{\delta}_{Na} = (1/2)[C^{(3)}_{Na} + C^{(4)}_{Na}](1 - \sigma^{\delta}_{Na})J_v{}^{\delta} + RT\cdot\omega^{\delta}_{Na}\cdot[C^{(3)}_{Na} - C^{(4)}_{Na}]. \quad (12\,e)$$

$$J^{\delta}_{Cl} = (1/2)[C^{(3)}_{Cl} + C^{(4)}_{Cl}](1 - \sigma^{\delta}_{Cl})J_v{}^{\delta} + RT\cdot\omega^{\delta}_{Cl}\cdot[C^{(3)}_{Cl} - C^{(4)}_{Cl}]. \quad (13\,e)$$

$$J^{\epsilon}_{Na} = (1/2)[C^{(4)}_{Na} + C^{(5)}_{Na}](1 - \sigma^{\epsilon}_{Na})J_v{}^{\epsilon} + RT\cdot\omega^{\epsilon}_{Na}\cdot[C^{(4)}_{Na} - C^{(5)}_{Na}]. \quad (14\,e)$$

$$J^{\epsilon}_{Cl} = (1/2)[C^{(4)}_{Cl} + C^{(5)}_{Cl}](1 - \sigma^{\epsilon}_{Cl})J_v{}^{\epsilon} + RT\cdot\omega^{\epsilon}_{Cl}\cdot[C^{(4)}_{Cl} - C^{(5)}_{Cl}]. \quad (15\,e)$$

The following relations follow from the electroneutrality of solutions: $C^{(1)}_{Na} = C^{(1)}_{Cl}$; $C^{(2)}_{Na} + C^{(2)}_{cat} = C^{(2)}_{Cl} + C^{(2)}_{an}$; $C^{(3)}_{Na} = C^{(3)}_{Cl}$; $C^{(4)}_{Na} = C^{(4)}_{Cl}$; $C^{(5)}_{Na} = C^{(5)}_{Cl}$.

List of Reductions

The following simplifying assumptions or reductions were used to evaluate the general equations of the compartment model: (*a*) In order to obtain a closed form solution to the equations, it was assumed that the three pressure gradients: $p^{(1)} - p^{(2)}$, $p^{(1)} - p^{(3)}$, and $p^{(2)} - p^{(3)}$ were all $\ll$ than the osmotic driving forces (see Appendix A). (*b*) As discussed in Appendix D, $\sigma^{\alpha}_{Na} = \sigma^{\alpha}_{Cl} = \sigma_s{}^{\alpha} = 0.7$; $\sigma^{\beta}_{Na} = \sigma^{\beta}_{Cl} = \sigma^{\beta}_{cat} = \sigma^{\beta}_{an} = \sigma_s{}^{\beta} = 1.0$; $\sigma^{\gamma}_{Na} = \sigma^{\gamma}_{Cl} = \sigma^{\gamma}_{cat} = \sigma^{\gamma}_{an} = \sigma_s{}^{\gamma} = 1.0$; $\sigma^{\delta}_{Na} = \sigma^{\delta}_{Cl} = \sigma_s{}^{\delta} = 0$ (except for Table IX); $\sigma^{\epsilon}_{Na} = \sigma^{\epsilon}_{Cl} = \sigma_s{}^{\epsilon} = 0$; $C^{(1)}_{Na} = C^{(5)}_{Na} = C_o$; $L_p{}^{\beta} = L_p{}^{\gamma}$.

Detailed Solution of the Equations

The preceding simplifying assumptions lead to the following set of reduced equations: Eq. 1 *e* implies,

$$J_v{}^{\alpha} = 2L_p{}^{\alpha}\cdot\sigma_s{}^{\alpha}\cdot RT\cdot[C^{(3)}_{Na} - C_o]. \quad (16\,e)$$

Eq. 2 *e* implies,

$$J_v^{\beta} = 2L_p^{\beta} \cdot RT \cdot [C_{Na}^{(3)} - (C_{Na}^{(2)} + C_{cat}^{(2)})]. \tag{17 e}$$

Eq. 3 *e* implies,

$$J_v^{\gamma} = 2L_p^{\gamma} \cdot RT \cdot [C_{Na}^{(2)} + C_{cat}^{(2)} - C_o]. \tag{18 e}$$

Eq. 4 *e* implies,

$$J_v^{\delta} = L_p^{\delta} \cdot [p^{(3)} - p^{(4)} + \pi^{(4)}]. \tag{19 e}$$

Eq. 5 *e* implies,

$$J_v^{\epsilon} = L_p^{\epsilon} \cdot [p^{(4)} - p^{(5)} + \pi^{(5)} - \pi^{(4)}]. \tag{20 e}$$

The cell sodium concentration, $C_{Na}^{(2)}$, is evaluated according to Eq. 1, Table III by equating Φ_v^{γ} and Φ_v^{β}, using Eqs. 17 *e* and 18 *e*.

$$C_{Na}^{(2)} = \frac{A^{\beta}}{A^{\beta} + A^{\gamma}} \cdot C_{Na}^{(3)} + \frac{A^{\gamma}}{A^{\beta} + A^{\gamma}} \cdot C_o - C_{cat}^{(2)}. \tag{21 e}$$

Substituting Eq. 1, Table III into Eq. 2, Table III and noting that $\Phi_v^{\delta} = \Phi_v^{te}$,

$$\Phi_v^{\alpha} + \Phi_v^{\gamma} = \Phi_v^{te}. \tag{22 e}$$

Using Eq. 16 *e* and 18 *e*,

$$2L_p^{\alpha} \cdot A^{\alpha} \cdot \sigma_s^{\alpha} \cdot RT \cdot [C_{Na}^{(3)} - C_o] + 2L_p^{\gamma} \cdot A^{\gamma} \cdot RT \cdot [C_{Na}^{(2)} + C_{cat}^{(2)} - C_o] = \Phi_v^{te}. \tag{23 e}$$

Substituting Eqs. 21 *e* into 23 *e* and solving for $C_{Na}^{(3)}$,

$$C_{Na}^{(3)} = \frac{\dfrac{\Phi_v^{te}}{2RT \cdot L_p^{\gamma} \cdot A^{\gamma}} + C_o \left[1 - \dfrac{A^{\gamma}}{A^{\beta} + A^{\gamma}} + \sigma_s^{\alpha} \cdot \dfrac{L_p^{\alpha} \cdot A^{\alpha}}{L_p^{\gamma} \cdot A^{\gamma}}\right]}{\sigma_s^{\alpha} \cdot \dfrac{L_p^{\alpha} \cdot A^{\alpha}}{L_p^{\gamma} \cdot A^{\gamma}} + \dfrac{A^{\beta}}{A^{\beta} + A^{\gamma}}}. \tag{24 e}$$

From the definition of r_{Cl},

$$C_{Cl}^{(2)} = r_{Cl} \cdot C_{Cl}^{(1)} = r_{Cl} \cdot C_o. \tag{25 e}$$

From electroneutrality,

$$C_{Cl}^{(3)} = C_{Na}^{(3)}. \tag{26 e}$$

Using the electroneutrality conditions and the list of reductions given previously, the remaining dependent parameters were evaluated as follows:
From Eq. 12 Table III and Eqs. 12 *e*, 13 *e*,

$$\omega_{Cl}^{\delta} = \omega_{Na}^{\delta}. \tag{27 e}$$

From Eqs. 8, 9, 12 Table III and Eqs. 14 *e*, 15 *e*,

$$\omega^{\epsilon}_{Cl} = \omega^{\epsilon}_{Na}. \tag{28 e}$$

For r_c different from 1×10^{-3}

$$\omega^{\epsilon}_{Cl} = \omega^{\epsilon}_{Na} = (D \cdot r_c)/(|\Delta x| \cdot RT),$$

(see Appendix D).

The peritubular space concentration $C^{(4)}_{Na}$ was evaluated according to Eq. 8 Table III by equating the ion fluxes Φ^{δ}_{Na} and Φ^{ϵ}_{Na}, using Eq. 12 *e* and 14 *e*.

$$C^{(4)}_{Na} = \frac{RT \cdot [\omega^{\epsilon}_{Na} \cdot A^{\epsilon} \cdot C_o + \omega^{\delta}_{Na} \cdot A^{\delta} \cdot C^{(3)}_{Na}] + (1/2) \cdot \Phi^{te}_{v} \cdot [C^{(3)}_{Na} - C_o]}{RT \cdot [\omega^{\epsilon}_{Na} \cdot A^{\epsilon} + \omega^{\delta}_{Na} \cdot A^{\delta}]}. \tag{29 e}$$

From electroneutrality:

$$C^{(4)}_{Cl} = C^{(4)}_{Na}. \tag{30 e}$$

From the definition of emergent concentration and Eqs. 3, 12 Table III, together with 12 *e*,

$$C_{emerg} = \frac{\Phi^{\epsilon}_{s}}{\Phi^{\epsilon}_{v}} = \frac{\Phi^{\delta}_{s}}{\Phi^{\delta}_{v}} = \frac{\Phi^{\delta}_{Na}}{\Phi^{\delta}_{v}} = (1/2)[C^{(3)}_{Na} + C^{(4)}_{Na}] + \frac{RT \cdot \omega^{\delta}_{Na} \cdot A^{\delta} \cdot [C^{(3)}_{Na} - C^{(4)}_{Na}]}{\Phi^{te}_{v}}. \tag{31 e}$$

The flux Φ^{β}_{Na} is evaluated from 8 *e*,

$$\Phi^{\beta}_{Na} = RT \cdot \omega^{\beta}_{Na} \cdot A^{\beta} \cdot [C^{(2)}_{Na} - C^{(3)}_{Na}] + (1/2)[C^{(2)}_{Na} + C^{(3)}_{Na}]\omega^{\beta}_{Na} \cdot A^{\beta} \cdot F \cdot \Delta\Psi^{\beta} + {}_{act}J^{\beta}_{Na} \cdot A^{\beta}. \tag{32 e}$$

Although ${}_{act}J^{\beta}_{Na}$ is listed as a dependent parameter in Table V, it is actually used as an input parameter in the system of equations for the compartment model. However, ${}_{act}J^{\beta}_{Na}$ is limited to a small range of ±5% around the value quoted in Table V. Values of ${}_{act}J^{\beta}_{Na}$ beyond this range cause at least one of the membrane coefficients to be negative which indicates violation of mass balance. In addition, the choice of ${}_{act}J^{\beta}_{Na}$ was found to be further restricted by the requirement that, $\omega_s{}^{\alpha}$ (volume expansion)/$\omega_s{}^{\alpha}$ (control) $\simeq$ 3.0 as measured in our laboratory (7). The result of these restrictions was that only a small range of values for ${}_{act}J^{\beta}_{Na}$ produced physiologically meaningful results. The flux Φ^{δ}_{Na} is evaluated from Eq. 12 *e*,

$$\Phi^{\alpha}_{Na} = (1/2)[C^{(3)}_{Na} + C^{(4)}_{Na}]\Phi^{te}_{v} + RT \cdot \omega^{\delta}_{Na} \cdot A^{\delta} \cdot [C^{(3)}_{Na} - C^{(4)}_{Na}]. \tag{33 e}$$

The flux Φ^{δ}_{Na} is evaluated from Eq. 6 Table III,

$$\Phi^{\alpha}_{Na} = \Phi^{\delta}_{Na} - \Phi^{\beta}_{Na}. \tag{34 e}$$

The coefficient ω^{γ}_{Na} is evaluated according to Eq. 4 Table III by equating the ion

fluxes Φ^{β}_{Na} and Φ^{γ}_{Na}, using Eqs. 8 *e* and 10 *e*:

$$\omega^{\gamma}_{Na} = \frac{\Phi^{\beta}_{Na}}{A^{\gamma}\cdot[RT\cdot(C_o - C^{(2)}_{Na}) + (1/2)(C_o + C^{(2)}_{Na})F\cdot\Delta\Psi^{\gamma}]}. \tag{35 e}$$

ω^{α}_{Na} is determined from Eq. 6 *e*,

$$\omega^{\alpha}_{Na} = \frac{\Phi^{\alpha}_{Na} - (1/2)[C_o + C^{(3)}_{Na}](1 - \sigma^{\alpha}_{Na})\Phi_v{}^{\alpha}}{A^{\alpha}\cdot[RT\cdot(C_o - C^{(3)}_{Na}) + (1/2)(C_o + C^{(3)}_{Na})F\cdot\Delta\Psi^{\alpha}]}, \tag{36 e}$$

where $\Phi_v{}^{\alpha}$ is obtained from Eq. 16 *e*, and Φ^{α}_{Na} from Eq. 34 *e*. From the definition of r_t, it follows that:

$$\omega^{\alpha}_{Cl} = r_t\cdot\omega^{\alpha}_{Na}. \tag{37 e}$$

The flux Φ^{α}_{Cl} is evaluated from Eq. 7 *e*,

$$\Phi^{\alpha}_{Cl} = (1/2)[C_o + C^{(3)}_{Cl}](1 - \sigma^{\alpha}_{Cl})\Phi_v{}^{\alpha} + \omega^{\alpha}_{Cl}\cdot A^{\alpha}\cdot[RT\cdot(C_o - C^{(3)}_{Cl}) - (1/2)(C_o + C^{(3)}_{Cl})F\cdot\Delta\Psi^{\alpha}]. \tag{38 e}$$

The flux Φ^{δ}_{Cl} is evaluated from Eq. 13 *e*,

$$\Phi^{\delta}_{Cl} = (1/2)[C^{(3)}_{Cl} + C^{(4)}_{Cl}]\Phi_v{}^{te} + RT\cdot\omega^{\delta}_{Cl}\cdot A^{\delta}\cdot[C^{(3)}_{Cl} - C^{(4)}_{Cl}]. \tag{39 e}$$

The flux Φ^{β}_{Cl} is evaluated from Eq. 7 Table III and Eqs. 38 *e*, 39 *e*:

$$\Phi^{\beta}_{Cl} = \Phi^{\delta}_{Cl} - \Phi^{\alpha}_{Cl}. \tag{40 e}$$

The coefficient ω^{β}_{Cl} is determined from Eq. 9 *e*,

$$\omega^{\beta}_{Cl} = \frac{\Phi^{\beta}_{Cl}}{RT\cdot A^{\beta}\cdot[C^{(2)}_{Cl} - C^{(3)}_{Cl}] - (1/2)[C^{(2)}_{Cl} + C^{(3)}_{Cl}]\cdot A^{\beta}\cdot F\cdot\Delta\Psi^{\beta}}. \tag{41 e}$$

The active chloride transport, ${}_{act}J^{\gamma}_{Cl}$ is evaluated according to Eq. 5 Table III by equating the ion fluxes Φ^{γ}_{Cl} and Φ^{β}_{Cl}, using Eq. 11 *e*:

$${}_{act}J^{\gamma}_{Cl} = \frac{\Phi^{\beta}_{Cl}}{A^{\gamma}} - RT\cdot\omega^{\gamma}_{Cl}\cdot[C_o - C^{(2)}_{Cl}] + (1/2)[C_o + C^{(2)}_{Cl}]\cdot\omega^{\gamma}_{Cl}\cdot F\cdot\Delta\Psi^{\gamma}. \tag{42 e}$$

From Kedem and Leaf (25) the salt (NaCl) permeability coefficient can be expressed in terms of the ionic permeability coefficients:

$$\omega^{\alpha}_{s} = \frac{\omega^{\alpha}_{Na}\cdot\omega^{\alpha}_{Cl}}{\omega^{\alpha}_{Na} + \omega^{\alpha}_{Cl}}. \tag{43 e}$$

The basic assumptions and equations of the compartment model do not provide enough information to evaluate the five remaining dependent parameters; $L_p{}^{\delta}$, $L_p{}^{\epsilon}$,

$\pi^{(4)}$, $p^{(3)}$, and $p^{(4)}$. Estimates for these quantities were obtained from two additional assumptions: (*a*) Under control conditions: $p^{(3)} \simeq p^{(4)} \simeq p^{(5)}$, (*b*) $r_\pi = [\pi^{(4)}/\pi^{(5)}]_{\text{control}} = [\pi^{(4)}/\pi^{(5)}]_{\text{VE}}$ where (VE) denotes volume expansion. From the above assumptions and Eq. 3 Table III with Eq. 19 *e*,

$$L_p^{\delta}\big|_{\text{control}} = \left[\frac{\Phi_v^{te}}{A^{\delta}\cdot\pi^{(4)}}\right]_{\text{control}}. \tag{44 e}$$

From Eq. 3 Table III with Eq. 20 *e*,

$$L_p^{\epsilon}\big|_{\text{control}} = \left[\frac{\Phi_v^{te}}{A^{\epsilon}\cdot\pi^{(5)}\cdot(1-r_\pi)}\right]_{\text{control}}. \tag{45 e}$$

For the parameter values in Table V, $A^{\epsilon} = A^{\delta}$; for those in Table VI, $A^{\epsilon} = 1$ cm^2/cm^2 epithelium. It was also assumed that $L_p{}^{\delta}$ and $L_p{}^{\epsilon}$ were invariant during volume expansion.

From the second additional assumption, the capillary osmotic pressure during volume expansion is given by,

$$\pi^{(4)}(\text{VE}) = r_\pi\cdot\pi^{(5)}(\text{VE}). \tag{46 e}$$

From Eq. 20 *e* during control and volume expansion, noting that $\Phi_v{}^{\epsilon} = \Phi_v^{te}$

$$\left[\frac{\Phi_v^{te}}{(1-r_\pi)\cdot\pi^{(5)}}\right]_{\text{control}} = \left[\frac{\Phi_v^{te}}{p^{(4)} - p^{(5)} + (1-r_\pi)\cdot\pi^{(5)}}\right]_{\text{VE}},$$

or

$$p^{(4)}(\text{VE}) = p^{(5)}(\text{VE}) + [1-r_\pi]\left[\frac{\Phi_v^{te}(\text{VE})}{\Phi_v^{te}(\text{control})}\cdot\pi^{(5)}(\text{control}) - \pi^{(5)}(\text{VE})\right] \tag{47 e}$$

From Eq. 3 Table III and Eq. 19 *e* during control and volume expansion, noting that $\Phi_v{}^{\delta} = \Phi_v^{te}$,

$$\left[\frac{\Phi_v^{te}}{\pi^{(4)}}\right]_{\text{control}} = \left[\frac{\Phi_v^{te}}{p^{(3)} - p^{(4)} + \pi^{(4)}}\right]_{\text{VE}},$$

or

$$p^{(3)}(\text{VE}) = p^{(5)}(\text{VE}) + \left[\frac{\Phi_v^{te}(\text{VE})}{\Phi_v^{te}(\text{control})}\cdot\pi^{(5)}(\text{control}) - \pi^{(5)}(\text{VE})\right]. \tag{48 e}$$

The flux ratios were obtained from the flux expressions and the definition:

$$R_j{}^k = \Phi_j{}^k/\Phi_j^{te}, \tag{49 e}$$

where $\Phi_{\text{Na}}^{te} = \Phi_{\text{Cl}}^{te} = \Phi_s^{te}$.

The dependent parameters of the compartment model were evaluated from Eqs. 21 *e* through 49 *e* together with the independent parameters in Table IV. The

equations were solved first for the case of noninteracting regions of peritubular fluid (see Fig. 3 B). This represents a first approximation since mixing between the two regions produces peritubular space profiles similar to those shown in Fig. 4 which are inhomogeneous in both x and y directions.

To estimate the degree of inhomogeneity in the x direction, the compartment model was used to evaluate $C_{Na}^{(4\delta)}$ and $C_{Na}^{(4\epsilon)}$ for the equivalent interacting case. (The notation: (4δ), (4ϵ) is defined in the glossary and illustrated in Fig. 10 B.) The following calculations are based on ratios of net salt to water flux determined from the noninteracting case, i.e., Eq. 31 *e*.

The net Na flux leaving the mouth of the interspace and crossing the tubular basement membrane is given by Eq. 12 *e* where $C_{Na}^{(4)}$ is replaced by $C_{Na}^{(4\delta)}$:

$$\Phi_{Na}^{\delta} = (1/2)[C_{Na}^{(3)} + C_{Na}^{(4\delta)}]\Phi_v^{te} + RT \cdot \omega_{Na}^{\delta} \cdot A^{\delta} \cdot [C_{Na}^{(3)} - C_{Na}^{(4\delta)}], \tag{50 e}$$

so that,

$$C_{Na}^{(4\delta)} = C_{Na}^{(3)} - \frac{\Phi_v^{te} \cdot C_{Na}^{(3)} - \Phi_{Na}^{\delta}}{(1/2)\Phi_v^{te} - RT \cdot \omega_{Na}^{\delta} \cdot A^{\delta}}, \tag{51 e}$$

where Φ_{Na}^{δ} is the salt flux calculated for the noninteracting condition.

Similarly, the Na flux across the capillary endothelium is given by Eq. 14 *e* where $C_{Na}^{(4)}$ is replaced by $C_{Na}^{(4\epsilon)}$ and $A^{\epsilon} = 1\ cm^2/cm^2$ epithelium.

$$\Phi_{Na}^{\epsilon} = (1/2)[C_{Na}^{(4\epsilon)} + C_o]\Phi_v^{te} + RT \cdot \omega_{Na}^{\epsilon} \cdot A^{\epsilon} \cdot [C_{Na}^{(4\epsilon)} - C_o], \tag{52 e}$$

so that,

$$C_{Na}^{(4\epsilon)} = C_o + \frac{\Phi_{Na}^{\epsilon} - \Phi_v^{te} \cdot C_o}{(1/2)\Phi_v^{te} + RT \cdot \omega_{Na}^{\epsilon} \cdot A^{\epsilon}}, \tag{53 e}$$

where $\Phi_{Na}^{\epsilon} = \Phi_{Na}^{\delta}$, calculated from the noninteracting condition.

In addition, the predicted value of $L_p{}^{\epsilon}$ will differ for the interacting and noninteracting cases because of its dependence on A^{ϵ} (see Eq. 45 *e*). The values of $C_{Na}^{(4\delta)}$, $C_{Na}^{(4\epsilon)}$, and $L_p{}^{\epsilon}$ under conditions of solute dispersion are summarized in Table VI. The remaining parameters of the compartment model in Tables IV and V are unchanged with solute dispersion.

The authors thank Dr. D. Rosner for worthwhile discussions and Dr. K. Spring for critical reading of the manuscript.

This investigation was supported by Research Grant 5-R01-AM-13844 and Program Project AM-17433 from the National Institute of Arthritis, Metabolic, and Digestive Diseases.

Received for publication 25 April 1975.

REFERENCES

1. ANAGNOSTOPOULOS, T., and E. E. WINDHAGER. 1970. Microperfusion study of cortical peritubular capillaries in rat kidney. *Fed. Proc.* **29**:397.
2. BENTZEL, C. J. 1972. Proximal tubule structure-function relationships during volume expansion in *Necturus*. *Kidney Int.* **2**:324.

3. BENTZEL, C. J., M. DAVIES, W. N. SCOTT, M. ZATZMAN, and A. K. SOLOMON. 1968. Osmotic volume flow in the proximal tubule of *Necturus* kidney. *J. Gen. Physiol.* **51**:517.
4. BENTZEL, C. J., B. PARSA, and D. K. HARE. 1969. Osmotic flow across proximal tubule of *Necturus*, correlation of physiologic and anatomic studies. *Am. J. Physiol.* **217**:570.
5. BERRY, C. A., and E. L. BOULPAEP. 1975. Nonelectrolyte permeability of the paracellular pathway in *Necturus* proximal tubule. *Am. J. Physiol.* **228**:581.
6. BOULPAEP, E. L. 1970. Electrophysiological properties of the proximal tubule. Importance of cellular and intercellular transport pathways. *In* Symposia Medica Hoechst. Electrophysiology of Epithelial Cells. G. Giebisch, editor. F. K. Schattauer, Stuttgart. 91.
7. BOULPAEP, E. L. 1972. Permeability changes of the proximal tubule of *Necturus* during saline loading. *Am. J. Physiol.* **222**:517.
8. CLAUDE, P. 1968. An electron microscopic study of urinary tubules of *Necturus* maculosus. Ph.D. thesis. University of Pennsylvania.
9. CURRAN, P. F. 1960. Na, Cl and water transport by rat ileum in vitro. *J. Gen. Physiol.* **43**: 1137.
10. CURRAN, P. F., and J. R. MCINTOSH. 1962. A model system for biological water transport. *Nature (Lond.)*. **193**:347.
11. DEEN, W. M., C. R. ROBERTSON, and B. M. BRENNER. 1973. A model of peritubular capillary control of isotonic fluid reabsorption by the renal proximal tubule. *Biophys. J.* **13**:340.
12. DIAMOND, J. M. 1964. The mechanism of isotonic water transport. *J. Gen. Physiol.* **48**:15.
13. DIAMOND, J. M., and W. H. BOSSERT. 1967. Standing-gradient osmotic flow: A mechanism for coupling of water and solute transport in epithelia. *J. Gen. Physiol.* **50**:2061.
14. FALCHUK, K. H., and R. W. BERLINER. 1971. Hydrostatic pressures in peritubular capillaries and tubules in the rat kidney. *Am. J. Physiol.* **220**:1422.
15. FARQUHAR, M. G., and G. E. PALADE. 1964. Functional organization of amphibian skin. *Proc. Natl. Acad. Sci. U.S.A.* **51**:569.
16. FRIZZELL, R. A., and S. G. SCHULTZ. 1972. Ionic conductances of extracellular shunt pathway in rabbit ileum. *J. Gen. Physiol.* **59**:318.
17. FRÖMTER, E. 1972. The route of passive ion movement through the epithelium of *Necturus* gallbladder. *J. Membr. Biol.* **8**:259.
18. FRÖMTER, E., and J. DIAMOND. 1972. Route of passive ion permeation in epithelia. *Nat. New Biol.* **235**:9.
19. GIEBISCH, G. 1958. Electrical potential measurements on single nephrons of *Necturus*. *J. Cell. Comp. Physiol.* **51**:221.
20. GOLDGRABEN, J. R., and S. WEINBAUM. 1973. On the mixing of a low Reynolds number biological jet with a quiescent outer bathing solution. *J. Fluid Mech.* **59**:159.
21. GRANDCHAMP, A., and E. L. BOULPAEP. 1974. Pressure control of sodium reabsorption and intercellular backflux across proximal kidney tubule. *J. Clin. Invest.* **54**:69.
22. GRANTHAM, J. J. 1971. Mode of water transport in mammalian collecting tubules. *Fed. Proc.* **30**:14.
23. KEDEM, O., and A. KATCHALSKY. 1962. Permeability of composite membranes, Part 1.— Electric current, volume flow and flow of solute through membranes. *Trans. Farad. Soc.* **59**:1918.
24. KEDEM, O., and A. KATCHALSKY. 1962. Permeability of composite membranes, Part 2.— Parallel elements. *Trans. Farad. Soc.* **59**:1931.
25. KEDEM, O., and A. LEAF. 1966. The relation between salt and ionic transport coefficients. *J. Gen. Physiol.* **49**:655.
26. KING, L. V. 1914. On the convection of heat from small cylinders in a stream of fluid. *Philos. Trans. R. Soc. Lond. B Biol. Sci.* **A214**:373.
27. LANDIS, E. M., and J. R. PAPPENHEIMER. 1963. Exchange of substances through capillary walls. *In* Handbook of Physiology. Circulation. Williams and Wilkins, Baltimore, Md. **2**:1010.
28. MACHEN, T. E., D. ERLIJ, and F. B. P. WOODING. 1972. Permeable junctional complexes: The movement of Lanthanum across rabbit gallbladder and intestine. *J. Cell Biol.* **54**:302.
29. MAUNSBACH, A. 1973. Ultrastructure of proximal tubule. *In* Handbook of Physiology. Renal Physiology. Sec. 8, Ch. 2:31.

30. OGILVIE, J. T., J. R. MCINTOSH, and P. F. CURRAN. 1963. Volume flow in a series-membrane system. *Biochim. Biophys. Acta.* **66**:441.
31. OTT, C. E., J. A. HAAS, J. L. CUCHE, and F. G. KNOX. 1975. Effect of increased peritubule protein concentration on proximal tubule reabsorption in the presence and absence of extracellular volume expansion. *J. Clin. Invest.* **55**:612.
32. PAPPENHEIMER, J. R., E. M. RENKIN, and L. M. BORRERO. 1951. Filtration, diffusion and molecular sieving through peripheral capillary membranes. A contribution to the pore theory of capillary permeability. *Am. J. Physiol.* **167**:13.
33. PATLAK, C. S., D. A. GOLDSTEIN, and J. F. HOFFMAN. 1963. The flow of solute and solvent across a two-membrane system. *J. Theor. Biol.* **5**:426.
34. POWELL, D. W., and S. J. MALAWER. 1968. Relationship between water and solute transport from isosmotic solutions by rat intestine in vivo. *Am. J. Physiol.* **215**:49.
35. ROBINSON, R. A., and R. H. STOKES. 1959. Electrolyte Solutions. Butterworths, London.
36. SAUER, F. 1973. Appendix: Nonequilibrium thermodynamics of kidney tubule transport. *In* Handbook of Physiology. Renal Physiology. Sec. 8, Ch. 12:399.
37. SPRING, K. R. 1973. A parallel path model for *Necturus* proximal tubule. *J. Membr. Biol.* **13**:323.
38. STIRLING, E. S. 1972. Radioautographic localization of sodium pump sites in rabbit intestine. *J. Cell. Biol.* **53**:704.
39. TORMEY, J. M., and J. M. DIAMOND. 1967. The ultrastructural route of fluid transport in rabbit gall bladder. *J. Gen. Physiol.* **50**:2031.
40. VOGEL, C. 1969. "Über den Austausch des extravasalen Plasma-Albumins (^{131}J-Albumin) der Niere mit dem Blut und den Abfluss von Makromolekülen (Polyvinylpyrrolidon) mit der Nierenlymphe bei normaler und durch Furosemid gehemmter tubulärer Reabsorption. *Pfluegers Arch. Eur. J. Physiol.* **305**:47.
41. WALL, B. J., J. L. OSCHMANN, and B. SCHMIDT-NIELSEN 1970. Fluid transport: Concentration of the intercellular compartment. *Science* (*Wash. D.C.*). **167**:1497.
42. WEAST, R. C., editor. 1974. Handbook of chemistry and physics. Chemical Rubber Co., Cleveland, Ohio.
43. WEINBAUM, S., and J. R. GOLDGRABEN. 1972. On the movement of water and solute in extracellular channels with filtration, osmosis and active transport. *J. Fluid Mech.* **53**:481.
44. WELLING, L. W., and J. J. GRANTHAM. 1972. Physical properties of isolated perfused renal tubules and tubular basement membrane. *J. Clin. Invest.* **51**:1063.
45. WELLING, D. J., L. W. WELLING, and L. P. SULLIVAN. 1973. Possible influence of basement membrane on intercellular transport: An analytic formulation. *Fed. Proc.* **32**:624.
46. WHEELER, H. O. 1963. Transport of electrolytes and water across wall of rabbit gallbladder. *Am. J. Physiol.* **205**:427.
47. WHITLOCK, R. T., and H. O. WHEELER. 1964. Coupled transport of solute and water across rabbit gallbladder epithelium. *J. Clin. Invest.* **43**:2249.
48. WHITTEMBURY, G. 1967. Sobre los mecanismos de absorción en el tubo proximal del riñón. *Acta Cient. Venez.* 3 Suppl.:71.
49. WHITTEMBURY, G., D. E. OKEN, E. E. WINDHAGER, and A. K. SOLOMON. 1959. Single proximal tubules of *Necturus* kidney. IV. Dependence of H_2O movement on osmotic gradients. *Am. J. Physiol.* **197**:1121.
50. WHITTEMBURY, G., and F. A. RAWLINS. 1971. Evidence of a paracellular pathway for ion flow in the kidney proximal tubule: electronmicroscopic demonstration of lanthanum precipitate in the tight junction. *Pfluegers Arch. Eur. J. Physiol.* **330**:302.
51. WHITTEMBURY, G., N. SUGINO, and A. K. SOLOMON. 1960. Effects of antidiuretic hormone and calcium on the equivalent pore radius of slices from *Necturus*. *Nature* (*Lond.*). **187**:699.
52. WHITTEMBURY, G., N. SUGINO, and A. K. SOLOMON. 1961. Ionic permeability and electrical potential differences in *Necturus* kidney cells. *J. Gen. Physiol.* **44**:689.
53. WILSON, H. A. 1904. On the convection of heat. *Proc. Camb. Phil. Soc.* **12**:413.